JETP Letters, Vol. 78, No. 11, 2003, pp. 691–694. From Pis'ma v Zhurnal Éksperimental'noĭ i Teoreticheskoĭ Fiziki, Vol. 78, No. 11, 2003, pp. 1203–1206.
Original English Text Copyright © 2003 by Volovik.

Dark Matter from the SU(4) Model¶

G. E. Volovik
Low Temperature Laboratory, Helsinki University of Technology, FIN-02015 HUT, Finland
Landau Institute for Theoretical Physics, Russian Academy of Sciences, Moscow, 117334 Russia
e-mail: volovik@boojum.hut.fi

Received October 16, 2003; in final form, October 24, 2003

The left–right symmetric Pati–Salam model of the unification of quarks and leptons is based on the SU(4) and SU(2) × SU(2) symmetry groups. These groups are naturally extended to include the classification of families of quarks and leptons. We assume that the family group (the group which unites the families) is also the SU(4) group. The properties of the fourth generation of fermions are the same as those of the ordinary-matter fermions in the first three generations except for the family charge of the $SU(4)_F$ group: $F = (1/3, 1/3, 1/3, -1)$, where $F = 1/3$ for fermions of ordinary matter and $F = -1$ for the fourth-generation fermions. The difference in F does not allow mixing between ordinary and fourth-generation fermions. Because of the conservation of the F charge, the creation of baryons and leptons in the process of electroweak baryogenesis must be accompanied by the creation of fermions of the fourth generation. As a result, the excess n_B of baryons over antibaryons leads to the excess $n_{4\nu} = N - \bar{N}$ of neutrinos over antineutrinos in the fourth generation with $n_{4\nu} = n_B$. This massive neutrino may form nonbaryonic dark matter. In principle, the mass density of the fourth neutrino $n_{4\nu}m_N$ in the Universe can make the main contribution to dark matter, since the lower bound on the neutrino mass m_N from the data on decay of the Z bosons is $m_N > m_Z/2$. The straightforward prediction of this model leads to the amount of cold dark matter relative to baryons, which is an order of magnitude higher than allowed by observations. This inconsistency may be avoided by nonconservation of the F charge. *© 2003 MAIK "Nauka/Interperiodica".*

PACS numbers: 12.10.-g; 12.60.Rc; 95.35.+d

1. INTRODUCTION

The three-family structure of fermions is one of the most puzzling features of the Standard Model. The other puzzles come from the baryonic asymmetry of the Universe and from astrophysical observations of dark matter, whose particles are most likely beyond the Standard Model. Here, we make an attempt to connect these three phenomena in the framework of the SU(4) scheme with four families of fermions. We discuss why the classification scheme based on the SU(4) groups is preferable and how it leads to nonbaryonic dark matter in the Universe if the Universe is baryonic asymmetric.

Breaking of the SU(4) symmetry between four generations to its $SU(3) \times U(1)_F$ subgroup separates the fermions of the fourth generation from the fermions of the other three families. If the charge F, the generator of the $U(1)_F$ group, is conserved in the process of baryogenesis, as happens, for example, in electroweak baryogenesis, the formation of the baryon asymmetry automatically leads to formation of dark matter made of the massive fourth-generation neutrinos. In such a scenario, the mass density of the matter in the Universe substantially exceeds the mass density of baryonic matter.

2. PATI–SALAM MODEL

In the current Standard Model, three families (generations) of fermions have identical properties above the electroweak energy scale. Each family contains 16 Weyl fermions (eight left and eight right) which transform under the gauge group $G(213) = SU(2)_L \times U(1)_Y \times SU(3)_C$ of weak, hypercharge, and strong interactions, respectively. In addition, they are characterized by two global charges: baryonic number B and leptonic number L.

The Grand Unification Theories (GUT) unify weak, hypercharge, and strong interactions into one big symmetry group, such as $SO(10)$, with a single coupling constant. There is, however, another group, the minimal subgroup of $SO(10)$, which also elegantly unites 16 fermions in each generation, a type of Pati–Salam model [1–3] with the symmetry group $G(224) = SU(2)_L \times SU(2)_R \times SU(4)_C$. This left–right symmetric group preserves all the important properties of $SO(10)$, but it has advantages when compared to the $SO(10)$ group [4–6]. In particular, the electric charge is left–right symmetric:

$$Q = \frac{1}{2}(B-L) + T_{R3} + T_{L3}, \tag{1}$$

where $B - L = (1/3, 1/3, 1/3, -1)$ is the difference between baryon and lepton numbers (the generator of $SU(4)_C$ color group) and T_{R3} and T_{L3} are left and right

---

¶ This article was submitted by the author in English.

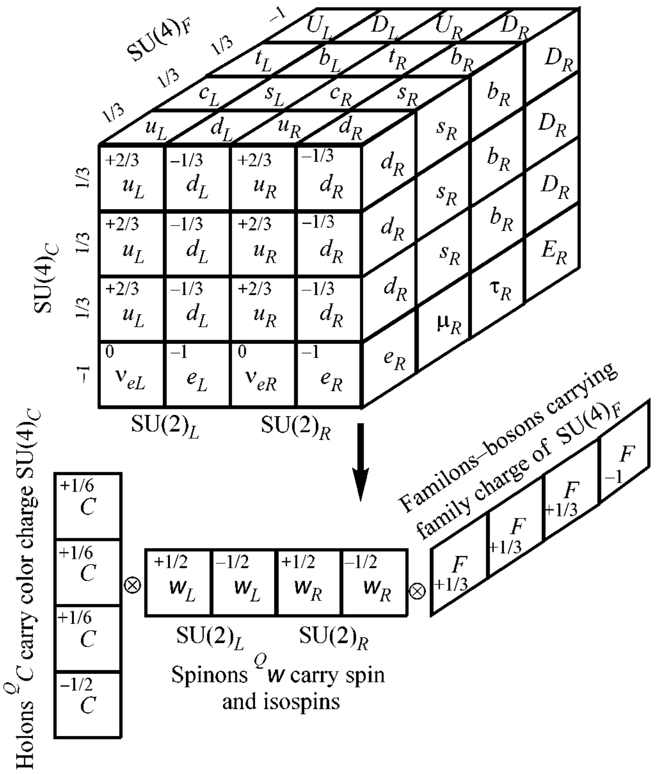

Fig. 1. Terazawa scheme of composite fermions *wC* as bound states of *w*-fermions and *C* bosons. Numbers show the electric charge.

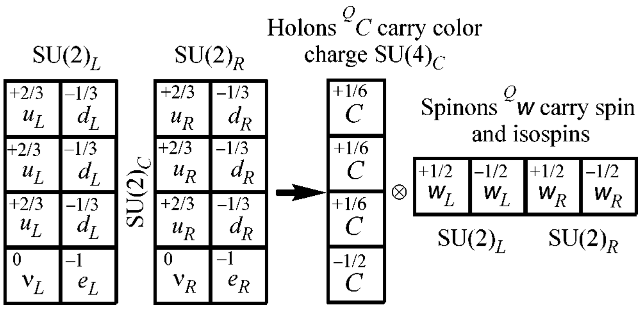

Fig. 2. Extended Terazawa scheme of composite fermions *wCF* as bound states of *w* fermions and *C* and *F* bosons.

isotopic spins (generators of the groups $SU(2)_R$ and $SU(2)_L$). Also, the G(224) group nicely fits the classification scheme of quantum vacua based on the momentum-space topology of fermionic propagators [7].

According to Terazawa [8], the 16 fermions of each generation can be represented as the product *Cw* of four bosons and four fermions in Fig. 1. The Terazawa scheme is similar to the slave-boson approach in condensed matter, where the spinons are fermions which carry spin and holons are bosons which carry electric charge [7]. Here, the "holons" *C* form the color $SU(4)_C$ quartet of spin-0 SU(2) singlet particles with $B - L$ charges of the $SU(4)_C$ group and electric charges $Q = (1/6, 1/6, 1/6, -1/2)$. The "spinons" are spin-1/2 particles *w*, which are color $SU(4)_C$ singlets and SU(2) isodoublets.

3. FAMILY CHARGE AND FOURTH GENERATION

What is missing in this scheme is fermionic families. The natural extension, which also uses the SU(4) symmetry, is to introduce the group $SU(4)_F$ in the family direction (Fig. 2). This requires the introduction of additional fourth generation of fermions. Then, the family charge *F* comes as one of the generators of $SU(4)_F$ in the same way as the $B - L$ charge comes as one of the generators of $SU(4)_C$ color group: $F = (1/3, 1/3, 1/3, -1)$. Here, $F = 1/3$ is assigned to ordinary matter in three generations, while $F = -1$ corresponds to the fourth generation.

The total number 64 of Weyl fermions, each being described by two complex or four real functions, satisfies the 2^n rule, which probably reflects the importance of the Clifford algebra in the underlying physics [9]. This is another advantage of classification based on SU(2) and SU(4) groups. This extension also fits the Terazawa scheme, which is modified by the addition of extra bosons. All 64 fermions are now represented as the product *FCw* in Fig. 2, where *F* is the quartet of bosons with *F* charges of the $SU(4)_F$.

Let us assume that the breaking of $SU(4)_F$ symmetry occurred in the same way as the breaking of the color group: $SU(4)_C \longrightarrow SU(3)_C \times U(1)_{B-L}$ and $SU(4)_F \longrightarrow SU(3)_F \times U(1)_F$, where $U(1)_F$ is the group generated by charge *F*. Then, all the charges of the fourth-generation fermions are the same as those of the ordinary-matter fermions in the first three generations except for the family charge *F*. This separates out the fourth generation in the same manner as leptons—the fourth color—are separated from quarks. The fourth-generation fermions cannot mix with ordinary fermions in the first three generations in the same manner as leptons cannot mix with quarks. This is the main difference from the democratic scheme of sequential generations, which assumes that all generations are equal. The important consequence of such a discrimination between the generations is that the excess of the baryonic charge in the Universe must be accompanied by the uncompensated neutrinos of the fourth generation.

4. DARK MATTER AND ELECTROWEAK BARYOGENESIS

Let us assume that the *F* charge is strictly conserved. This certainly occurs in the process of electroweak baryogenesis, in which the baryons and leptons are created due to the anomalous nonconservation of the baryonic and leptonic numbers, while the chiral anomaly conserves the charges F and $B-L$ (this does not depend on whether $\mathrm{SU}(4)_F$ is a local or global group). The conservation of these two charges gives

$$\begin{aligned} F &= \frac{1}{3}(n_q + n_l) - (n_{4q} + n_{4l}) = 0, \\ B - L &= \frac{1}{3}(n_q + n_{4q}) - (n_l + n_{4l}) = 0, \end{aligned} \tag{2}$$

where n_q and n_l are (algebraic) densities of quarks and leptons belonging to ordinary matter in three generations and n_{4q} and n_{4l} are that of the fourth generation. From Eqs. (2), one obtains the densities of the fourth-generation quarks and leptons in terms of ordinary matter (which mainly belongs to the first generation):

$$n_{4q} = n_l, \quad n_{4l} = \frac{1}{3}n_q - \frac{2}{3}n_l. \tag{3}$$

If in our Universe $n_l = 0$, i.e., the leptonic charge of electrons is compensated by that of antineutrinos, one obtains

$$n_{4q} = 0, \quad n_{4l} = \frac{1}{3}n_q = n_B, \tag{4}$$

where n_B is the algebraic number density of baryons in our Universe.

This means that any excess of the baryonic charge in the Universe is accompanied by the excess $n_{4\nu} = N - \bar{N} = n_B$ of the neutrinos over antineutrinos in the fourth generation (we assume that the mass of the fourth-generation neutrino is smaller than that of the fourth-generation electron, $m_N < m_E$). If this is correct, the fourth-generation neutrinos add to the mass of our Universe and may play the role of dark matter. The mass m_N of the fourth-generation (dark) neutrino can be expressed in terms of the mass of baryon (nucleon) m_B and the energies stored in baryonic matter (with fraction Ω_B of the total mass in the flat Universe) and nonbaryonic dark matter (with fraction Ω_{DM}):

$$\frac{m_N}{m_B} = \frac{\Omega_{DM}}{\Omega_B}. \tag{5}$$

Masses of the fourth generation of fermions must be below the electroweak energy scale, since the masses of all the fermions (ordinary and of fourth generation) are formed due to violation of the electroweak symmetry, as follows from the topological criterion of mass protection (see Chapter 12 of [7]). There is also the lower constraint on the fourth neutrino mass which comes from the measured decay properties of the Z boson: $m_N > m_Z/2 = 45.6$ GeV (see, e.g., [10] and somewhat stronger constraint $m_N > 46.7$ GeV from the Z-resonance lineshape in [11]). Then, the fourth-generation contribution to dark matter must be

$$\Omega_{DM} = \Omega_B \frac{m_N}{m_B} > 50\Omega_B. \tag{6}$$

Since in our spatially flat Universe $\Omega_{DM} < 1$, this gives the constraint on the baryonic mass in the Universe: $\Omega_B < 0.02$. On the other hand, since the baryonic density in luminous matter is $\Omega_B \sim 0.004$, the constraint on dark matter mass is $\Omega_{DM} > 0.2$.

There are, however, the other constraints on the mass of m_N of heavy neutrino obtained from particle and astroparticle implications of the fourth-generation neutrinos [12], from which it follows that m_N must be larger than 200 GeV. For the early limits on heavy neutrino contribution to the density of dark matter, which follow from consideration of neutrino–antineutrino annihilation, see [13]. On the other hand, the electroweak data fit prefers the 50 GeV neutrinos [14], though masses as high as 200 GeV are not excluded.

One must also take into account that the dark matter contribution Ω_{DM} is only a fraction of unity, as follows from observational data on CMB angular temperature fluctuations [15]. On the other hand, the baryonic content of dark matter is about 10 times bigger than the baryon density in visible matter, as follows independently both from the structure of acoustic peaks in the angular power spectrum of CMB temperature fluctuations [15] and from the primordial nucleosynthesis theory plus observed abundance of light elements (^{4}He, D, ^{3}He, and ^{7}Li) [16]. As a result, one finds that $\Omega_{DM}/\Omega_B < 7$. Together with the constraint on m_N, this indicates that the excess $n_{4\nu}$ of neutrinos over antineutrinos must be smaller (maybe by one or two orders of magnitude) than n_B. This would mean that the F charge is not strictly conserved.

5. CONCLUSION

It appears that the classification scheme based on the SU(2) and SU(4) groups has many interesting features. Here, we considered one of them—the discrimination between the ordinary-matter fermions and the fourth generation. If the family charge F is strictly conserved, the fermions of the fourth-generation neutrinos with density $n_{4\nu} = n_B$ must be necessarily present in the baryonic asymmetric Universe to compensate the family charge. Moreover, it is not excluded that it is the asymmetry in the fourth-generation neutrinos which is primary and serves as a source of the baryonic asymmetry of the Universe.

These massive neutrinos form stable dark matter with mass density exceeding the baryonic mass density by the ratio of masses of neutrino and baryon m_N/m_B. According to the well-known physics of the decay of Z boson, this factor must be larger than 50. Whether this is an acceptable solution to the dark matter problem depends on details of the G(2244) = $SU(2)_L \times SU(2)_R \times SU(4)_C \times SU(4)_F$ model. The above relation between the baryonic and nonbaryonic masses of the Universe is based on the assumption of the conservation of the F charge. If this requirement is weakened, the dark matter density coming from the fourth generation of fermions will depend on the details of the baryo- or neutrino-genesis and on the further cosmological evolution of ordinary and dark matter.

ACKNOWLEDGMENTS

I am grateful to S.L. Adler for e-mail correspondence, J.C. Pati for encouraging comments, M.Yu. Khlopov and T. Vachaspati for numerous discussions, and L.B. Okun and A.A. Starobinsky for careful reading of the manuscript and valuable suggestions.

This work was supported by the ESF COSLAB Program and by the Russian Foundation for Basic Research.

REFERENCES

1. J. C. Pati and A. Salam, Phys. Rev. Lett. **31**, 661 (1973).
2. J. C. Pati and A. Salam, Phys. Rev. D **10**, 275 (1974).
3. R. Foot, H. Lew, and R. R. Volkas, Phys. Rev. D **44**, 859 (1991).
4. J. C. Pati, hep-ph/0005095.
5. J. C. Pati, hep-ph/0204240.
6. S. L. Adler, Int. J. Mod. Phys. A **14**, 1911 (1999).
7. G. E. Volovik, *The Universe in a Helium Droplet* (Clarendon Press, Oxford, 2003).
8. H. Terazawa, in *Proceedings of 22nd International Workshop on the Fundamental Problems of High Energy Physics and Field Theory*, KEK Preprint No. 99-46 (1999).
9. F. Wilczek and A. Zee, Phys. Rev. D **25**, 553 (1982).
10. J. E. Dubicki and C. D. Froggatt, hep-ph/0305007.
11. S. S. Bulanov, V. A. Novikov, L. B. Okun, *et al.*, hep-ph/0301268.
12. D. Fargion, M. Yu. Khlopov, R. V. Konoplich, and R. Mignani, JETP Lett. **68**, 685 (1998); K. M. Belotsky, T. Damour, and M. Yu. Khlopov, Phys. Lett. B **529**, 108 (2002); K. Belotsky, D. Fargion, M. Khlopov, *et al.*, hep-ph/0210153.
13. M. I. Vysotsky, A. D. Dolgov, and Ya. B. Zeldovich, JETP Lett. **26**, 188 (1977); B. W. Lee and S. Weinberg, Phys. Rev. Lett. **39**, 165 (1977); K. Sato and M. Kobayashi, Prog. Theor. Phys. **58**, 1775 (1977); P. Hut, Phys. Lett. B **69B**, 85 (1977).
14. V. A. Novikov, L. B. Okun, A. N. Rozanov, and M. I. Vysotsky, JETP Lett. **76**, 127 (2002).
15. D. N. Spergel, L. Verde, H. V. Peiris, *et al.*, Astrophys. J., Suppl. **148**, 175 (2003).
16. R. Cyburt, B. D. Fields, and K. A. Olive, Phys. Lett. B **567**, 227 (2003); G. Steigman, astro-ph/0308511.

JETP Letters, Vol. 78, No. 11, 2003, pp. 695–699. Translated from Pis'ma v Zhurnal Éksperimental'noĭ i Teoreticheskoĭ Fiziki, Vol. 78, No. 11, 2003, pp. 1207–1211.
Original Russian Text Copyright © 2003 by Ivanov, Krasil'nikov, Pravdin.

Search for Anisotropy in Arrival Directions of Ultrahigh-Energy Cosmic Rays by Using the Marr Wavelet on the Equatorial Sphere

A. A. Ivanov*, A. D. Krasil'nikov, and M. I. Pravdin
Institute of Cosmophysical Research and Aeronomy, Yakut Research Center, Siberian Division,
Russian Academy of Sciences, pr. Lenina 31, Yakutsk, 677891 Russia
** e-mail: a.a.ivanov@ikfia.ysn.ru*

Received October 20, 2003

The arrival direction distribution of cosmic rays for energies $E > 10^{18}$ eV detected at the Yakutsk EAS array is analyzed using the Marr wavelet. Deviation from the isotropic distribution of 361 showers above 10^{19} eV is found at a significance level of 0.007, which corroborates previous evidence of the cosmic ray anisotropy in this energy range. In contrast to the previous methods, the wavelet analysis makes it possible to localize both a celestial-sphere domain containing a supposed source of excess cosmic ray flux and the scale parameter of the two-dimensional wavelet. *© 2003 MAIK "Nauka/Interperiodica".*

PACS numbers: 96.40.Pq; 96.40.De; 95.85.Ry; 98.70.Sa

Cosmic rays (CRs) above 10^{18} eV are very uniformly distributed over their arrival directions. Nevertheless, analysis of the data from different arrays provided evidence of anisotropy. In particular, analyzing the data accumulated at the Volcano Ranch, Haverah Park, Sydney, and Yakutsk arrays to 1974, Krasil'nikov *et al.* [1] have found that the first-harmonic amplitude of the right-ascension distribution of 76 EASs above 10^{19} eV for declinations $\delta > 0$ reaches 44% (chance probability is equal to 2.6%) with a phase of 13.3 ± 1.5 h. Similar evidence was obtained by the group at the University of Durham [2] and by their followers in other works. The AGASA data exhibit a significant anisotropy of primary CRs near $E \sim 10^{18}$ eV with the excess localization from the Galactic center [3]. In a series of works, the authors stated that the arrival direction distribution exhibits local irregularities, so-called clusters, where several showers are localized (see, e.g., [4–6]).

In this work, we test the *null hypothesis* that the CR distribution over arrival directions is isotropic on the celestial sphere. For a quantitative estimate, we must characterize deviation from isotropy by a certain criterion determined for a finite fixed number N of observed particles in an energy range. We propose that it can be calculated by means of a continuous wavelet transform in the equatorial coordinate system. There is a difficulty in this way: since the fitting of the position and width of an energy range, where the distribution is anisotropic, provides the energy range found *a posteriori*, the results must be corrected for statistical significance.

In our analysis, we also involve another hypothesis that is proposed by Krasil'nikov *et al.* in [1]. This hypothesis is formulated as follows: a significant anisotropy of the right-ascension distribution of the arrival directions of CRs is observed for energies $E > 10^{19}$ eV, where the Galactic magnetic field ceases to confine CRs. We treat this statement as an *a priori* hypothesis, because it has been obtained from previous independent measurements.

The arrays, whose data were analyzed in [1], no longer detect CRs, except for the Yakutsk array. However, quite numerous events of ultrahigh-energy EASs were accumulated at the Yakutsk array, and the hypotheses can be tested at a statistical significance level higher than that achievable previously. To exclude showers used in [1], we analyze the Yakutsk data obtained after 1974. In this case, correction for the statistical significance of deviation from isotropy in the indicated energy range is not required. We do not use data from two other operating arrays, because the parameters of EASs detected at the High Resolution Fly's Eye have not yet been available, and AGASA data have been reported only for energies above 4×10^{19} eV.

The Yakutsk array and results obtained at it were described in [7]. Here, we use 32389 EASs above 10^{18} eV that were detected from 1975 to 2002 and whose axes were within the array perimeter and zenith angles $\theta < 60°$. This selection provides the accessible accuracy of the determination of shower parameters. According to analysis of the sidereal-time distribution of events above 10^{18} eV [8], methodical distortions of, e.g., the first-harmonic amplitude that arise due to nonuniformity of sky observation by the array and seasonal variations in the atmospheric conditions do not lead to noticeable deviation from the uniform distribution over the right ascension α. The distribution over the declina-

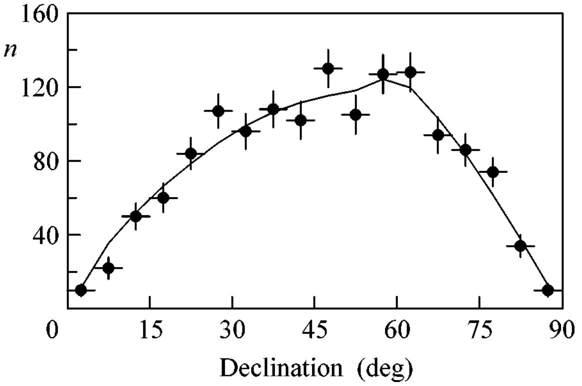

Fig. 1. Declination distribution of EASs with $E > 5 \times 10^{18}$ eV. The points are the observed data and the line is the isotropic distribution expected for the Yakutsk array. The vertical bars are statistical errors, and horizontal bars are declination intervals.

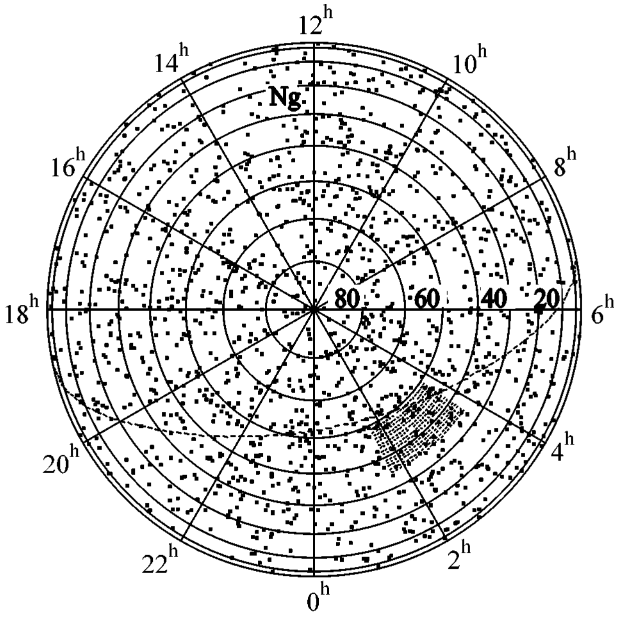

Fig. 2. Equatorial equal-exposition map of 1427 EASs with energies $E > 5 \times 10^{18}$ eV. The dial shows the right ascensions in hours, and declinations in degrees are shown along a radius. The Galactic North Pole is denoted as N_g, and the dashed line is the Galactic equator.

tion δ is strongly nonuniform due to the acceptance of the ground array and attenuation of inclined showers in the atmosphere. The expected isotropic distribution over declination for the array with the taken criterion of event selection that is obtained by transforming the function $\propto \sin(2\theta)$ from the horizontal system to the equatorial one, as well as the CR distribution observed in Yakutsk, is shown in Fig. 1.

This distribution is used to plot an equal-exposition map of the arrival directions of EASs (Fig. 2), where the radial declination scale is taken so that all domains of the map have equal exposition times in the diurnal cycle [9].

In this work, the data are analyzed by using wavelets to search for large-scale anisotropy disregarding small-angle correlations of the arrival directions of CRs in clusters. The wavelet analysis is a logical development of the harmonic analysis and is effective for determination of the local features of aperiodic functions [10]. It is successfully applied in various fields, including physics [11]. The method, as well as the harmonic analysis, is based on the expansion of an original function in an orthonormal basis, but wavelets, in contrast to harmonic functions, are localized in both physical and Fourier-transform spaces.

A continuous wavelet transform of the function $f(\mathbf{x})$ is defined as

$$wv(R, \mathbf{b}) = \int d\mathbf{x} f(\mathbf{x}) \Psi(R, \mathbf{b}; \mathbf{x}), \tag{1}$$

$$\Psi(R, \mathbf{b}; \mathbf{x}) = \frac{1}{R} \psi\left(\frac{|\mathbf{x} - \mathbf{b}|}{R}\right), \tag{2}$$

where $wv(R, \mathbf{b})$ is the wavelet transform of the function with the scale parameter R at the point with the coordinates $\mathbf{b}$ and $\psi(|\mathbf{x}|)$ is the isotropic mother wavelet. Necessary and sufficient conditions of applicability of this direct transform and inverse transform are the compensation of positive and negative values, i.e., $\int d\mathbf{x}\psi = 0$; normalization, i.e., $\int d\mathbf{x}\psi^2 = 1$; and admissibility, i.e., $(2\pi^2)\int dq q^{-1} \psi^2(q) < \infty$, where $\psi(q)$ is the Fourier transform of the function $\psi(x)$.

To test the null hypothesis and hypothesis by Krasil'nikov *et al.*, we use the one-dimensional (1D) Marr wavelet (Mexican hat) [12] on the right-ascension circle. Distances between points are measured in right ascension, and expressions similar to Eq. (1) are integrated within 2π. Possible sources of CRs are further localized by the two-dimensional (2D) Marr wavelet on the equatorial sphere. This wavelet has the smooth bell-shaped maximum (Fig. 3) inherited from the normal distribution, and the maximum width is specified by the scale parameter R:

$$\psi(\mathbf{x}) = (2 - \mathbf{x}^2/R^2)\exp(-0.5\mathbf{x}^2/R^2)/\sqrt{2\pi R^2}, \tag{3}$$

where x is the distance from the wavelet center. Transformation (1) presents the contribution of various scales and coordinates to the function under analysis.

For the wavelets defined on the infinite plane to be used on the equatorial sphere with a given accuracy, we have to measure distances between pairs of points in terms of spherical arcs and to limit the domain of allowed scale parameters so that the conditions of applicability of the wavelet are satisfied. Since we test deviation from isotropy without the inverse wavelet

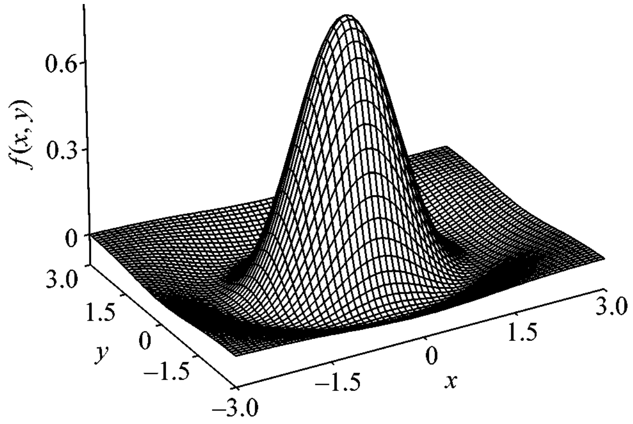

Fig. 3. Marr wavelet (3) with the parameters $R = 1$ and $b = 0$.

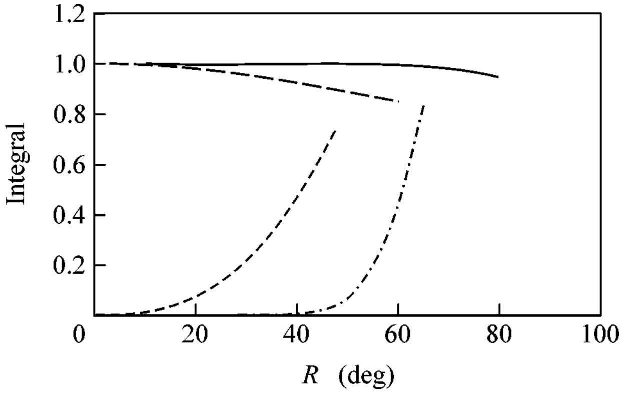

Fig. 4. Normalization integrals for (solid line) 1D and (dashed line) 2D Marr wavelets and integrals of balance between positive and negative values for (dash–dotted line) 1D and (dashed line) 2D Marr wavelets.

transform of wavelet coefficients to the original function, we can restrict ourselves by two first conditions: compensation and function normalization.

The results of numerical integration over the circle and sphere were presented in Fig. 4 and Table 1, where it is seen that the conditions were satisfied with an accuracy of 10% for $0° < R < 51.6°$ and $0° < R < 22.9°$ in the 1D case and on the equatorial sphere, respectively.

Although the wavelet coefficients of the isotropic distribution $f(\mathbf{x}) = \mathrm{const}$ are equal to zero for continuous functions, they are really nonzero because the number of EASs is finite. For this reason, we calculate the expected coefficients for isotropic primary CRs by the Monte Carlo method, representing the isotropic distribution of N points by the sum of delta functions $f(\mathbf{x}) = \sum_{i=1}^{N} \delta(\mathbf{x} - \mathbf{x}_i)$,

$$wv(R, \mathbf{b}) = \sum_{i=1}^{N} \psi(|\mathbf{x_i} - \mathbf{b}|/R)/R,$$

and then averaging the coefficients over a sample of a sufficiently large number of tests for each given energy range.

Calculation of the wavelet coefficients for the arrival-direction distribution of primary CRs shows that the spread $(wv_{\max} - wv_{\min})/(wv_{\max} + wv_{\min})$ of minimum an maximum values for fixed R and N values can be represented by the first-harmonic amplitude in right ascension, which tends to zero with an increase in N. Then, the deviation of the observed/isotropic amplitude ratio of the wavelet coefficients $W_1^{\mathrm{observ}}/W_1^{\mathrm{isotr}}$ from unity in an energy range for the given parameters can be used as a measure of deviation from the isotropic expectation.

Figure 5 shows this ratio obtained by processing the Yakutsk data with the 1D wavelet on the right-ascension circle for the arrival-direction distribution integrated with respect to declination in order to reproduce the conditions from [1].

Indeed, the Marr-wavelet amplitude significantly differs from the isotropic amplitude for $E > 10^{19}$ eV, where $W_1^{\mathrm{observ}}/W_1^{\mathrm{isotr}} = 2.52 \pm 0.52$. The wavelet maximum at a right ascension of 2.7 h with an error of $R/2 =$ 1 h corresponds to the phase of this amplitude. The significance level of the deviation of the amplitude from the isotropic expectation, which is calculated by the Monte Carlo method for 361 particles falling within the third range, is equal to 0.7% (Table 2). The statistical power has increased strongly since 1974, but the phase is now at another point. Our result is independent of the procedure of analysis with respect to right ascension. Indeed, the harmonic analysis of the recent Yakutsk data with respect to right ascension [13] also reveals a significant first-harmonic amplitude ($A_1 = 26.4 \pm 8\%$, $\alpha = 2.3 \pm 1.2h$) in the energy range $(1–3) \times 10^{19}$ eV.

The application of the 2D wavelet provides the further advance in the analysis. It enables us to more precisely determine the primary arrival direction of CRs in the declination distribution and to estimate the wavelet scale parameter within a certain range. However, the

Table 1. Limit scale parameters of the wavelets R (in deg) that ensure the applicability conditions on the (1D) right-ascension circle and (2D) sphere for (norm) normalization integral and (compens) balance between positive and negative values at a given accuracy δ_{integr}

δ_{integr}, %	20	10	1	0.1
$R_{1D}^{\mathrm{compens}}$	55.0	51.6	43.8	38.7
$R_{2D}^{\mathrm{compens}}$	29.2	22.9	10.5	4.8
R_{1D}^{norm}	108.9	89.8	66.9	56.8
R_{2D}^{norm}	73.7	47.4	14.1	4.4

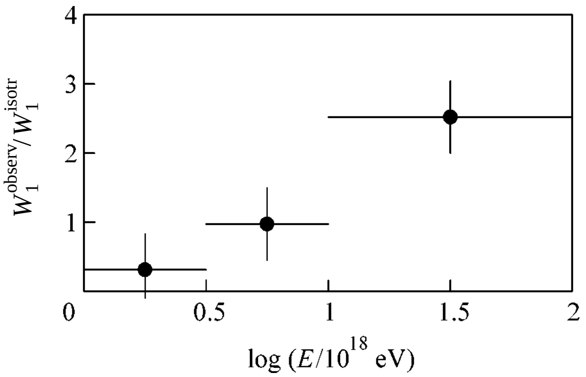

Fig. 5. Amplitude of the Marr wavelet for the right-ascension distribution of the arrival directions of CRs. The vertical bars are statistical errors, and horizontal bars are energy ranges.

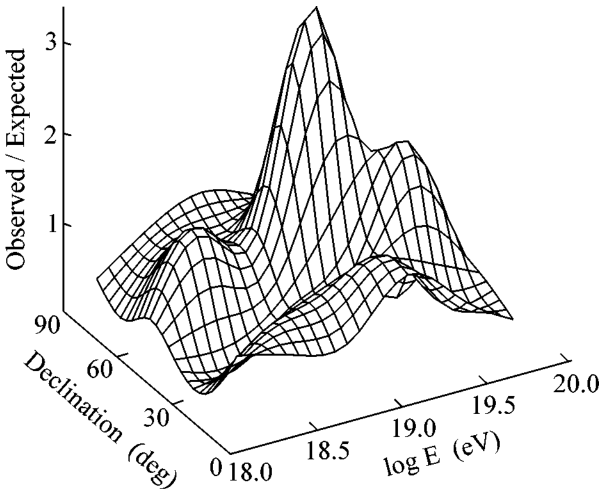

Fig. 6. Determination of the domain of an excess CR flux in the declination distribution: 2D wavelet analysis of the Yakutsk array data.

significance level of the results gains uncertainty in this case, because they are obtained *a posteriori*.

Calculating integral (1) with the 2D Marr wavelet on the equatorial sphere and further estimating the amplitude of the first harmonics in right ascension, we obtain the observed-to-isotropic amplitude ratio shown in Fig. 6 as a function of energy and declination. Here, we fit the range width in energy logarithm 0.25 and scale parameter $R = 17°$ (corresponding to the condition that the wavelet is equal to zero on the sphere within an accuracy of ~10%) such that the maximum ratio $W_1^{\rm observ}/W_1^{\rm isotr} = 3.18 \pm 0.54$ is reached in the ranges $10^{19} < E \le 10^{19.25}$ eV and $45° \le \delta < 60°$. The resulting domain is shaded in the map of the equatorial coordinates (Fig. 2).

It is noteworthy that the north–south asymmetry in the Galactic latitude distribution of CR flux was found in the same energy range in the Yakutsk data [14, 15] with evidence of an excess flux from the latitude interval (–15°, 0°). These two results for the supposed domain of the excess flux agree well with each other. Moreover, they supplement each other. Calculations of the trajectories of charged particles in Galactic magnetic fields [16, 14] show that the north–south asymmetry arises in a model with sources in the Galactic disk.

Then, measurements of the arrival direction distribution of CRs provide the following pattern in the transition energy range between Galactic and extragalactic components [15]. The isotropic extragalactic component and Galactic component captured in the magnetic field $\bar{B} \sim 2\ \mu$G dominate above and below the threshold energy $E_{\rm thr}$, respectively. The contribution of $\bar{Z} \sim 10$ nuclei from the Galactic disk provides the north–south asymmetry only near $E_{\rm thr} \sim 10^{19}$ eV. This threshold energy agrees with an “ankle” irregularity in the CR spectrum in this range that is observed at all arrays (see review [17]).

This work was supported by the Russian Foundation for Basic Research and the Ministry of Industry, Science, and Technologies of the Russian Federation.

Table 2. Observed ($W_1^{\rm observ}$) and isotropic ($W_1^{\rm isotr}$) wavelet amplitudes of the right-ascension distribution for $R = 30°$ in energy ranges (*1*) $10^{18} < E \le 10^{18.5}$ eV, (*2*) $10^{18.5} < E \le 10^{19}$ eV, and (*3*) $E > 10^{19}$ eV corresponding to Fig. 5; $\alpha_{\rm max}$ is the right ascension of the wavelet maximum, δW_1 is statistical errors, and P is the chance probability of realizing the wavelet amplitude $W_1^{\rm isotr} \ge W_1^{\rm observ}$ in the isotropic distribution

{E}	$W_1^{\rm observ}$	$\alpha_{\rm max}$, h	$W_1^{\rm isotr}$	δW_1	P, %
1	0.75	20.1	2.39	1.23	93.7
2	0.81	2.3	0.83	0.43	48.5
3	1.24	2.7	0.49	0.25	0.7

REFERENCES

1. D. D. Krasilnikov, A. I. Kuzmin, J. Linsley, *et al.*, J. Phys. A **7**, L176 (1974).
2. J. Wdowczyk and A. W. Wolfendale, J. Phys. G **10**, 1453 (1984).
3. N. Hayashida, M. Nagano, D. Nishikawa, *et al.*, Astropart. Phys. **10**, 303 (1999).
4. X. Chi, J. Wdowczyk, and A. W. Wolfendale, J. Phys. G **18**, 1867 (1992).
5. N. Hayashida, K. Honda, M. Honda, *et al.*, Phys. Rev. Lett. **77**, 1000 (1996).
6. P. G. Tinyakov and I. I. Tkachev, Pis’ma Zh. Éksp. Teor. Fiz. **74**, 3 (2001) [JETP Lett. **74**, 1 (2001)].

7. M. N. D'yakonov, T. A. Egorov, N. N. Efimov, *et al.*, in *Space Radiation of Extremely High Energy* (Nauka, Novosibirsk, 1991).
8. M. I. Pravdin, A. A. Ivanov, A. D. Krasil'nikov, *et al.*, Izv. Ross. Akad. Nauk, Ser. Fiz. **66**, 1592 (2002).
9. D. D. Krasilnikov, T. A. Egorov, A. A. Ivanov, *et al.*, in *Proceedings of 15th International Cosmic Ray Conference* (Plovdiv, 1977), Vol. 2, p. 189.
10. I. Daubechies, *Ten Lectures on Wavelets* (SIAM, Philadelphia, 1991; RKhD, Moscow–Izhevsk, 2001).
11. I. M. Dremin, O. V. Ivanov, and V. A. Nechitaĭlo, Usp. Fiz. Nauk **171**, 465 (2001) [Phys. Usp. **44**, 447 (2001)].
12. D. Marr and E. C. Hildreth, Proc. R. Soc. London, Ser. B **207**, 187 (1980).
13. A. D. Krasilnikov, A. A. Ivanov, and M. I. Pravdin, in *Proceedings of 27th International Cosmic Ray Conference* (Hamburg, 2001), Vol. 1, p. 398.
14. X. Chi, A. A. Ivanov, and A. W. Wolfendale, J. Phys. G **19**, 1975 (1993).
15. A. A. Ivanov, J. Phys. G **24**, 227 (1998).
16. S. I. Syrovatskiĭ, Preprint No. 151, FIAN (Physical Inst., USSR Academy of Sciences, Moscow, 1969).
17. M. Nagano and A. A. Watson, Rev. Mod. Phys. **72**, 689 (2000).

Translated by R. Tyapaev

JETP Letters, Vol. 78, No. 11, 2003, pp. 700–702. Translated from Pis'ma v Zhurnal Éksperimental'noĭ i Teoreticheskoĭ Fiziki, Vol. 78, No. 11, 2003, pp. 1212–1215.

On Coherent Radiation in Collisions of Short Bunches of Relativistic Particles

N. F. Shul'ga* and D. N. Tyutyunnik
National Science Center Kharkov Institute of Physics and Technology,
ul. Akademicheskaya 1, Kharkov, 61108 Ukraine
** e-mail: shulga@kipt.kharkov.ua*

Received October 2, 2003; in final form, October 20, 2003

Suppression of coherent radiation arising in collisions of relativistic electrons with a short bunch of relativistic particles is predicted. It is shown that this effect must occur in the low-frequency range of emitted photons if radiation has a not purely dipole character. The mechanism of this effect differs from the mechanism of electron synchrotron radiation in the field of the incident particle bunch. *© 2003 MAIK "Nauka/Interperiodica".*

PACS numbers: 41.60.–m; 41.75.Ht

1. As was shown in [1–4], a considerable coherent effect in radiation can exist in collisions of relativistic electrons with a short bunch of relativistic particles. This effect should occur at low frequencies of emitted photons, when the coherence length of the emission process is much larger than the bunch length. In [1–3], a theory of this effect was proposed on the basis of the Born approximation in QED, and the possibility of detecting the effect at the available accelerators was analyzed. This effect was considered classically in [4], but it has not yet been observed in experiment.

In [1–4], radiation of a relativistic electron in the bunch field was assumed to be dipolal; i.e., $\gamma\vartheta_e \ll 1$, where γ is the electron Lorentz factor and ϑ_e is the total scattering angle of an electron in the bunch field. As was mentioned in [1], this condition is not satisfied for some accelerators. Therefore, it is necessary to understand the features of electron emission in the bunch field for $\gamma\vartheta_e \geq 1$.

In the latter case, electron emission was previously considered on the basis of the theory of synchrotron radiation. In this work, we show that this is not necessarily the case and that electron emission in the field of particle bunch can be accompanied, in addition to the coherent effect, by the suppression of coherent radiation, similar to the Landau–Pomeranchuk–Migdal suppression of relativistic electron bremsstrahlung in a thin layer of substance [5–7].

2. Let us consider low-frequency radiation emitted by an electron interacting with an incident narrow and short bunch of relativistic particles. This radiation is primarily directed close to the direction of electron motion. In this case, if the emission coherence length is much larger than the bunch longitudinal size, the electron interaction with particles of the bunch is determined by the parameter

$$\alpha_N = N\frac{eQ}{\hbar c}, \qquad (1)$$

where e is the elementary charge, Q is the charge of a bunch particle, and N is the number of particles in the bunch. This parameter is similar to the corresponding parameter determining the interaction of an electron with a crystal atomic chain [8] and implies that the electron interacts with the bunch particles just as with a united object with the effective charge $Q_{\text{eff}} = NQ$. In this aspect, the problem of coherent radiation of an electron in the bunch field is close to the problem of coherent radiation of a relativistic electron in crystal [9].

When $NeQ/\hbar c \ll 1$, the electron emission in the bunch field can be described in the Born approximation of QED. However, the condition for the applicability of the Born approximation is rapidly violated with an increase in N. The typical number of bunch particles for many accelerators is $N \sim 10^8$–10^{10} (see, e.g., [1]). Therefore, such bunches satisfy the condition $\alpha_N \gg 1$, which is opposite to the condition for the applicability of Born approximation. In this case, the low-energy photon emission can be considered within the framework of the classical radiation theory.

In classical electrodynamics, spectral and angular radiation density is determined by the electron trajectory $\mathbf{r}(t)$ in an external field:

$$\frac{dE}{d\omega d\mathbf{\Omega}} = \frac{e^2}{4\pi^2}|\mathbf{k}\times\mathbf{I}|^2, \qquad (2)$$

where ω and $\mathbf{k}$ are the frequency and wavenumber of an emitted wave, $d\mathbf{\Omega}$ is the element of solid angle in the emission direction, and

$$\mathbf{I} = i\int_{-\infty}^{\infty} dt e^{i(\omega t - \mathbf{k}\mathbf{r}(t))}\frac{d}{dt}\frac{\mathbf{v}(t)}{\omega - \mathbf{k}\mathbf{v}(t)}. \qquad (3)$$

The electron trajectory $\mathbf{r}(t)$ in the field of incident bunch is determined by the equation of motion

$$\frac{d}{dt}\mathbf{v} = \frac{e}{\varepsilon}[\mathbf{E} + \mathbf{v}\times\mathbf{H} - \mathbf{v}(\mathbf{v}\cdot\mathbf{E})], \qquad (4)$$

where ε is the electron energy and $\mathbf{E} = -\nabla\varphi - \frac{\partial}{\partial t}\mathbf{A}$ and $\mathbf{H} = \nabla\times\mathbf{A}$ are, respectively, the electric and magnetic fields of the moving particle bunch. The scalar φ and vector $\mathbf{A}$ potentials of the bunch are determined by the expressions

$$\varphi = \sum_n \frac{Q}{[(z - z_n - v_p t)^2 + |\rho - \rho_n|^2/\gamma_p^2]^{1/2}}, \qquad (5)$$
$$\mathbf{A} = \mathbf{v}_p\varphi,$$

where γ_p is the Lorentz factor of particles in the bunch; (z_n, ρ_n) are the coordinates of particles at $t = 0$; z and ρ are the coordinates parallel and perpendicular to the electron velocity $\mathbf{v}$, respectively; and $\mathbf{v}_p$ is the velocity of incident particles ($\mathbf{v}_p$ is assumed to be directed along the negative z semiaxis and identical for all particles in the bunch). Summation in Eqs. (5) is over all bunch particles. Hereinafter, we use the system of units where the speed of light is equal to unity.

Characteristic scattering angles of a relativistic electron in the field of bunch particles are small. Therefore, the electron velocity can be written in the form

$$\mathbf{v}(t) = \mathbf{v}\left(1 - \frac{1}{2}v_\perp^2\right) + \mathbf{v}_\perp(t), \qquad (6)$$

where $\mathbf{v}_\perp(t)$ are the electron-velocity components perpendicular to the velocity $\mathbf{v}$ of the incident electron, $|v_\perp| \ll |v|$. If

$$\frac{2\gamma^2/\omega}{1 + \gamma^2\vartheta_N^2} \gg \frac{L}{2}, \qquad (7)$$

where L is the bunch length and ϑ_N is the total electron scattering angle by the bunch, the exponential factor in Eq. (3) can be ignored. In this case, $\mathbf{I}$ is determined only by the directions of the initial $\mathbf{v}$ and final $\mathbf{v}_N$ electron velocities. The radiation spectral density is given by the expression

$$\frac{dE}{d\omega} = \frac{2e^2}{\pi}\left[\frac{2\xi^2 + 1}{\xi\sqrt{\xi^2 + 1}}\ln(\xi + \sqrt{\xi^2 + 1}) - 1\right], \qquad (8)$$

where $\xi = \xi_N = \gamma\vartheta_N/2$ is the parameter characterizing the nondipolar electron radiation in the bunch field.

Thus, if condition (7) is fulfilled, spectral radiation density (8) is determined by the product of the electron Lorentz factor and the total electron-scattering angle by the particle bunch. Note that formula (8) and its applicability condition (7) are valid for both small and large parameters ξ_N. Condition (7) means that, with allowance for the electron scattering in the bunch field, the emission coherence length $l_c = 2\gamma^2/\omega(1 + \gamma^2\vartheta_N^2)$ is much larger than the electron–bunch interaction length [the right-hand side of inequality (7) includes the factor 1/2, because the bunch moves toward the electron, so that the electron time of flight through the bunch is equal to $L/2v$].

To determine the electron scattering angle in field (5), it is necessary to know the transverse electron-velocity component $\mathbf{v}_\perp(t)$. In view of the relation $\mathbf{v}\times(\nabla\times\mathbf{A}) = -\nabla\varphi - \mathbf{v}_p(\mathbf{v}\cdot\nabla)\varphi$, Eq. (4) for $\mathbf{v}_\perp(t)$ can be written, to the terms on the order of γ^{-2} and $v_\perp^2/v^2$, in the form

$$\frac{d}{dt}\mathbf{v}_\perp = -\frac{2e}{\varepsilon}\nabla_\perp\varphi. \qquad (9)$$

Therefore, the total electron scattering angle in the bunch field is determined by the expression

$$\vartheta_N = \frac{\mathbf{v}_\perp(+\infty)}{v} \approx \frac{4eQ}{\varepsilon}\sum_{n=1}^{N}\frac{\rho - \rho_n}{|\rho - \rho_n|^2}. \qquad (10)$$

3. For simplicity, we consider the radiation for the case where the electron passes along the bunch at a distance $\rho \gg \rho_n$ from its axis. In this case, according to Eq. (10),

$$\vartheta_N \approx N\vartheta_1, \qquad (11)$$

where $\vartheta_1 \approx 4eQ/\rho\varepsilon$ is the electron scattering angle by one particle of the bunch. The parameter ξ in Eq. (8) is determined by the expression

$$\xi_N = N\frac{2eQ}{m\rho}. \qquad (12)$$

Therefore, all bunch particles behave as a single electron-scattering center with effective charge NQ.

Substituting Eq. (12) into Eq. (8), we obtain the radiation spectral density for a relativistic electron in the field of incident bunch particles. The corresponding expression is valid under condition (7). If $\xi_N \ll 1$, expression (8) can be expanded in powers of ξ. To the first approximation, we obtain

$$\frac{dE_N}{d\omega} = \frac{2e^2}{3\pi}\gamma^2\vartheta_N^2 = N^2\frac{32e^4Q^2}{3\pi m^2\rho^2}. \qquad (13)$$

In this case, the coherent effect occurs in the electron emission induced by the collisions with a bunch of N

particles, according to which the radiation spectrum is proportional to the square of the number of particles in the bunch. In this connection, we note that, although the applicability conditions for the Born approximation are strongly violated, the classical consideration shows that the coherent effect for electron emission in the field of incident bunch of particles is still valid. In other words, this means that the coherent effect is possible for a larger number of particles in the bunch.

Let us now determine the limiting number of particles in the bunch for which the coherent effect is possible. With an increase in N, the inequality $\xi_N \gg 1$ becomes invalid. For $\xi_N \gg 1$, according to Eq. (8), we have

$$\frac{dE_N}{d\omega} = \frac{4e^2}{\pi}\ln 2\xi_N = \frac{4e^2}{\pi}\ln\left(N\frac{4eQ}{m\rho}\right). \tag{14}$$

In this case, the coherent radiation is suppressed and the radiation spectral density is virtually independent of the number of atoms in the bunch. This effect is similar to the bremsstrahlung suppression for high-energy electrons in a thin layer of matter [7].

Thus, the coherent effect in this problem is possible up to the number $N_{\max}$ of particles in the bunch, which is determined by the relation

$$N_{\max}\frac{2eQ}{m\rho} \sim 1. \tag{15}$$

For typical cases (see below), $N_{\max} \sim 10^{10}$. For a larger number of particles in the bunch, the coherent effect of radiation breaks, and, according to Eqs. (13) and (14), the square dependence of the radiation spectral density on N changes to much weaker logarithmic dependence. We note that the suppression mechanism for coherent radiation in the problem under consideration is similar to the mechanism of bremsstrahlung suppression in the Landau–Pomeranchuk–Migdal (LPM) effect [5, 6, 9]. In both problems, radiation is suppressed when the electron is scattered within the coherence length at angles exceeding the characteristic emission angle $\vartheta \sim 1/\gamma$ of relativistic electron. This means that an analogue of the LPM effect is also possible for another process—coherent emission by the relativistic electron in the field of the incident bunch of relativistic charged particles. Thereby, new possibilities of investigating the analogues of the LPM effect have opened up. (The LPM effect was recently verified in experiments at the SLAC [10] and CERN [11] accelerators.)

We emphasize that formula (14) is valid under the condition $\gamma\vartheta_N \gg 1$. At the same time, it substantially differs from the corresponding result of the synchrotron radiation theory, which was previously used to describe electron emission in the bunch field under the condition $\gamma\vartheta_N \gg 1$. This difference exists because the formulas of synchrotron radiation theory require the condition $2\gamma^2/\omega \ll L/2$, in addition to the inequality $\gamma\vartheta_N \gg 1$. Moreover, the mean field of the bunch of particles varies slightly on the coherence length of emission [9]. The last condition is opposite to condition (7), under which formula (8) is valid.

We now present particular estimates of the results for electrons that have energy $\varepsilon \sim 5$ GeV and move at distance $\rho \sim 10^{-2}$ cm from the axis of the incident bunch of relativistic particles with $N_p \sim 5 \times 10^{10}$, $L \sim 10^{-1}$ cm, and transverse size $\Delta\rho \ll 10^{-2}$ cm. In this case, the effective constant of the interaction of the electron with the field of the bunch is equal to $\alpha_N \sim 5 \times 10^8$, the parameter of deviation from dipole radiation $\gamma\vartheta_N \sim 8$, and the above formulas are valid beginning with the emitted-quantum energy $\omega_c = 4\gamma^2/L(1 + \gamma^2\vartheta_N^2) \sim$ 100 keV. Thus, for the case under consideration, coherent emission is substantially suppressed. At the same time, formulas of synchrotron-radiation theory are not yet valid. The coherent effect is still possible for $N_{\max} \sim 10^{10}$.

N.F.Sh. is grateful to V.G. Serbo for stimulating discussions.

REFERENCES

1. I. F. Ginzburg, G. L. Kotkin, S. I. Polityko, and V. G. Serbo, Yad. Fiz. **55**, 3310 (1992) [Sov. J. Nucl. Phys. **55**, 1847 (1992)]; Yad. Fiz. **55**, 3324 (1992) [Sov. J. Nucl. Phys. **55**, 1855 (1992)].
2. I. F. Ginzburg, G. L. Kotkin, S. I. Polityko, and V. G. Serbo, Z. Phys. C **60**, 737 (1993).
3. S. I. Kotkin and V. G. Serbo, Phys. Rev. E **51**, 2493 (1995).
4. M. Bassetti, J. Bosser, M. Gygi-Henney, *et al.*, IEEE Trans. Nucl. Sci. **30**, 2182 (1983).
5. L. D. Landau and I. Ya. Pomeranchuk, Dokl. Akad. Nauk SSSR **92**, 735 (1953).
6. A. B. Migdal, Dokl. Akad. Nauk SSSR **96**, 49 (1954).
7. N. F. Shul'ga and S. P. Fomin, Zh. Éksp. Teor. Fiz. **113**, 58 (1998) [JETP **86**, 32 (1998)].
8. A. I. Akhiezer, V. F. Boldyshev, and N. F. Shul'ga, Fiz. Élem. Chastits At. Yadra **10**, 52 (1979) [Sov. J. Part. Nucl. **10**, 19 (1979)].
9. A. I. Akhiezer and N. F. Shul'ga, *Electrodynamics of High Energies in Materials* (Nauka, Moscow, 1993).
10. P. L. Anthony, R. Becker-Szendy, P. E. Bosted, *et al.*, Phys. Rev. D **56**, 1373 (1997).
11. H. Hansen, U. I. Uggerhoj, C. Biino, *et al.*, Phys. Rev. Lett. **91**, 014801 (2003).

Translated by R. Tyapaev

JETP Letters, Vol. 78, No. 11, 2003, pp. 703–706. Translated from Pis'ma v Zhurnal Éksperimental'noĭ i Teoreticheskoĭ Fiziki, Vol. 78, No. 11, 2003, pp. 1216–1220.

X-ray-Line Plasma Satellites of Ions in Solid Target Plasmas Produced by Picosecond Laser Pulse

V. S. Belyaev[1], V. I. Vinogradov[1], A. S. Kurilov[1], A. P. Matafonov[1], V. S. Lisitsa[2], V. P. Gavrilenko[3, 4], A. Ya. Faenov[5], T. A. Pikuz[5], I. Yu. Skobelev[5, *], A. I. Magunov[4, 5], and S. A. Pikuz, Jr.[6]

[1] *Research Institute of Mechanical Engineering, Korolev, Moscow region, 141070 Russia*
[2] *Institute of Nuclear Fusion, Russian Research Centre Kurchatov Institute, pl. Akademika Kurchatova 1, Moscow, 123182 Russia*
[3] *National Research Center of Surface and Vacuum Properties, Andreevskaya nab. 2, Moscow, 117331 Russia*
[4] *Prokhorov Institute of General Physics, Russian Academy of Sciences, ul. Vavilova 38, Moscow, 117942 Russia*
[5] *Center of the Data on Multicharged Ion Spectra, Research Institute of Physicotechnical and Radio Engineering Measurements, Mendeleevo, Moscow region, 141570 Russia*
**e-mail: skobelev@orc.ru*
[6] *Faculty of Physics, Moscow State University, Vorob'evy gory, Moscow, 119899 Russia*

Received October 8, 2003; in final form, October 22, 2003

The X-ray lines of ions in a solid target interacting with picosecond laser pulses of moderate intensity (2×10^{17} W/cm^2) were measured on the "Neodim" laser facility. X-ray Ly_α emission spectra of hydrogen-like fluorine ions were observed. Satellite lines were also observed, evidencing the presence of intense plasma oscillations. The positions and separation between the satellites allow their assignment to the intense electrostatic oscillations with an amplitude larger than 10^8 V/cm and a frequency of about 7×10^{14} s^{-1} that is noticeably lower than the laser frequency $\omega_{\text{las}} \sim 1.8 \times 10^{15}$ s^{-1}. It is suggested that these oscillations may be due to strong plasma turbulence caused by the development of plasma oscillations of the Bernstein-mode type under the action of a strong magnetic field generated in plasma. The experimental results are compared with the calculated spectra of multicharged ions. *© 2003 MAIK "Nauka/Interperiodica".*

PACS numbers: 52.38.Ph; 52.70.La; 52.50.Jm; 52.35.Mw

1. The electron-velocity distribution in plasmas produced by high-power sub- and picosecond laser pulses is strongly anisotropic. Due to this anisotropy, the strong electromagnetic oscillations caused by the development of instabilities, primarily, so-called Weibel instability, arise in such plasmas. As known, the development of instability gives rise to quasi-stationary magnetic fields of strength determined by laser intensity and achieving hundreds of megagauss for intensities exceeding 10^{19} W/cm^2. In recent experiments [1], the generation of such ultrastrong quasi-stationary magnetic fields was observed in laser plasma. Irrespective of the generation mechanism, their occurrence is of fundamental interest, because they modify cardinally the physical properties of laser plasma. The magnetic fields measured in experiments [1], were on the order of 300 MG and had a noticeable effect on the propagation of ordinary and extraordinary waves in the visible region.

The appearance of strong plasma instabilities and ensuing plasma oscillations should affect the ion emission spectra in plasmas produced by the sub- and picosecond laser pulses. The observation of spectroscopic effects caused by the plasma oscillations is of indubitable interest, first, as an independent method for proving their appearance and, second, as the method of local measurement of these effects.

This work reports the results of measuring the spectra of multicharged ions in plasma produced by picosecond laser pulses of moderate intensity ($\sim 10^{17}$ W/cm^2). Our experiments give evidence for the presence of strong longitudinal electric fields in plasma, with frequency sizably lower than the laser frequency. It is suggested that the frequency of these oscillations is close to the electron cyclotron frequency that, likely, corresponds to the development of Bernstein-type plasma oscillations in a magnetic field. The calculated spectra correlate well with the experimental data.

2. Experiments were conducted on the "Neodim" terawatt laser facility [2]. It gave the following pulse parameters: an energy up to 1.5 J, a wavelength of 1.055 μm, and a duration of 1.5 ps. A laser beam 60 mm in diameter was focused onto a target using a 14.5-mm aspherical lens with a focal length of 140 mm to concentrate 50% of energy within a spot of radius 15 μm. As a result, the mean intensity focused onto the target was 2×10^{17} W/cm^2. Flat fluoroplastic plates of thickness 200 μm were used as targets. The residual gas

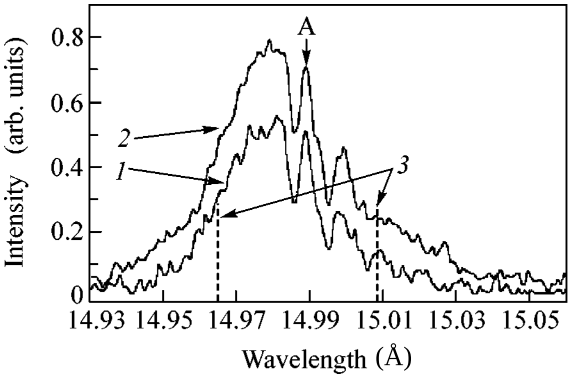

Fig. 1. Typical Ly_α profiles for a hydrogen-like FIX ion in the experiments with plasma heated by a picosecond laser pulse. (*1*) 3F flare and (*2*) 4F flare; in both cases, the laser intensity was ~2 × 10^{17} W/cm^2. Dashed lines (*3*) show the positions of laser satellites that could be excited upon laser photon scattering by the metastable $2s_{1/2}$ state of the FIX ion.

pressure in the vacuum chamber was no worse than 10^{-3} torr.

The X-ray emission from plasma produced upon the interaction of laser pulse with target was recorded using two FSRP spectrographs [3] with spherically bent quartz or mica crystals (radius of curvature of the crystal surfaces was 150 mm). In all experiments, the takeoff angle with the normal to the target surface was equal to 5° for spectrograph no. 1 and 85° for spectrograph no. 2. A Kodak-2492 X-ray photographic film protected from the visible radiation by two 1-μm-thick polypropylene layers spray-coated with an Al layer of an overall thickness of 0.2 μm was used as a detector of the radiation reflected from the surface.

The plasma emission spectra were examined in the range from 1.49 to 1.51 nm. In our experiments, the spectral resolution $\lambda/\Delta\lambda$ was no worse than 5000. The typical Ly_α profiles ($n = 2 \longrightarrow n = 1$ transition, where n is the principal quantum number) for a hydrogen-like FIX ion are shown in Fig. 1. The salient feature of these profiles is that there is a sharp peak surrounded by dips on both its sides at the long-wavelength wing of the line. This peak is marked letter "A" in the experimental profiles shown in Fig. 1. It should be noted that this peak cannot be assigned to so-called laser satellites [4–6], because it is shifted from the energy of forbidden 2*s*–1*s* transition at a distance that is different from the laser photon energy (Fig. 1).

3. The theoretical modeling was based on the calculation of the emission spectra in the presence of the static ion and variable plasma-oscillation fields. As a first step, we considered the action of the static and variable electric fields on the level fine-structure components in the case of aligned quasi-static ion field and the plasma oscillation electric vector. It was assumed that the static field of plasma ions obeys the Holtsmark distribution for an ion density of about 10^{20} cm^{-3}. The main uncertainty was introduced by the uncertainty in the electric field strength of plasma oscillations. This value is determined by the level of plasma turbulence, i.e., by the ratio of the oscillation energy density to the thermal energy density in plasma. In our calculations, this value was varied in a rather broad range that covered various levels of turbulence from 10^{-1} to 10^{-3}. As to the plasma oscillation frequency, its scale was also varied to achieve the best agreement with the experiment. This frequency was found to be sizably lower than the laser frequency. It is conceivable that these frequencies are scaled by the electron cyclotron frequency in a magnetic field in the presence of Weibel instability. Indeed, one can see in Fig. 1 that the separation between the satellite lines is $\Delta\lambda = 10^{-2}$ Å or, on the energy (frequency) scale, $\hbar\omega_c = 0.55$ eV. This corresponds to the cyclotron frequency (separation between the Landau levels) $\omega_c = 1.76 \times 10^7 B$, where B is expressed in Gauss. From the latter relationship, one finds the magnetic field $B = 4.76 \times 10^7$ G. The magnetic field strength can be related to the laser intensity. Indeed, by equating the magnetic energy density $W = B^2/8\pi$ in laser plasma to the laser energy density J/c, one obtains $B \approx 10^{-1}\sqrt{J}$, where B is expressed in G and J is in W/cm^2.

Strictly speaking, the relationship between the magnetic field and laser intensity should include the coefficient k of radiation transformation into magnetic field ($B = k \times 10^{-1}\sqrt{J}$). This coefficient varies from 0 to 1 and depends on the laser parameters, target material, geometry of the experiment, and other factors. The fact that, under the optimal experimental conditions, k is close to unity is confirmed by the results of a number of works. It was pointed out in [7] that the magnetic energy in the focal region is comparable with the pulse energy. As shown in [8], the quasi-stationary field in laser plasma has the same order of magnitude as the magnetic field of high-frequency laser radiation. Numerical simulation of the action of a ~100-fs laser pulse with an intensity of 10^{19} W/cm^2 on a solid target yielded magnetic field strengths of ≈250 MG [9]. Magnetic fields of ~300 MG at an intensity of ~10^{19} W/cm^2 were experimentally measured in [10]. These results are very close to our estimate with $k \approx 1$. For a laser intensity of 2×10^{17} W/cm^2, this gives $B \approx 4.5 \times 10^7$ G, which agrees well with the above estimate from the data of spectroscopic measurements.

Note that the most appropriate modeling of the experiment (see below) was made with a rather low ion temperature of ~100 eV. This is likely due to the fact that the turbulent oscillations arise at the early stages of plasma expansion when the ion effective temperature is low, while the plasma oscillations are already rather intense because of the instability development. Therefore, the observed (time-integrated) ion emission spectrum is the sum of a turbulent spectrum with low ion temperature at short times and a broad Doppler spectrum due to the ions heated at longer times. Inasmuch as the ion density sharply decreases upon plasma expansion, the contribution from the initial dense plasma-expansion stage is rather large.

4. Analysis of the experimental data presented in Fig. 1 suggests that the Stark effect in electric fields produced by plasma charged particles (electron concentration N_e is higher than or on the order of 10^{20} cm^{-3}) and the Doppler effect (plasma temperature T is higher than or on the order of 100 eV) play the significant role in the formation of Ly_α-line profiles. However, these factors alone cannot account for the appearance of a sharp peak in the experimental Ly_α profiles. The Stark effect in the oscillating electric field $\mathbf{E}(t) = \mathbf{E}_0\cos\omega t$ is the most universal mechanism for the appearance of additional features (sharp peaks and/or dips) in the smooth plasma line profiles (see, e.g., reviews [11, 12]). Due to the interaction of an ion with the field $\mathbf{E}(t) = \mathbf{E}_0\cos\omega t$, sharp peaks (satellites) appear in the emission spectra, with a distance between them equal to a multiple of ω. If this field acts on the emitting plasma ion simultaneously with a quasi-static electric field $\mathbf{F}$ ($\mathbf{F}$ may represent the plasma ion microfields and/or low-frequency plasma turbulence fields), more complicated structures (not only peaks but also dips) can arise in the line profile. The particular shape of these structures depends on the parameters of electric fields $\mathbf{F}$ and $\mathbf{E}(t) = \mathbf{E}_0\cos\omega t$ (characteristic field strength and frequency ω), on the order of atomic energy levels, and on the dipole transition matrix elements between the atomic levels.

The $n = 2$ level of a hydrogen-like ion consists of three sublevels $2P_{3/2}$, $2S_{1/2}$, and $2P_{1/2}$. In the absence of electric field, the Ly_α line arises from two radiative transitions $2P_{3/2} \longrightarrow 1S_{1/2}$ and $2P_{1/2} \longrightarrow 1S_{1/2}$. The FIX $2P_{3/2} \longrightarrow 1S_{1/2}$ and $2P_{1/2} \longrightarrow 1S_{1/2}$ spectral components are separated by approximately $\delta\lambda = 5.4 \times 10^{-4}$ nm. Note that the fine-structure splitting (i.e., the separation between the $2P_{3/2}$ and $2P_{1/2}$ levels) in the FIX ion is, on the frequency scale, $\delta\omega = 4.54 \times 10^{14}$ s^{-1}. The value of $\delta\lambda$ is much smaller than the experimentally measured Ly_α linewidth $\Delta\lambda_{1/2}$ (Fig. 1). The $2P_{3/2}$, $2S_{1/2}$, and $2P_{1/2}$ states undergo Stark mixing under the action of plasma electric field. In conjunction with the Doppler effect, this results in the rearrangement of the Ly_α profile; the individual $2P_{3/2} \longrightarrow 1S_{1/2}$ and $2P_{1/2} \longrightarrow 1S_{1/2}$ components disappear, and a single broad line is observed instead.

Numerical calculations show that the appearance of a sharp peak in the experimental FIX Ly_α profiles can be explained by the simultaneous action of two electric fields: quasi-static electric microfield $\mathbf{F}$ produced by the plasma ions and the oscillating field $\mathbf{E}(t) = \mathbf{E}_0\cos\omega t$. The program for the numerical calculation of the Ly_α profiles included, first, the determination of quasienergies and corresponding wave functions of quasienergy states (QESs) for a three-level ($2P_{3/2}$, $2S_{1/2}$, $2P_{1/2}$) system in an electric field $\varepsilon(t) = \mathbf{F} + \mathbf{E}_0\cos\omega t$. Note that the quasienergies and QESs of various quantum-mechanical systems whose Hamiltonians depend periodically on time are considered in detail, e.g., in [13]. After the quasienergies and the corresponding QESs had been found, the Ly_α emission spectrum was calculated (for a fixed ion-field strength $\mathbf{F}$), whereupon this spectrum was averaged over the $\mathbf{F}$ distribution in plasma. The Holtsmark function (see, e.g., [14]) was used as the $\mathbf{F}$ microfield distribution function. In doing so, it was assumed that the perturbation was mainly introduced by the FIX ions. To simplify the calculations, a scalar "one- dimensional" model with mutually parallel $\mathbf{F}$ and $\mathbf{E}_0$ vectors was used. Note that, along with the Stark effect in the field $\varepsilon(t) = \mathbf{F} + \mathbf{E}_0\cos\omega t$, the Doppler effect was also taken into account.

The FIX Ly_α profiles calculated for three values of plasma density $N_e = 10^{20}$, 10^{21}, and 2×10^{21} cm^{-3} are shown in Fig. 2. The calculations were carried out for plasma temperature $T = 100$ eV. For all profiles shown in Fig. 2, the amplitude of oscillating electric field was taken to be $E_0 = 3 \times 10^8$ V/cm, and the frequency ω was equal to 6×10^{14} s^{-1} in Fig. 2a, 7×10^{14} s^{-1} in Fig. 2b, and 8×10^{14} s^{-1} in Fig. 2c. Some of the theoretical profiles in Fig. 2 agree well with the observed Ly_α profiles shown in Fig. 1. Noteworthy is profile *2* in Fig. 2b, which reproduces the characteristic features of the experimental profiles shown in Fig. 1. In particular, profile *2* shows a sharp peak (marked by letter B) that corresponds to peak A in the experimental profiles. The characteristic ion microfield strength is related to the plasma density by the relationship (in CGS units) $F_H = 2.6eZ^{1/3}N_e^{2/3}$, where Z is the ion charge (in our case, $Z = 8$). The dipole interaction of the FIX ion (on the $n = 2$ level) with the oscillating field $E_0\cos\omega t$ and ion microfield F can be estimated by $G_E = (d_{12}^2 + d_{13}^2)^{1/2}E_0$ and $G_F = (d_{12}^2 + d_{13}^2)^{1/2}F_H$, respectively. Here, d_{12} and d_{13} are the dipole-moment matrix elements $d_{12} \equiv |\langle 2S_{1/2}^{(m)}|\mathbf{d}|2P_{3/2}^{(m)}\rangle|$ and $d_{13} \equiv |\langle 2S_{1/2}^{(m)}|\mathbf{d}|2P_{1/2}^{(m)}\rangle|$ calculated for the magnetic quantum number $m = 1/2$. If the plasma density N_e achieves 10^{21} cm^{-3}, G_F becomes of the same order of magnitude as G_E (for $E_0 = 3 \times 10^8$ V/cm). At the same time, G_F and G_E become of the same order as the separation $\hbar\delta\omega$ between the $2P_{3/2}$ and $2P_{1/2}$ levels. Note that the frequencies ω, for which the Ly_α profiles were calculated, were also of the same order as the separation $\delta\omega$ between the $2P_{3/2}$ and $2P_{1/2}$ levels. Thus, one can conclude that the appearance of a sharp peak in the FIX Ly_α profile can be explained theoretically if the ion dipole interaction with the ion microfield F and oscillating field $E(t) = E_0\cos\omega t$, as well as the frequency ω are of the same order of magnitude as the fine-structure splitting of the $n = 2$ level.

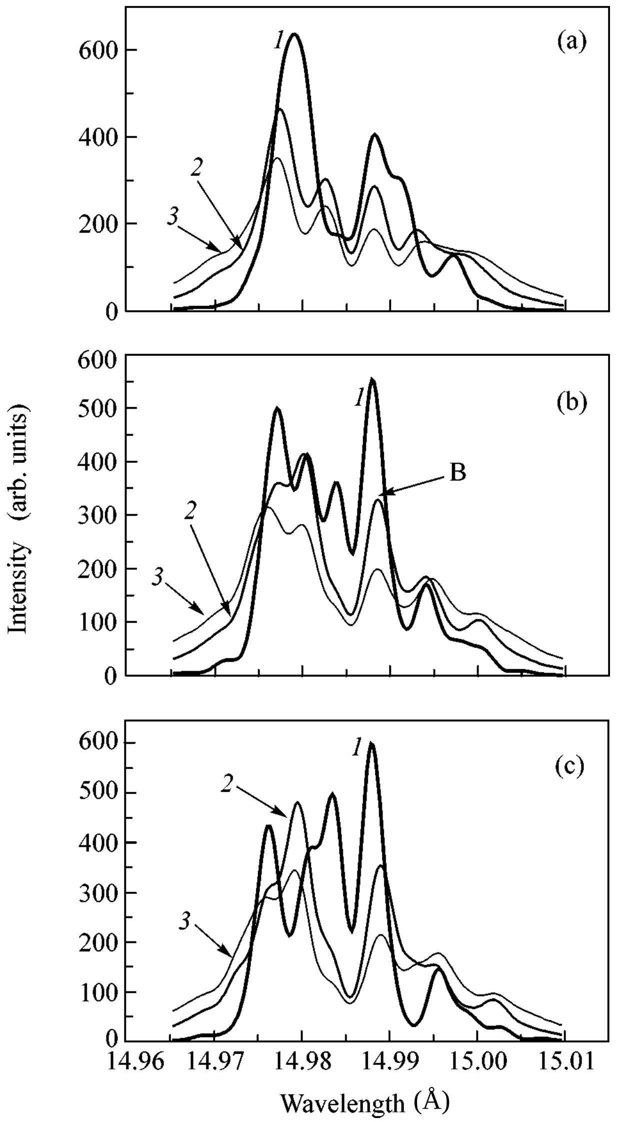

Fig. 2. The FIX Ly_α profiles calculated for plasma temperature $T = 100$ eV and for three values $N_e = (1)\ 10^{20}$, (2) 10^{21}, and (3) 2×10^{21} cm^{-3}. The amplitude of oscillating electric field is $E_0 = 3 \times 10^8$ V/cm, and the frequency ω is (a) 6×10^{14}, (b) 7×10^{14}, and (c) 8×10^{14} s^{-1}.

5. Our measurements give evidence for the presence of intense plasma oscillations in picosecond laser plasma, presumably, at the initial plasma expansion stage. The fact that the separation between the observed satellites correlates well with the estimates of magnetic field in plasma allows their assignment to plasma oscillations of the Bernstein-mode type. If this correlation will be confirmed in further experiments, it will open up new possibilities for a direct measurement of magnetic fields generated in laser plasmas.

In actuality, the observed spectrum is more complicated than the calculated one. Namely, additional satellites, likely, caused by the fine-structure sublevel crossing in a strong magnetic field appear in the spectrum (for detail, see [15]). In the vicinity of level-crossing points, the plasma-oscillation field gives rise to the well-known Blokhintsev satellite structure with the equidistant components of intensities determined by the ratio between the field intensity and frequency. It is conceivable that the observed spectrum is the superposition of the spectra of these types. Unfortunately, the magnetic-field distribution appearing upon the development of Weibel instability is unknown. Of interest are further experiments on the observation of the satellites in the spectra of multicharged ions, with the object of determining the type of magnetic field distribution and, therefore, the specific features of Weibel instability development.

This work was supported by the International Scientific and Technical Center (project no. 2155) and INTAS (grant no. 01- 0233).

REFERENCES

1. M. Tatarakis, A. Goral, I. Watts, *et al.*, Phys. Plasmas **9**, 2244 (2002).
2. V. S. Belyaev, V. I. Vinogradov, A. S. Kurilov, *et al.*, Kvantovaya Élektron. (Moscow) **30**, 229 (2000).
3. T. A. Pikuz, A. Ya. Faenov, S. A. Pikuz, *et al.*, J. X-Ray Sci. Technol. **5**, 323 (1995).
4. S. A. Pikuz, A. Maksimchuk, D. Umstadter, *et al.*, Pis'ma Zh. Éksp. Teor. Fiz. **66**, 454 (1997) [JETP Lett. **66**, 480 (1997)].
5. A. L. Osterheld, B. K. F. Young, J. Dunn, *et al.*, J. Quant. Spectrosc. Radiat. Transf. **58**, 827 (1997).
6. I. Yu. Skobelev, A. Ya. Faenov, A. I. Magunov, *et al.*, Phys. Scr. T **73**, 104 (1997).
7. Y. Sakagami, Phys. Rev. Lett. **49**, 245 (1979).
8. R. N. Sudan, Phys. Rev. Lett. **70**, 3075 (1993).
9. S. C. Wilks, W. L. Kruer, M. Tabak, and A. B. Langdon, Phys. Rev. Lett. **69**, 1383 (1992).
10. M. Tatarakis, I. Watts, K. Krushelnick, *et al.*, in *Proceedings of 28th EPS Conference on Controlled Fusion and Plasma Physics, Madeira, Portugal, 2001*, Ed. by C. Silva (Madeira Tecnopolo, Furchal, Portugal, 2001).
11. L. A. Bureeva, V. P. Gavrilenko, and V. S. Lisitsa, in *An Encyclopedia of Low-Temperature Plasma*, Ed. by V. E. Fortov (Nauka, Moscow, 2000), Vol. 1, pp. 351–366.
12. V. P. Gavrilenko, V. N. Ochkin, and S. N. Tskhai, Proc. SPIE **4460**, 207 (2002).
13. N. B. Delone and V. P. Kraĭnov, *Atom in a Strong Light Field*, 2nd ed. (Énergoatomizdat, Moscow, 1984; Springer, Berlin, 1985).
14. H. R. Griem, *Spectral Line Broadening by Plasmas* (Academic, New York, 1974; Mir, Moscow, 1978).
15. L. A. Bureeva and V. S. Lisitsa, *Perturbed Atom* (IzdAt, Moscow, 2000).

Translated by V. Sakun

JETP Letters, Vol. 78, No. 11, 2003, pp. 707–708. Translated from Pis'ma v Zhurnal Éksperimental'noĭ i Teoreticheskoĭ Fiziki, Vol. 78, No. 11, 2003, pp. 1221–1222.
Original Russian Text Copyright © 2003 by Tereshchenko, Khudukon, Romanova, Galakhov, Mel'nichenko, Sukhorukov.

Radiotomographic Observations of the Ionosphere Electron Density at the Spitsbergen Archipelago–Kola Peninsula–Karelia Meridian

E. D. Tereshchenko, B. Z. Khudukon, N. Yu. Romanova, A. A. Galakhov, Yu. A. Mel'nichenko, and V. M. Sukhorukov

Polar Geophysical Institute, Kola Research Center, Russian Academy of Sciences, Murmansk, 183010 Russia

Received October 22, 2003

The first results on the reconstruction of two-dimensional ionosphere electron density by the method of satellite tomography in the area extended for about 1700 km from the subauroral ionosphere (Karelia) to the near-polar cap zone (northwest of the Spitsbergen Archipelago) are analyzed. This experiment is unique in that the satellite-receiving apparatus was placed on a research ship in the Barents Sea, which separates the Kola Peninsula and the Spitsbergen Archipelago. The results obtained are evidence of a complex ionospheric structure in this region even under the quiet geophysical conditions of sunlight irradiation. *© 2003 MAIK "Nauka/Interperiodica".*

PACS numbers: 94.20.Dd

Global changes in electron density in the area extended from polar cap to mid-latitude ionosphere are of great importance in the study of the interaction between sun plasma and the Earth's magnetosphere and in the understanding of the physical mechanisms underlying the ionosphere formation. However, radiotomographic measurements of electron density [1] in this area are hampered because of the difficulties associated with placing diagnostic tools in the Barents Sea, which separates the Spitsbergen Archipelago and the Kola Peninsula by almost 1000 km. For this reason, an attempt was undertaken to place satellite-signal receiver on the research ship "Dal'nie Zelentsy," whose route passed between Murmansk and the Spitsbergen Archipelago (Fig. 1).

This work reports the first results on the reconstruction of the two-dimensional electron density by the radiotomographic method with satellite-signal receivers placed in the area extended from Karelia (Kem) to the northwest part of the Spitsbergen Archipelago (the Ny Alesund port). The scheme of the experiment was chosen as follows. Six receivers were placed along the satellite trajectory from the town of Kem to the port of Ny Alesund at the Spitsbergen Archipelago. The coordinates of the receiving stations were the following: Ny Alesund (78.92° N, 11.93° E), Barentsburg (78.1° N, 14.21° E), ship (74.5° N, 21.28° E at 03:57 UT, 10.10.2003, and 74.5° N, 20.21° E at 05:41 UT), Nikel (69.4° N, 31.01° E), Verkhnetulomsky port (68.6° N, 31.76° E), and Kem (64.95° N, 34.5° E). In the experiment, Russian navigation satellites orbiting at an altitude of about 1000 km with an inclination of 83° and radiating coherent signals at 150 and 400 MHz were used. One can see in Fig. 1 that the coordinates of the receiving stations closely coincide with the projection of the satellite trajectory when it moves from the north. The ship was located approximately in the middle of the large distance between the continent and the Spitsbergen Archipelago and, thus, its receiver could form a system of crossing beams in the ionosphere and reconstruct the electron density distribution over a wide spatial area extended from the subauroral zone to the polar cap. Taking into account that there are two zones where currents enter the ionosphere and where one can expect

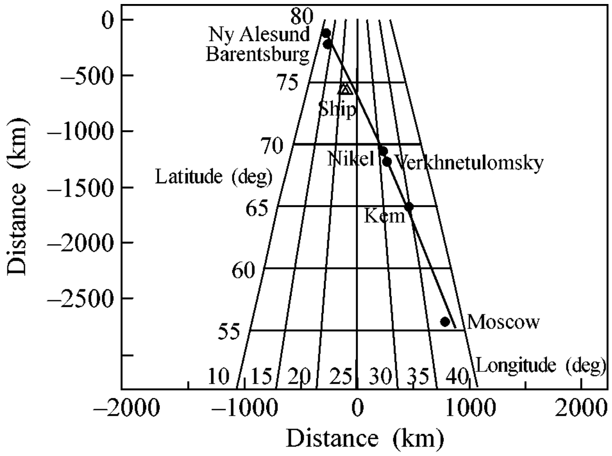

Fig. 1. Projection of the satellite upon its moving from the north (solid line); locations of receiving stations (dots); and location of the research ship "Dal'nie Zelentsy" for the sessions at 03:57 and 05:41 UT on August 10, 2003.

0021-3640/03/7811-0707$24.00 © 2003 MAIK "Nauka/Interperiodica"

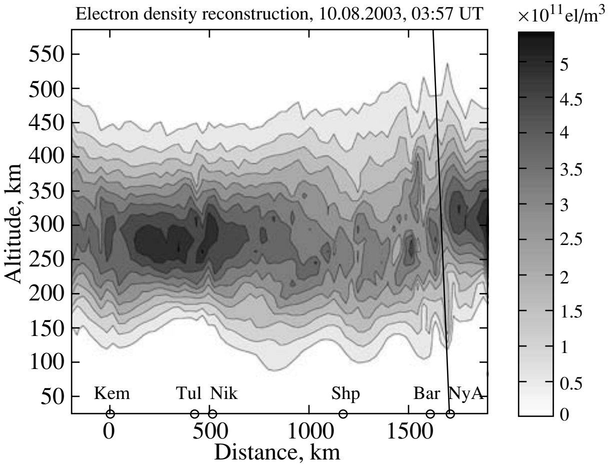

Fig. 2. Electron-density reconstruction for the satellite session at 03:57 UT on August 10, 2003. The ship's latitude and the satellite direction azimuth are, respectively, 84° and 66°.

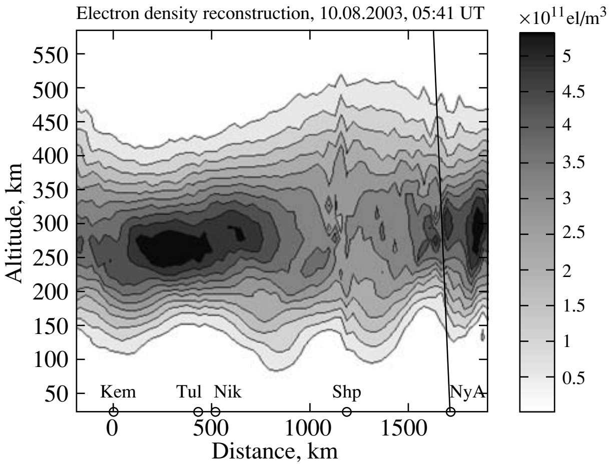

Fig. 3. Electron-density reconstruction for the satellite session at 05:41 UT on August 10, 2003. The ship's latitude and the satellite direction azimuth are, respectively, 78° and 61°.

the appearance of vertical electron-density structures, the receivers in the vicinity of the polar cap at the Spitsbergen Archipelago (Barentsburg, Ny Alesund) and in the auroral zone at the Kola Peninsula (Verkhnetulomsky port, Nikel) were placed at a comparatively small distance from each other.

The results of the tomographic electron-density reconstruction for practically the same ionospheric region in two sequential observation sessions carried out at 03:57 and 05:41 UT on August 10, 2003, are presented in Figs. 2 and 3. At 03:57 UT, the satellite signals were recorded by all six receiving stations, while, at 05:41 UT, the satellite signals were not recorded at Barentsburg. The distance from Earth, measured from Kem, is plotted on the X axis. The receiving stations are denoted by NyA, Bar, Shp, Nik, Tul, and Kem. The size of the elementary cell of the tomographic reconstruction mesh was (distance × altitude) 30 × 16 km. The solid slanting lines show the direction (making an angle of approximately 8° to the south of the vertical) of magnetic field lines over the Spitsbergen Archipelago.

One can see from the comparison of Figs. 2 and 3 that the electron-density distribution at two different instants of time is similar on the whole. In both cases, there is a region with the reduced electron density to the north of the Kola Peninsula and the isolated local structures (extended approximately along the geomagnetic field and better seen in Fig. 2) with higher concentration are present near the polar cap over the Spitsbergen Archipelago in the lower and upper parts of the ionospheric F region. As the Sun's zenith angle increases (when going from Fig. 2 to Fig. 3), the concentration increases and the ionosphere becomes more homogeneous.

REFERENCES

1. V. Kunitsyn and E. Tereshchenko, *Ionospheric Tomography* (Springer, Berlin, 2003).

Translated by V. Sakun

JETP Letters, Vol. 78, No. 11, 2003, pp. 709–713. Translated from Pis'ma v Zhurnal Éksperimental'noĭ i Teoreticheskoĭ Fiziki, Vol. 78, No. 11, 2003, pp. 1223–1227.

The Townsend Coefficient and Runaway of Electrons in Electronegative Gas

A. M. Boichenko, A. N. Tkachev, and S. I. Yakovlenko*
Institute of General Physics, Russian Academy of Sciences, Moscow, 119991 Russia
**e-mail: syakov@kapella.gpi.ru*

Received October 3, 2003; in final form, October 23, 2003

We have studied the character of variation of the number of electrons formed in an electronegative gas (SF_6) under the action of an external electric field. At any value of the electric field strength E, the number of generated electrons exponentially increases with the distance from the cathode, while the average velocity and energy of electrons attain constant values. At small values of the reduced field strength, $E/p < 94$ V/(cm Torr) (p is the gas pressure), the regime of electron attachment prevails that is characterized by negative values of the exponent (negative Townsend coefficients). For $E/p > 94$ V/(cm Torr), the electron multiplication proceeds in the usual Townsend regime with positive exponents. In the intermediate region of E/p = 40–160 V/(cm Torr), the electron multiplication coefficient exhibits a linear dependence on E/p. Numerical calculations based on a simple model show that the Townsend multiplication regime takes place even in very strong fields where the drag caused by ionization can be ignored. A universal function describing the electron runaway in SF_6 is obtained. © *2003 MAIK "Nauka/Interperiodica".*

PACS numbers: 52.80.Dy; 52.25.Jm

INTRODUCTION

The Townsend regime of gas ionization under the action of an external electric field has two characteristic features. First, the number of ionization events exponentially increases with the distance to the point of the first electron production. Second, the average velocity and energy of electrons are independent of this distance. By modeling this process using methods of many-particle dynamics, it is possible to determine the dependence of the Townsend multiplication factor on the electric field strength E and the gas pressure p, provided that the cross sections of the elastic and inelastic collisions of electrons with atoms and molecules of the neutral gas are known.

Recently, we performed such modeling [1, 2] and established that, for a sufficiently large interelectrode distance, the Townsend ionization regime can take place even in very strong fields where, according to conventional notions, the average electron energy is expected to grow continuously [3–5]. Under these conditions, the Townsend coefficient exhibits a nonmonotonic dependence on the reduced electric field strength E/p. This nonmonotonic behavior of the electron multiplication coefficient leads to double-branch curves (analogs of the Paschen curve) separating the regimes of intense electron multiplication and their runaway without multiplication. These new findings are especially important in the context of obtaining pulsed electron beams of nanosecond duration and record current amplitudes (up to ~70 A in air and ~200 A in helium) at atmospheric pressure [6].

Previously, we modeled the field-induced electron multiplication processes in helium [1] and xenon [2]. It would also be of interest to use the same method in analysis of the mechanism of electron multiplication in electronegative gases, which are characterized by a large cross section of the electron attachment to molecules. In view of the competition between the electron attachment and multiplication processes, it is not clear whether the concept of the Townsend coefficient is adequate in application to electronegative gases. Nevertheless, such gases are widely used in various discharges, in particular, for pumping exciplex and chemical lasers. Below, we consider the electron multiplication and runaway in SF_6, a convenient model gas for which the characteristics of electron collisions are well known.

MULTIPLICATION AND ATTACHMENT OF ELECTRONS: DESCRIPTION OF THE MODEL

The process of electron multiplication and runaway in SF_6 was modeled using a modified particle-in-cell method [7]. The transfer of electrons between two planes spaced by a distance d was driven by the applied voltage U (generating a field with the strength $E = U/d$). It was assumed that the constant voltage was applied long before the appearance of electrons under consideration. The electrons generated on the cathode possessed randomly oriented velocities and the energies distributed according to the Poisson law with an average value of $\varepsilon_0 = 0.2$ eV. The equations of motion for all electrons were solved at small time steps and the elastic and inelastic collisions were played with the probabilities

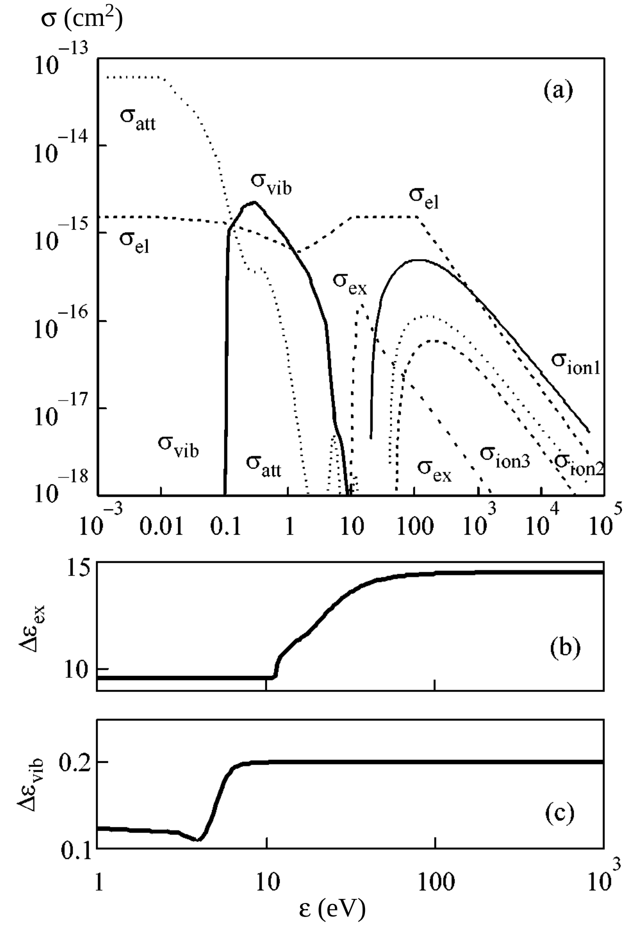

Fig. 1. Plots of (a) the cross sections of electron interactions with SF_6 molecules and the energies of excitation of the (b) electronic and (c) vibrational states versus the electron energy. Data on the cross sections for elastic collisions (σ_{el}), attachment (σ_{att}), excitation of the vibrational states (σ_{vib}), excitation of electronic state (σ_{ex}), and ionization at various thresholds (σ_{ion1}, σ_{ion2}, σ_{ion3}) are taken from [8–10].

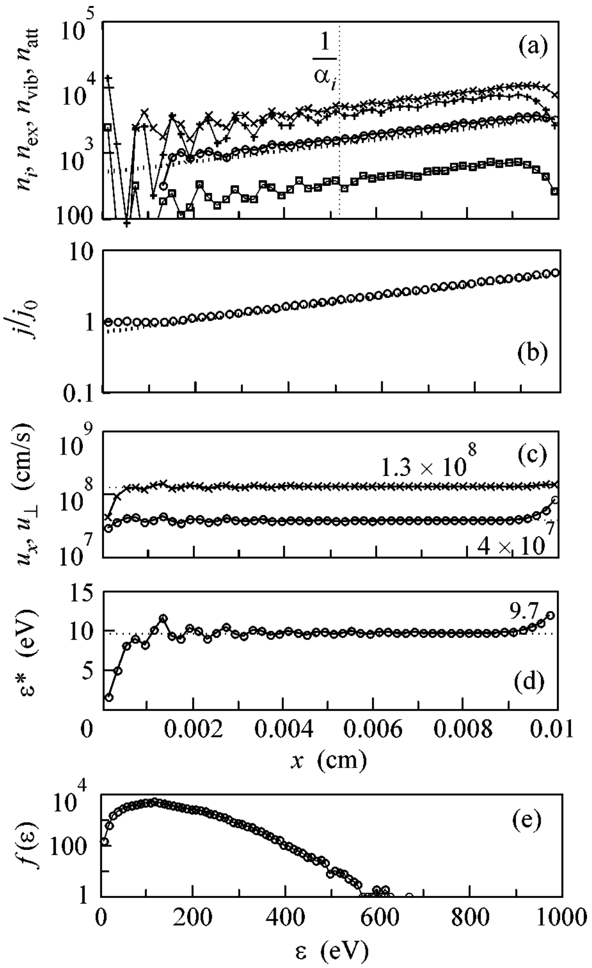

Fig. 2. Plots of the characteristics of electron multiplication in the Townsend regime versus distance to cathode x calculated for $N = 3.22 \times 10^{18}$ cm^{-3} ($p = 100$ Torr), $U = 1.6$ kV, $d = 0.1$ mm, and $E = 16$ kV/cm ($E/p = 160$ V(cm Torr)): (a) the number of generated ions n_i (○) and the events of excitation of the electronic states (×), excitation of the vibrational states (+), and electron attachment (□); dashed curve shows the plot of 500exp(192x/cm) that yields $\alpha_i = 192$ cm^{-1}, $\alpha_i d \approx 1.92$; (b) the ratio of electron flux $j(x)$ at a given point to the total electron flux j_0 from cathode; dashed curve shows the plot of 0.7exp(192x/cm); (c) the average electron velocity projection u_x onto the electric field direction (○) and the average modulus of the electron velocity projection $u_\perp$ onto the plane perpendicular to the electric field (×); (d) the average electron energy ε*; (e) the energy distribution of electrons reaching the anode.

determined by cross sections of the corresponding elementary events. Data on the cross sections and energy characteristics of these events (Fig. 1) were taken from [8–10].

THE TOWNSEND IONIZATION REGIME

The Townsend multiplication coefficient α_i was determined from the slope of a plot of the logarithm of electron current versus the distance to cathode (Fig. 2). The same value is obtained from the slope of the logarithm of the number of ionization, attachment, and excitation events. Naturally, the interelectrode distance must be greater than the characteristic electron multiplication length (equal to the reciprocal Townsend multiplication factor α_i^{-1}).

The results of our model calculations showed that, for a sufficiently large reduced field strength ($E/p >$ 94 V/(cm Torr)) and sufficiently large interelectrode distance ($d > \alpha_i^{-1}$), the anticipated Townsend ionization regime actually takes place (Fig. 3). The main characteristics of this regime show qualitatively the same behavior as that observed for helium and xenon. As the distance x to cathode increases, the number of electron generation events and the number of inelastic collisions exponentially increase. At the same time, the average

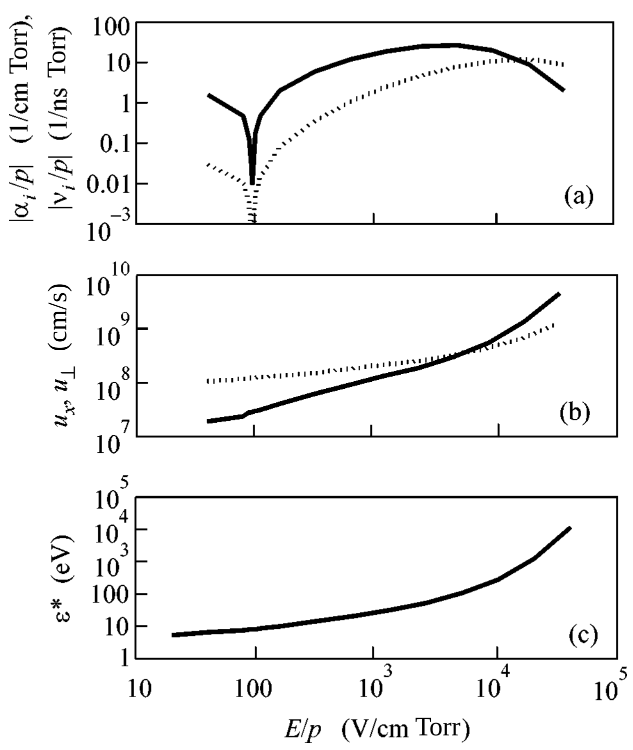

Fig. 3. Plots of the ionization and drift characteristics versus the reduced field strength E/p (p = 100 Torr): (a) the modulus of the Townsend coefficient α_i/p (solid curve) and the ionization rate ν_i/p normalized to the gas pressure p (dashed curve); (b) the average electron velocity projection u_x onto the electric field direction (solid curve) and the average modulus of the electron velocity projection $u_\perp$ onto the plane perpendicular to the electric field (dashed curve); (c) the average electron energy ε*.

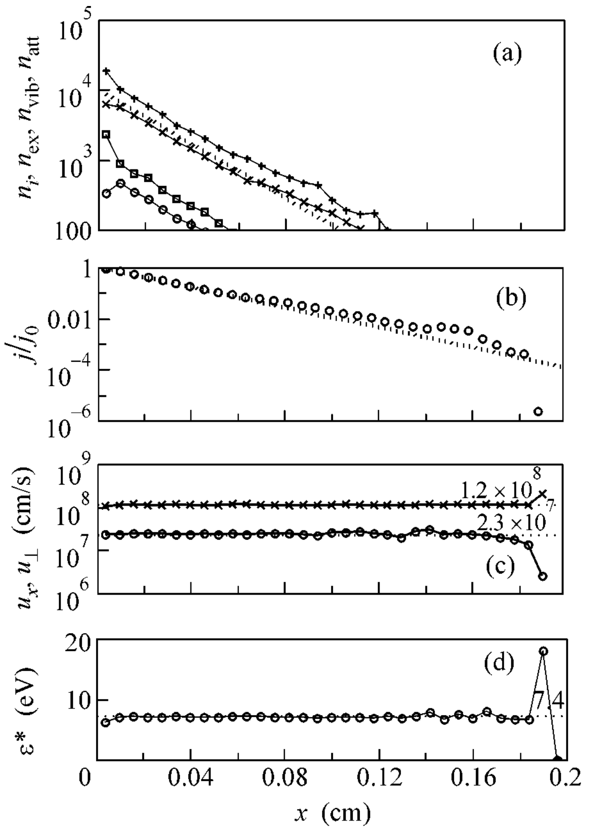

Fig. 4. Plots of the characteristics of electron multiplication in the electron attachment regime versus distance to cathode x calculated for E/p = 80 V/(cm Torr), p = 100 Torr, U = 2.4 kV, and d = 3 mm. For notations see the legend to Fig. 2.

electron energy ε*, the average projection u_x of the electron velocity onto the electric field direction, and the average projection $u_\perp$ of the electron velocity onto the plane perpendicular to the field attain constant values independent of the distance x. A maximum in the energy distribution of electrons reaching the anode is observed at small energies $\varepsilon^* \ll eU$.

The Townsend multiplication coefficient α_i is proportional to the gas density (pressure p) and can be written as $\alpha_i(E, p) = p\xi(E/p)$, where the function $\xi(E/p)$ is characteristic of a given gas. The results of calculations showed that this function exhibits a maximum at $(E/p)_{\max} \approx 5$ kV/(cm Torr), which is related to the presence of a maximum in the ionization cross section.

COMPETITION BETWEEN THE ATTACHMENT AND MULTIPLICATION OF ELECTRONS

An important feature of electronegative gases is that, when the electric field strength is below a certain value ($E/p < 94$ V/(cm Torr) for SF_6), electrons emitted from the cathode predominantly attach to molecules rather than participate in the multiplication process. The regime of electron attachment is, in a certain sense, inverse to the multiplication process (Fig. 4). Indeed, the former regime is also characterized by exponential variation of both the electron current and the number of inelastic collisions, while the average electron energy ε* and the average projections u_x and $u_\perp$ of the electron velocity are independent of the interelectrode distance x. However, the multiplication coefficient in this case becomes negative.

It should be noted that the attachment predominates mostly because of a drop in the ionization cross section at small electron energies rather than due to a large cross section for the electron sticking to a molecule. The attachment prevails over multiplication in the region of reduced field strengths $E/p < 94$ V/(cm Torr), where the average electron energy ε* drops significantly (ε* < 10 eV) below the first ionization threshold (20 eV for SF_6). Another noteworthy fact is the linear dependence of the multiplication coefficient on the reduced field strength in the region of sign change (Fig. 5).

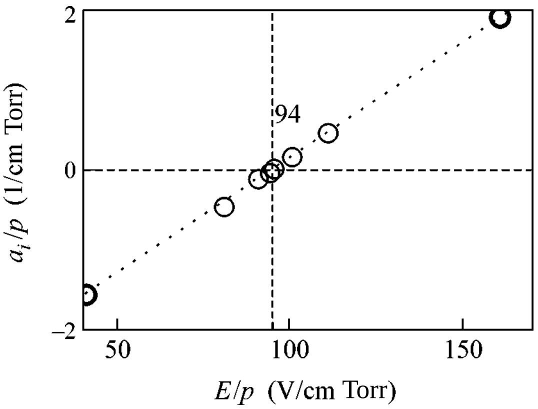

Fig. 5. A plot of the reduced multiplication coefficient versus reduced field strength in the intermediate region. Dashed line shows the plot of 2.87×10^{-2} E/p (cm Torr/V) – 2.7.

ELECTRON MULTIPLICATION AND THE LOCAL CRITERION OF ELECTRON RUNAWAY

The runaway of electrons is usually characterized in terms of the local criterion (for more detail, see, e.g., [3, p. 53], [4, p. 71], and [5, p. 74]). It is commonly accepted that the flux of electrons from cathode to anode in the established regime is close to monoenergetic [5]. The energy ε of electrons in the electric field E is described by the balance equation [3–5],

$$d\varepsilon/dx = eE - F(\varepsilon), \tag{1}$$

where $F(\varepsilon)$ is the friction (drag) force related to the collisions of electrons with gas particles.

The drag force as a function of the electron energy has the maximum $F_{\max} = F(\varepsilon_{\max})$. According to the conventional approach, a necessary condition for obtaining runaway electrons in a gas is as sufficiently large field strength $E > E_{cr1}$, where the critical field strength E_{cr1} is determined by the maximum drag force: $E_{cr1} = F_{\max}/e$.

However, simple considerations show that the regime of continuous acceleration for the major fraction of electrons in a gas is not achieved even for $E \gg E_{cr1}$ when the distance to cathode is sufficiently large.

Average electron energy limited by multiplication. Note the following important fact. Even for $E > E_{cr1}$, the average electron energy does not infinitely grow with the distance x because the above considerations do not take into account the effect of electron multiplication. For determining the average energy ε*, we should rewrite the energy balance equation (1) so as to take into account variation of the number of electrons,

$$d(N_e\varepsilon^*)/dx = eEN_e - F(\varepsilon^*)N_e, \tag{2}$$

where $N_e(x)$ is the electron density at the distance x. Taking into account that $dN_e/dx = \alpha_i N_e$, we obtain

$$d\varepsilon^*/dx = eE - F(\varepsilon^*) - \alpha_i\varepsilon^*. \tag{3}$$

This equation differs from Eq. (1) by the negative term $\alpha_i\varepsilon^*$ describing “redistribution” of the energy gained by electrons accelerated in the field between all electrons, including the newly generated ones.

Thus, even with full neglect of the electron drag in the gas ($F(\varepsilon) = 0$), the average electron energy is limited: $\varepsilon^* < \varepsilon^*_{\max} = eE/\alpha_i$. Therefore, Eq. (1) cannot be used for determining the average electron energy and the electron energy distribution cannot be considered as monoenergetic. Nor should we accept the notion that the Townsend regime is impossible for $E > E_{cr1}$. In fact, the value of E_{cr1} determines the condition for a drop in the Townsend multiplication coefficient for $E > E_{\max} \approx E_{cr1}$, rather than the condition for continuous acceleration of the major fraction of electrons with increasing distance x.

A nonlocal criterion of electron runaway. The Townsend ionization regime is established at a certain distance from the cathode, $x \sim \alpha_i^{-1}$, which corresponds to the characteristic multiplication length. When the interelectrode distance is small, $d < \alpha_i^{-1}$, the pattern of electron multiplication substantially differs from that in the Townsend regime. In this case, a considerable number of electrons are continuously accelerated so that both the velocity projection u_x onto the x axis and the average energy ε* increase with the distance x. The peak in the energy distribution of electrons reaching the anode coincides with the maximum energy $eU = eEd$ acquired by an electron upon the flight from cathode to anode.

In contrast to the commonly accepted notions [3–5], the approach developed in [1, 2] assumes that runaway electrons begin to predominate when the interelectrode distance becomes comparable with the characteristic electron multiplication length α_i^{-1}. For $\alpha_i d < 1$, the runaway electrons also predominate in the spectrum of electrons reaching the anode. Accordingly, the criterion determining the critical field strength E_{cr} is as follows:

$$\alpha_i(E_{cr}, p)d = 1. \tag{4}$$

For flat electrodes ($E_{cr} = U_{cr}/d$), we obtain

$$pd\xi(E_{cr}/p) = 1 \quad \text{or} \quad pd\xi(U_{cr}/pd) = 1. \tag{5}$$

The latter formula in Eq. (5) determines the implicit dependence of the critical voltage $U_{cr}(pd)$ on the product pd of the interelectrode distance by the gas pressure (Fig. 6). This runaway curve separates the region of effective multiplication from a regime in which electrons fly through the discharge gap without participating in multiplication events. This curve, universal for a given gas, contains the lower and upper branches

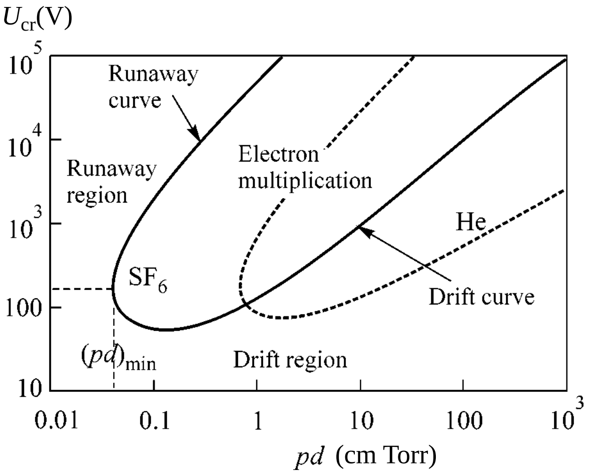

Fig. 6. The runaway curves $U_{cr}(pd)$ separating the region of effective multiplication from the regime of electron runaway without multiplication. Solid curve refers to SF_6; dashed curve shows the data for He taken from [1].

(Fig. 6). The boundary point between the two branches corresponds to the minimum product $pd = (pd)_{min}$ and to a maximum of the function $\xi(x)$.

CONCLUSIONS

We have studied the character of variation of the number of electrons formed in an electronegative gas (SF_6) under the action of an external electric field. At any value of the electric field strength E, the number of generated electrons exponentially increases with the distance from the cathode, while the average velocity and energy of electrons attain constant values. At small values of the reduced field strength, $E/p < 94$ V/(cm Torr), the regime of electron attachment that is characterized by negative values of the exponent (negative Townsend coefficients) predominates. For $E/p > 94$ V/(cm Torr), the electron multiplication proceeds in the usual Townsend regime with positive exponents. In the intermediate region of $E/p = 40$–160 V/(cm Torr), the electron multiplication coefficient exhibits a linear dependence on E/p. Tabulated values of the Townsend coefficient, ionization rate, and electron drift velocities can be used for constructing the diffusion–drift models describing the properties of discharges in various gases.

Numerical calculations based on a simple model show that the Townsend multiplication regime takes place even in very strong fields where the drag caused by ionization can be ignored. A universal function describing the electron runaway in SF_6 is obtained.

ACKNOWLEDGMENTS

The authors are grateful to V.F. Tarasenko for stimulating discussions.

This study was supported by the International Science and Technology Center, grant no. 1270.

REFERENCES

1. A. N. Tkachev and S. I. Yakovlenko, Pis’ma Zh. Éksp. Teor. Fiz. **77**, 264 (2003) [JETP Lett. **77**, 221 (2003)].
2. A. N. Tkachev and S. I. Yakovlenko, Pis’ma Zh. Tekh. Fiz. **29** (9), 54 (2003) [Tech. Phys. Lett. **29**, 683 (2003)].
3. L. P. Babich, T. V. Loĭko, and V. A. Tsukerman, Usp. Fiz. Nauk **160**, 49 (1990) [Sov. Phys. Usp. **33**, 521 (1990)].
4. Yu. D. Korolev and G. A. Mesyats, *The Physics of Pulse Breakdown* (Nauka, Moscow, 1991).
5. Yu. P. Raĭzer, *The Physics of Gas Discharge* (Nauka, Moscow, 1992).
6. V. F. Tarasenko, S. I. Yakovlenko, V. M. Orlovskiĭ, *et al.*, Pis’ma Zh. Éksp. Teor. Fiz. **77**, 737 (2003) [JETP Lett. **77**, 611 (2003)].
7. A. N. Tkachev and S. I. Yakovlenko, Laser Phys. **12**, 1022 (2002).
8. T. Stanski and B. Adamchyk, J. Mass Spectrom. Ion Phys. **46**, 31 (1983).
9. J. P. Novak and M. F. Frechette, J. Appl. Phys. **55**, 107 (1984).
10. L. E. Kline, D. K. Davies, C. L. Chen, and P. J. Chantry, J. Appl. Phys. **50**, 6789 (1979).

Translated by P. Pozdeev

JETP Letters, Vol. 78, No. 11, 2003, pp. 714–717. Translated from Pis'ma v Zhurnal Éksperimental'noĭ i Teoreticheskoĭ Fiziki, Vol. 78, No. 11, 2003, pp. 1228–1231.
Original Russian Text Copyright © 2003 by Tarasov, Kuz'min, Fominskii, Agulo, Kalabukhov.

Electron Cooling in a Normal-Metal Hot-Electron Bolometer

M. A. Tarasov[1, 3, *], L. S. Kuz'min[2, 3], M. Yu. Fominskii[1, 3], I. E. Agulo[3], and A. S. Kalabukhov[2, 3]

[1] *Institute of Radio Engineering and Electronics, Russian Academy of Sciences, Moscow, 101999 Russia*
**e-mail: tarasov@hitech.cplire.ru*
[2] *Moscow State University, Moscow, 119899 Russia*
[3] *Chalmers University of Technology, S41296 Gothenburg, Sweden*

Received September 17, 2003; in final form, October 9, 2003

Normal-metal hot-electron bolometers, each of which contains two superconductor–insulator–normal metal (SIN) junctions for electron cooling and two SIN junctions for temperature measurements, were fabricated and experimentally studied. The electron cooling by SIN junctions is an analog of the Peltier effect and allows one to reduce the effective electron temperature of a bolometer. The electron temperature was determined from the ratio of the differential resistance to normal one for several values of a constant bias. At a phonon temperature of 250 mK, the resistance ratio at zero bias reached 1000, which was close to the theoretical value for an ideal SIN junction. A decrease in the electron temperature from 250 to 90 mK was obtained. © *2003 MAIK "Nauka/Interperiodica".*

PACS numbers: 07.57.Kp; 74.50.+r

Normal-metal hot-electron bolometers with capacitive coupling were proposed in [1] and experimentally studied in [2]. The main characteristics of a bolometer, namely, the response and the noise-equivalent power (NEP), are determined by its electron temperature. A way of improving these characteristics by using an electron cooling with the help of superconductor–insulator–normal metal (SIN) junctions was proposed in [3]. A direct electron cooling was demonstrated in [4] and further developed in [5]. Two SIN tunnel junctions can be used for both electron cooling in the normal metal and measuring the response of the bolometer to an external signal. The electron cooling is an analog of the Peltier effect known since 1834 for a pair of junctions formed by different metals: when current flows through the junctions, one of them is heated and the other is cooled. The principle of cooling by SIN junctions is similar to blowing hot vapor away from the surface of hot tea in a cup. Hot electrons with energies above the Fermi level are removed from the normal metal via one junction and cold electrons with energies below the Fermi level are supplied to the normal metal via the other junction. This is the main qualitative distinction from the Peltier effect, because both SIN junctions participate in cooling of the normal metal lying between them. Cold electrons with energies below the Fermi level can also be considered as hot holes removed via the second SIN junction. A simple estimate of the power eliminated in this way can be made by assuming that, at a bias near the energy gap, each electron participating in the current removes the energy smaller than or about k_bT. Then, the power eliminated by a current I is about Ik_bT/e. For an efficient cooling, it is necessary to have a channel for heat removal by the current of hot quasiparticles with energies above the superconducting energy gap. This is achieved with the help of the normal-metal traps. Evidently, a decrease in the electron temperature leads to an increase in the temperature response, which makes it possible to reduce the contribution of noise of the subsequent amplifier and the NEP.

Principles of temperature measurement by superconducting tunnel junctions. To estimate the electron temperature, we can use the approximation of the current–voltage (I–V) characteristic of a real junction by the I–V characteristic of an ideal SIN junction. For the latter, the following simple expression is valid:

$$I(V,T) = \frac{1}{eR_N}\sqrt{2\pi k_b T\Delta}\exp\left(-\frac{\Delta}{k_bT}\right)\sinh\left(\frac{eV}{k_bT}\right), \quad (1)$$

where R_N is the normal resistance of the junction, T is the temperature, Δ is the energy gap of the superconductor, e is the electron charge, k_b is the Boltzmann constant, and V is the voltage. The subgap leakage current due to the nonideal structure of the SIN junction can modify the I–V characteristic and considerably affect the response of the bolometer. In addition to the defects of the tunnel junction, the I–V characteristic of a highly transparent junction can also be affected by the two-electron tunneling current, when two electrons form a Cooper pair [6]. As was noted in [7], a decrease in the barrier thickness leads to an increase in the contribution of Andreev reflection. At temperatures below 200 mK, an inverse tunneling of quasiparticles from the superconductor to the normal metal is possible [8] and an inverse absorption of phonons may also occur after the recombination of quasiparticles. Without special traps for hot quasiparticles, the effect of electron cooling may be considerably suppressed. In the experiments [9], a temperature saturation was observed below 300 mK, when hot quasiparticles are in the normal-metal trap.

For real junctions, it is important to estimate the effect of point defects of the tunnel barrier. The defects determine the residual resistance at zero bias. For a typical junction with a normal resistance of 1 kΩ at 300 mK, the differential resistance in the absence of bias should be greater than 1 MΩ. If we take the leakage resistance equal to this value, i.e., 1 MΩ, the electron temperature due to the Joule heating will be expressed as

$$T_e = \left(T_{ph}^5 + \frac{P}{\Sigma \mathcal{V}}\right)^{1/5}, \qquad (2)$$

where P is the power scattered by the leakage resistance, $\Sigma = 3 \times 10^9\ \mathrm{W\ m^{-3}\ K^{-5}}$ is the characteristic constant of the normal metal, and $\mathcal{V} = 0.18\ \mu\mathrm{m}^3$ is the volume of the normal metal. For zero phonon temperature at a standard bias of 400 μV, we obtain a temperature increase of 200 mK. For a smaller bias of 100 μV, we still obtain an overheating of 115 mK. An increase in the leakage resistance to 10 MΩ reduces the overheating to 127 mK at a bias of 400 μV. This means that even a very small measuring current of the thermometer may cause a considerable increase in the electron temperature above the phonon temperature and introduce an error in the temperature measurement. Let us estimate the possibility of applying the resistance ratio criterion to temperature measurements by a real junction. For this purpose, we introduce a shunting resistance R_s of the leakage current into Eq. (1) and obtain the relative differential resistance in the form

$$r = \left[\left(\sqrt{\frac{k_bT}{2\pi\Delta}}\,\frac{\exp(\Delta/k_bT)}{\cosh(eV/k_bT)}\right)^{-1} + \frac{R_n}{R_s}\right]^{-1}. \qquad (3)$$

This kind of temperature dependence calculated for the standard parameters of one of our samples is shown in Fig. 1. One can see that, at zero bias, a saturation of the thermometer is observed as early as at 200 mK, while at relatively high biases, the thermometer retains a high sensitivity. To measure lower temperatures, it is necessary to use greater bias voltages at which the differential resistance is smaller than the leakage resistance. For choosing the bias voltage, the following simple criterion can be used: at temperatures below 200 mK, the resistance ratio should be measured at a bias voltage of 250 μV at the thermometer, and below 100 mK, at a bias of 300 μV.

Electron cooling by SIN junctions. For the cooling power, we write a simple analytical expression:

$$P_{\mathrm{cool}}(T_e, V) = \frac{\sqrt{2\pi\Delta k_bT_e}}{2eR_N}\left(\frac{\Delta}{e} - V\right)\exp\left(-\frac{\Delta - eV}{k_bT_e}\right). \qquad (4)$$

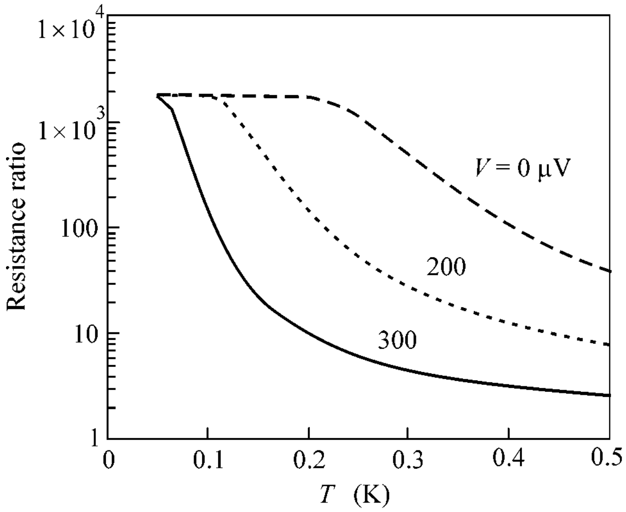

Fig. 1. Temperature dependences of the resistance ratio at zero bias and at biases of 200 and 300 μV. The dependences were calculated for a thermometer with a normal resistance of 10 kΩ and a leakage resistance of 35 MΩ.

The effective electron temperature T_e is determined from the heat balance equation

$$(T_{ph}^5 - T_e^5)\Sigma\mathcal{V} = P_{\mathrm{cool}}(T_e) - P_{bg} - V^2/R_s, \qquad (5)$$

where T_{ph} is the phonon temperature, V is the constant bias voltage, R_s is the shunting leakage resistance, $P_{bg} = 0.5hf\Delta f = 6 \times 10^{-14}$ W is the background radiation power, $\Sigma = 3 \times 10^9\ \mathrm{W\ m^{-3}\ K^{-5}}$ is the parameter of the absorber material, and $\mathcal{V} = 1.8 \times 10^{-19}\ \mathrm{m}^3$ is the volume of the absorber. A graphical solution of Eq. (5) is shown in Fig. 2, where curve P_{ep} corresponds to the electron–phonon energy transfer $P_{ep} = (T_{ph}^5 - T_e^5)\Sigma\mathcal{V}$ at a phonon temperature of 250 mK and curves P_V correspond to the cooling or overheating powers $P_V = P_{\mathrm{cool}} - V^2/R_s - P_{bg}$ in the bolometer. From these dependences it follows that, at a leakage resistance of 30 MΩ, one can obtain an electron cooling of $\Delta T = 160$ mK at a phonon temperature of 250 mK.

Such a noticeable decrease in the electron temperature should lead to a considerable improvement of the bolometer parameters and, in particular, to an increase in the temperature response dV/dT_e. If we approximate the I–V characteristic of the SIN junction by the expression [9]

$$I(V) = I_0 e^{(eV-\Delta)/k_bT_e}, \quad I_0 = \frac{\sqrt{2\pi\Delta k_bT_e}}{2eR_N},$$

the maximal temperature sensitivity should be observed at zero bias and be equal to

$$\frac{dV}{dT_e} \cong \frac{k_b}{e}\ln\frac{I}{I_0} = \frac{k_b}{e}\frac{eV - eV_\Delta}{k_bT_e} = -\frac{V_\Delta}{T_e}. \qquad (6)$$

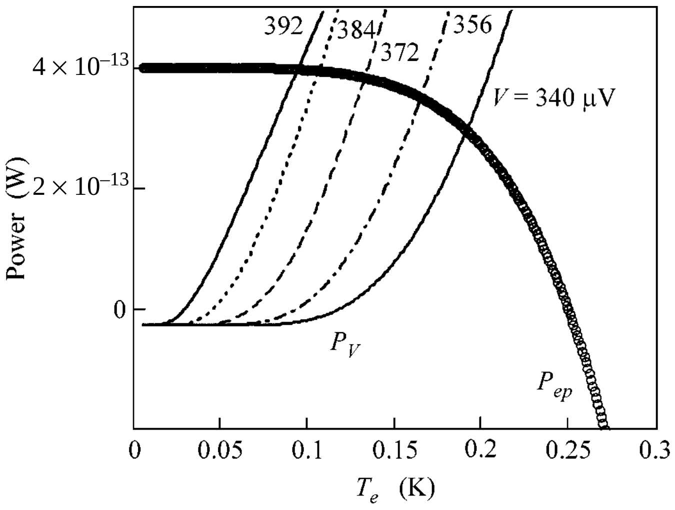

Fig. 2. Curve P_{ep} corresponds to the electron–phonon power transfer $P_{ep} = (T_{ph}^5 - T_e^5)\Sigma v$ at a phonon temperature of 250 mK; curves $P_V = P_{\text{cool}} - V^2/R_s - P_{bg}$ correspond to the cooling and heating power balance in a bolometer with the bias voltages at the cooling junctions within 392–340 μV. The intersection of curves P_{ep} and P_V yields the value of the stable electron temperature T_e in equilibrium.

Evidently, a twofold decrease in the electron temperature leads to a twofold increase in the temperature response. This allows one to reduce the contribution of noise from the subsequent amplifier and, hence, to reduce the NEP. However, in a real junction, such high response values cannot be obtained because of the parasitic leakage resistance. Now, if, for temperature measurements, one uses the same SIN junctions as those used for cooling with the bias chosen to satisfy the condition $eV - \Delta = k_bT$, the response becomes equal to

$$dV/dT_e = (T/T_e)k_b/e. \tag{7}$$

Then, the NEP proves to be considerably reduced in both cases:

$$NEP^2 = 4k_bT_e^2G. \tag{8}$$

As a result, in the example considered above, a temperature decrease from 250 mK to less than 100 mK corresponds to a decrease in the NEP by a factor of 2.5.

EXPERIMENT

For the sake of comparison with the theoretical estimates, in Fig. 3 we present the experimental dependences of the differential resistance of SIN thermometers on the bias voltage of the cooling junctions at a phonon temperature of 20 mK. One can see that the maximal resistance of 45 MΩ is observed at zero bias at the cooling junctions. Any finite bias voltage reduces the resistance below 37 MΩ, i.e., leads to an overheating above 20 mK instead of cooling. An increase in the resistance of the thermometer biased by 200–350 μV with a cooler biased by 400 μV corresponds to the expression for the resistance ratio at a finite bias, when the cooling from the bias-overheated thermometer (98 mK) to an electron temperature of 88 mK takes place. Similar dependences measured at a phonon temperature of 250 mK (Fig. 3) exhibit a growth of the resistance of the unbiased thermometer from 12 to 36 MΩ with increasing bias at the cooler. The resistance of the thermometer at this phonon temperature is not as strongly shunted by leakage, and the electron temperature can be estimated from the resistance ratio at zero bias according to Eq. (3). The resistance ratio at

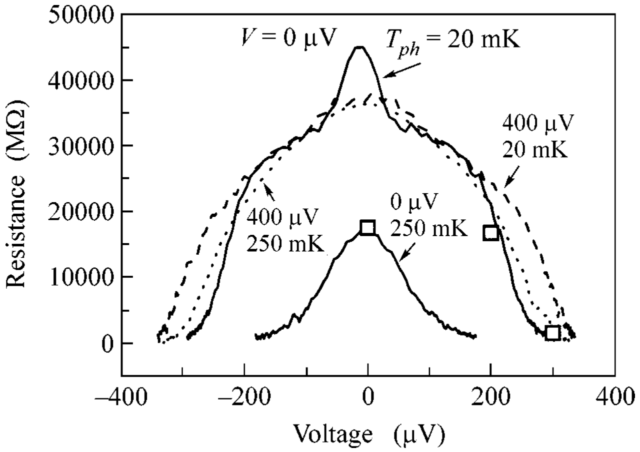

Fig. 3. Dependences of the differential resistance of an SIN thermometer on its bias voltage. The dependences were measured at phonon temperatures of 20 and 250 mK with two bias voltages at the cooler: 0 and 400 μV. Theoretical values from Fig. 1 are presented for three bias voltages at the thermometer: 0, 200, and 300 μV.

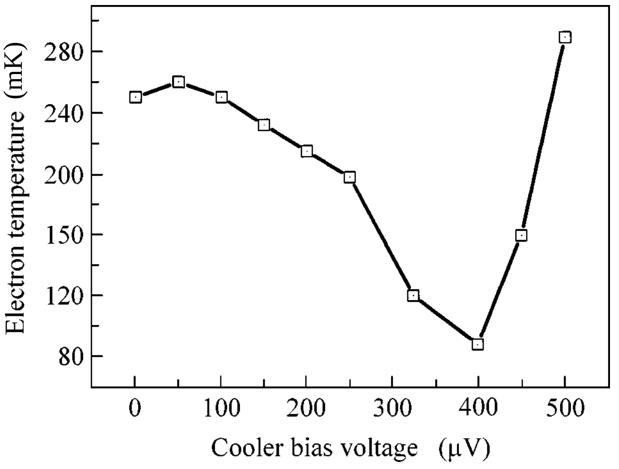

Fig. 4. Equivalent electron temperature obtained from the resistance ratio at a bias of 300 μV.

a thermometer bias of 300 μV (Fig. 4) yields a decrease in the electron temperature from the equilibrium phonon temperature of 250 down to 88 mK, i.e., by 162 mK. A noticeable difference between theory and experiment is observed for zero bias at both thermometer and cooler, when the resistance drastically increases above the expected leakage resistance. We assume that this effect is related to the Coulomb blockade in the small bridge separated from the electrodes by tunnel junctions. The slight deviation from the theory that was observed with a bias of 200 μV at the thermometer may be related to an additional cooling of the absorber phonon system due to the electron cooling.

The limiting parameters of a normal-metal hot-electron bolometer strongly depend on the overheating by the external background radiation and the overheating by the leakage current through the defects of the tunnel barriers in the tunnel junctions of both thermometer and cooler. The real electron temperature of the bolometer may exceed the phonon temperature by 100 mK or more. The use of electron cooling makes it possible to considerably reduce the effect of this parasitic overheating and to improve the bolometer characteristics. In our samples at a temperature of 250 mK, the use of electron cooling allowed us to increase the temperature response from 1.6 to 2.1 mV/K, which corresponds to Eq. (7) for not strongest possible cooling and not optimum bias. Theoretical estimates made for an ideal SIN junction yield greater values for electron cooling and greater improvement for the bolometer parameters. However, in real junctions, the presence of the shunting leakage resistance considerably affects the results.

CONCLUSIONS

Thus, we developed, fabricated, and studied normal-metal hot-electron bolometers with an electron cooler on the basis of a superconducting tunnel junction. The electron cooling makes it possible to increase the response of the bolometer and to reduce the NEP. To estimate the electron temperature, we suggested to use the criterion of the resistance ratio of the tunnel junction at finite bias voltages. We obtained a cooling of the electron subsystem from the equilibrium phonon temperature of 250 mK down to 90 mK.

This work was supported by the INTAS (grant no. 01-686) and STINT.

REFERENCES

1. L. Kuzmin, Physica B (Amsterdam) **284–288**, 2129 (2000).
2. M. Tarasov, M. Fominsky, A. Kalabukhov, and L. Kuzmin, JETP Lett. **76**, 507 (2002).
3. L. Kuzmin, I. Devyatov, and D. Golubev, Proc. SPIE **3465**, 193 (1998).
4. M. Nahum, T. M. Eiles, and J. M. Martinis, Appl. Phys. Lett. **65**, 3123 (1994).
5. M. Leivo, J. Pecola, and D. Averin, Appl. Phys. Lett. **68**, 1996 (1996).
6. F. W. J. Hekking and Yu. Nazarov, cond-mat/9302034 (1993).
7. A. Bardas and D. Averin, Phys. Rev. B **52**, 12873 (1995).
8. J. Jochum, C. Mears, S. Golwala, *et al.*, J. Appl. Phys. **83**, 3217 (1998).
9. D. Quirion, F. Lefloch, and M. Sanquer, Physica E (Amsterdam) **12**, 934 (2002).

Translated by E. Golyamina

JETP Letters, Vol. 78, No. 11, 2003, pp. 718–721. Translated from Pis'ma v Zhurnal Éksperimental'noĭ i Teoreticheskoĭ Fiziki, Vol. 78, No. 11, 2003, pp. 1232–1236.

Photostimulated Phenomena in Relaxors

R. F. Mamin[1, *], S. A. Migachev[1], M. F. Sadykov[1], I. V. Lunev[2],
V. V. Izotov[2], and Yu. A. Gusev[2]

[1] *Zavoĭskiĭ Physicotechnical Institute, Kazan Scientific Center, Russian Academy of Sciences,*
Sibirskiĭ trakt 10/7, Kazan 29, 420029 Tatarstan, Russia
**e-mail: mamin@dionis.kfti.knc.ru*
[2] *Kazan State University, ul. Lenina 18, Kazan, 420008 Tatarstan, Russia*

Received October 20, 2003

The action of illumination on the conducting and dielectric properties of lead magnoniobate was investigated. The photostimulated currents were examined and the spectral dependence of photoconductivity in the region of diffuse phase transition was obtained. It was found that the illumination affects the dielectric properties and that its action is memorized at temperatures below room temperature. The role of defect states in the formation of relaxor properties is discussed on the basis of the obtained data. © *2003 MAIK "Nauka/Interperiodica".*

PACS numbers: 72.40.+w; 77.22.-d; 77.84.-s

Ferroelectrics with diffuse phase transitions, usually called relaxors, belong to a large group of materials with a mixed composition, most of which have either the perovskite or the tungsten bronze structure. These compounds are the subject of persistent and intensive investigation, and many unusual physical properties have been revealed for them to date [1–9]. A distinctive feature of these compounds is the presence of a broad diffuse maximum in the temperature behavior of the dielectric constant and its strong frequency dependence at relatively low frequencies (10^{-2}–10^{6} Hz) that are untypical of conventional ferroelectrics. Among the relaxor family, the best known are lead magnoniobate $Pb(Mg_{1/3}Nb_{2/3})O_3$ (PMN) compounds [2–8], which serve as model objects in studying the relaxor behavior. Although these compounds have rather long been explored, no adequate understanding of the physical mechanisms underlying the processes occurring in them and no unambiguous interpretation of the observed phenomena have been attained as yet [4, 5, 9]. There are several ways in interpreting the nature of relaxors. Relaxors were originally treated as objects with local phase transition temperatures [1]. More recently, the idea of superparaelectric state of relaxors has emerged [2]. In the last few years, approaches have been developed that either consider relaxors as objects with the glass behavior [3, 4] or are based on the phenomenological models in which the system is divided into nanoregions arising under the action of random fields [5–7]. To elucidate the motive force for the relaxor behavior and develop an adequate model, the theoretical results must be checked against the experimental data that would reveal the specific features inherent in one or another model.

In recent years, certain progress has been achieved in the description of the relaxor behavior using a model that relates it to the dynamics of inhomogeneous polarization anchoring to the nanoregions as a result of charge localization on defects [10, 11]. Because of this, the problem of studying the properties of the relaxor defect states in an effort to alter the dielectric properties of relaxors through the action on the defects has become a topical problem. For this purpose, the spectral dependence of photostimulated currents was measured and the influence of illumination on the dielectric properties of lead magnoniobate single crystals was studied in this work.

All measurements were made with a PMN sample 6.2 × 4.5 × 0.65 mm in size. Transparent electrodes were applied to the optically processed largest sample surfaces oriented in the [110] plane. In all experiments, the samples were illuminated through the transparent electrodes. The photocurrent was detected using a U5-9 electrometric dc amplifier. The electrical conductivity was measured using the U5-9 amplifier and an E6-13A teraohmmeter. The dielectric measurements were performed in the frequency range 1–10^{6} Hz using a computer-interfaced automated complex. The light illumination was provided by gas-discharge xenon or halogen incandescent lamps through an MDR-12 wide-aperture monochromator with a triple quartz condenser at its input. The radiation intensity at the monochromator output was estimated using either an IMO-2 mean-power meter or a BKM-5a bolometer in the range 350–1000 nm and was found to be 0.5–7.5 mW/cm^2. The radiation wavelength was swept with a constant rate, which was usually varied from 20 to 80 nm/min. If required, the width of emission spectrum could also be varied, and the majority of data were obtained for a width of 9.6 nm. In the course of measurements, the sample temperature was maintained constant through blowing dry gaseous nitrogen and monitored by a copper–constantan thermocouple with an accuracy no worse than 0.02 K.

The studies of the dc conductivity of lead magnoniobate showed that the crystal conduction above room temperature is controlled by the thermal activation from the defect levels. The activation energy was found to be about 0.65 eV. The photoconductivity spectra measured at different temperatures show several maxima. A pronounced photocurrent maximum appears at 2.85 eV. The photoconductivity rapidly increases with temperature. Figure 1 shows the spectral dependence of the photostimulated currents in lead magnoniobate single crystals in the blue and ultraviolet regions at room temperature. The first peak with a maximum at 2.85 eV corresponds to the density of defect states lying below the conduction band bottom. Similar behavior was observed in [8] for the [100] orientation. The second peak at 3.8 eV corresponds to the photostimulated current that appears due to the direct charge-carrier transition from the valence band to the conduction band. This current was not observed in [8]. It is caused by the Dember effect in the range of strong light absorption, because the sample was illuminated through the transparent electrodes. The direction of this current depends on the sweeping direction, i.e., on whether the wavelength increases or decreases on sweeping. The current magnitude also depends on the sweeping rate. The spectrum shown in Fig. 1 corresponds to the case of decreasing wavelength. On sweeping in the direction of increasing wavelength, the photostimulated current flows in the opposite direction, i.e., against the applied field. After switching off the voltage, the currents with a maximum at 3.8 eV do not change in magnitude or direction. This suggests that the photostimulated current due to the Dember effect is much stronger than the usual photoconduction current in this spectrum range. The Dember mechanism is schematically illustrated in Fig. 2. It is caused by the appearance of a nonuniform charge-carrier spatial distribution $f(x)$ along the sample in the range of strong light absorption. In our case, the specificity of the Dember effect is that the photocurrent arises not only due to the nonuniform charge-carrier distribution $f(x)$ along the sample but also because this distribution changes with changing light wavelength. From the totality of spectroscopic data and the photoconduction data, one can draw the conclusion that there is a rather broad energy distribution of defect levels near the conduction band bottom. The possible role of these states in the formation of a diffuse phase transition in relaxors and the ways of light radiation action on relaxors are revealed in our further studies of dielectric properties.

The dielectric properties were studied at different temperatures and frequencies before and after the illumination. When measuring, the illumination was switched off to exclude the light-induced sample heating. After annealing the sample for 1 h at a high temperature ($T \sim 600$ K), the sample was cooled to the measurement temperature. The dielectric data show a typical relaxor behavior (inset in Fig. 3a) and coincide with the data obtained by other authors [5]: the temperature maximum is diffuse and strongly depends on frequency at low frequencies. The illumination noticeably affects the dielectric constants. The frequency-dependent real ε' and imaginary ε'' parts of the dielectric constant of lead magnoniobate single crystals measured at temperature $T = 270$ K are shown in Fig. 3. After annealing and cooling to 270 K, the dielectric constant was measured at different frequencies (shown by lines with circles in Fig. 3). After this, the sample was exposed to broadband ultraviolet illumination (λ ~ 350–450 nm). After the illumination was switched off and the temperature was stabilized at 270 K, the dielectric constant was again measured at different frequencies (lines with squares in Fig. 3). Thereafter the sample was illumi-

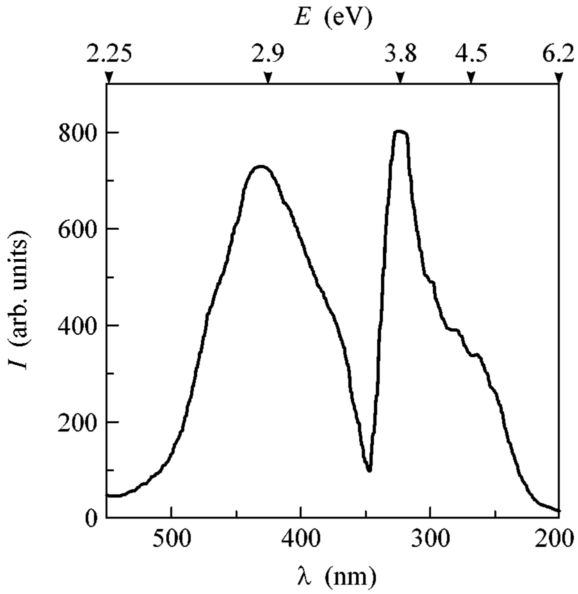

Fig. 1. Spectral dependence of photostimulated currents for lead magnoniobate single crystals at room temperature.

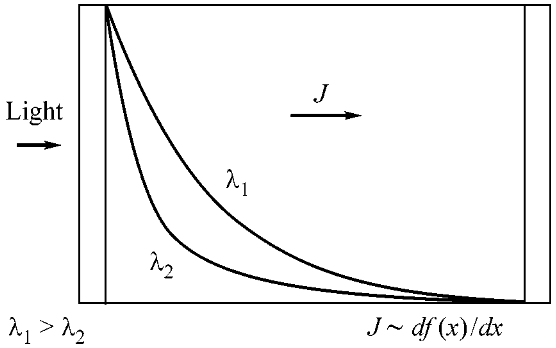

Fig. 2. Schematic illustration of the Dember effect. The curves show the distribution $f(x)$ of excited charge carriers along the sample for two different wavelengths.

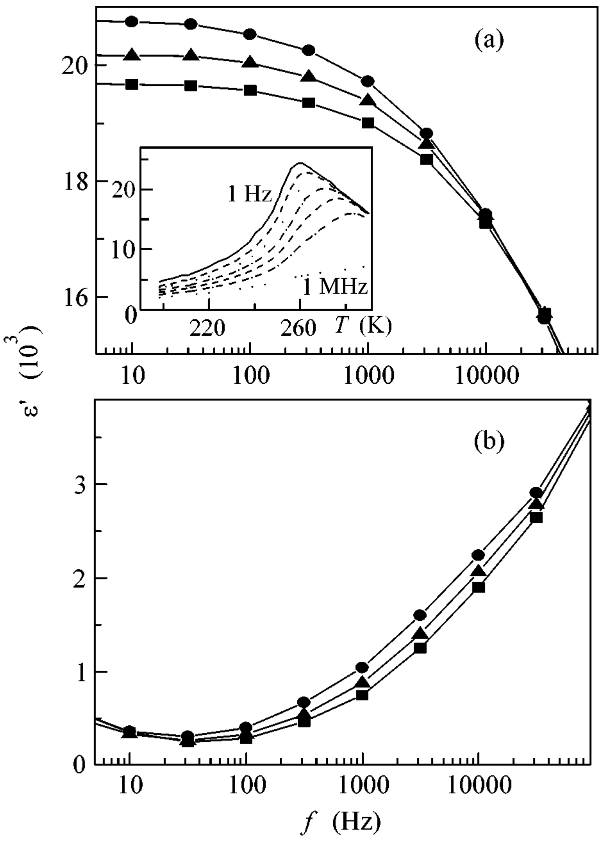

Fig. 3. Frequency dependences of the (a) real ε'(f) and (b) imaginary ε"(f) parts of dielectric constant for lead magnoniobate single crystals at temperature T = 270 K: (lines with circles) before illumination, (lines with squares) after ultraviolet illumination, and (lines with triangles) after repeated illumination by infrared light (f in Hz). Inset in (a): temperature dependence of the real ε'(f) part of dielectric constant at frequencies 1, 10, …, 10^5, and 10^6 Hz.

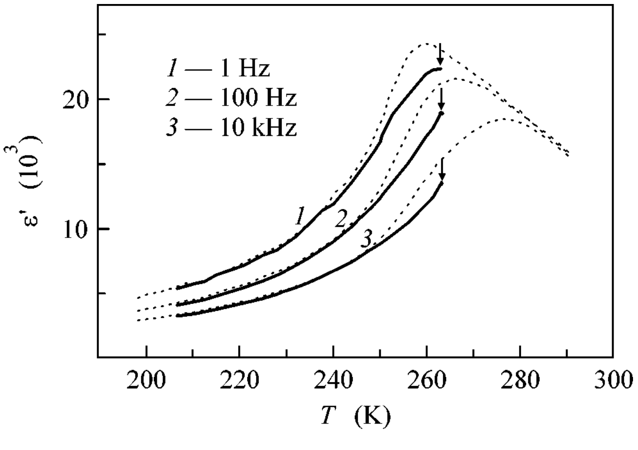

Fig. 4. Temperature dependences of the real part ε'(f) of dielectric constant for different frequencies (dotted lines) before illumination and (solid line) after ultraviolet illumination at a temperature of 263.5 K. Frequency f = (*1*) 1, (*2*) 100, and (*3*) 10 000 Hz. For comparison, the values of dielectric constant measured for the same frequencies before illumination are shown by the dotted lines.

nated again, but by a broadband infrared radiation near a wavelength of 1 μm. The results are shown in Fig. 3 by the lines with triangles. One can see from these results that the ultraviolet light strongly reduces both real and imaginary parts of the dielectric constant, while the infrared light exerts a partial restoring action. An important point is that the illumination decreases, rather than increases, the imaginary part of dielectric constant. This signifies that the observed effects cannot be associated with the increase in the sample conductivity.

Similar results were obtained for other temperatures. The measurement procedure was the same, starting with the high-temperature annealing. The effect was most pronounced in the region of maximal real part of dielectric constant. It persisted over a prolonged period (more than a day) and appeared at temperatures lower than the illumination temperature. The temperature behavior of the real part of dielectric constant at different frequencies after ultraviolet illumination at a temperature of 263.5 K and subsequent cooling is shown in Fig. 4. For comparison, the values of dielectric constant at the same frequencies are shown by the dotted lines in Fig. 4 for a nonilluminated sample. Upon further sample heating to the illumination temperature, we obtained the same values of dielectric constant as were obtained directly after illumination. The effect rapidly disappears upon heating above room temperature (T ~ 400 K).

We now discuss the electronic properties that can show up in the relaxor behavior of a defect system. The activation energy correlates well with the gap between the energy of charge-carrier localization on defects and the conduction band. The same energies account well for the temperature dependence of the relaxation-time distribution function [11] that is widely used to interpret the experiments with relaxors. It follows from the photoconductivity spectra that the energy distribution of defect levels is rather broad. This also correlates with the position that the broad distribution of relaxation times is associated with the broad energy distribution of defect states [11]. The luminescence data for lead magnoniobate [12] suggest that the carrier localization temperature is close to the phase transition temperature. The defect density in the samples is more indirect evidence counting in favor of the correlation between the defect subsystem and the relaxor behavior. From our data on photoelectron state relaxation in PMN and from the data for other samples, this density can be estimated at 10^{18}–10^{19} cm^{-3}. This corresponds to a mean distance of 3–10 nm between the defects, which coincides well with the experimentally observed sizes of the polarization inhomogeneity nanoregions [13]. One can thus assume that the inhomogeneous polarization arises due to the anchoring of polarization vectors to the defects.

The data on a photostimulated change in the dielectric properties are the most convincing results that count in favor of the correlation between the relaxor behavior and the defect subsystem. The fact that the dielectric constant undergoes an appreciable photostimulated change is evidence that the defect charge-exchange dynamics should necessarily be taken into account when discussing the nature of relaxors. The influence of illumination on the phase transitions in ferroelectrics was observed earlier in [14]. However, this effect showed itself as a shift in the phase transition temperature and was observed only under illumination. The distinctive feature of our experiments is that the effect of illumination was observed after switching off the light, and it manifested itself in an appreciable change of the dielectric parameters of the sample.

In recent years, particular interest in the complex systems composed of several subsystems has been expressed by researchers in various fields of science. A new division of science—synergetics—has emerged. In our case, the properties of the lattice subsystem are changed by the action on the other subsystem—defect electronic subsystem—and these changes are memorized by the whole system. Therefore, relaxors exemplify the synergistic behavior caused by the appearance of spatially inhomogeneous states.

Although our study does not lay claim to the ultimate solution of the problem of relaxor behavior it nevertheless outlines the way for further inquiries with the object of determining the physical nature of relaxor behavior and revealing new properties of these materials. One such property—photostimulated change in the dielectric constant—has been observed and is reported in this work.

In summary, the spectral dependences of photoconductivity, photostimulated currents appearing in the absence of external voltage, and a photostimulated change in the dielectric properties of lead magnoniobate $PbMg_{1/3}Nb_{2/3}O_3$ have been studied in this work. The data obtained were used to reveal the density of defect states, and the possible role of these states in the formation of a diffuse phase transition in relaxors has been discussed. It has been shown that the action of light on the electronic properties of the defect subsystem can alter the dielectric properties of relaxors.

We are grateful to G.B. Teĭtel’baum for discussion of results. This work was supported by the Russian Foundation for Basic Research, project no. 01-02-16350.

REFERENCES

1. G. A. Smolenskiĭ, V. A. Isupov, A. I. Agranovskaya, and S. N. Popov, Fiz. Tverd. Tela (Leningrad) **2**, 2906 (1961) [Sov. Phys. Solid State **2**, 2584 (1961)].
2. L. E. Cross, Ferroelectrics **76**, 241 (1987).
3. R. Blinc, J. Dolinsek, A. Grigorovic, *et al.*, Phys. Rev. Lett. **83**, 424 (1999).
4. E. V. Colla, L. K. Chao, and M. B. Weissman, Phys. Rev. Lett. **88**, 017601 (2002).
5. A. E. Glazounov and A. K. Tagantsev, Phys. Rev. Lett. **85**, 2192 (2000).
6. V. Westphal, W. Kleemann, and M. D. Glinchuk, Phys. Rev. Lett. **68**, 847 (1992).
7. W. Kleemann, Int. J. Mod. Phys. B **7**, 2469 (1993).
8. V. A. Trepakov, N. N. Kraĭnik, and A. V. Olifir, Fiz. Tverd. Tela (Leningrad) **18**, 1751 (1976) [Sov. Phys. Solid State **18**, 1019 (1976)].
9. V. V. Gladkiĭ, V. A. Kirikov, S. V. Nekhlyudov, *et al.*, Pis’ma Zh. Éksp. Teor. Fiz. **71**, 38 (2000) [JETP Lett. **71**, 24 (2000)].
10. R. F. Mamin, Pis’ma Zh. Éksp. Teor. Fiz. **58**, 534 (1993) [JETP Lett. **58**, 538 (1993)].
11. R. F. Mamin, Izv. Ross. Akad. Nauk, Ser. Fiz. **67**, 1160 (2003).
12. R. F. Mamin, S. A. Migachev, I. I. Nikitin, *et al.*, Ferroelectrics **291**, 101 (2003).
13. S. B. Vakhrushev, A. A. Naberezhnov, B. Dkhil, *et al.*, AIP Conf. Proc. **677**, 74 (2003).
14. V. M. Fridkin, *Photoferroelectrics* (Nauka, Moscow, 1976; Springer, Berlin, 1979).

Translated by V. Sakun

JETP Letters, Vol. 78, No. 11, 2003, pp. 722–725. Translated from Pis’ma v Zhurnal Éksperimental’noĭ i Teoreticheskoĭ Fiziki, Vol. 78, No. 11, 2003, pp. 1237–1241.
Original Russian Text Copyright © 2003 by Tovstonog, Bisti.

Plasmons in Double Quantum Wells in a Parallel Magnetic Field

S. V. Tovstonog and V. E. Bisti*
Institute of Solid-State Physics, Russian Academy of Sciences, Chernogolovka, Moscow region, 142432 Russia
**e-mail: bisti@issp.ac.ru*

Received October 24, 2003

Collective intraband charge-density excitations in the quasi-two-dimensional electron system of double GaAs/AlGaAs quantum wells in an external parallel magnetic field $B_{||}$ are studied by inelastic light scattering. It has been found that the energy of the excitations under study (acoustic and optical plasmons) exhibits anisotropy depending on the mutual orientation of $B_{||}$ and the excitation quasi-momentum k. It is shown theoretically that, in a strong parallel magnetic field, the effects associated with the finite width of the quantum wells dominate over the effects associated with interlayer tunneling and determine the anisotropy of plasmons. The experimental data are compared with a theoretical calculation. © *2003 MAIK “Nauka/Interperiodica”.*

PACS numbers: 73.21.Fg; 73.20.Mf

The effect of an external magnetic field on two-dimensional electron systems (2DESs), which can be exemplified by both single (SQWs) and double (DQWs) quantum wells, have long been investigated; however, this effect is still of great theoretical and experimental interest. Nevertheless, whereas the properties of collective excitations in 2DESs in a perpendicular magnetic field have been investigated rather extensively (see, for example, [1, 2]), the papers devoted to the consideration of the effect of a parallel magnetic field on the spectrum of excitations in 2DESs are relatively few in number [3–6].

It is known [7] that two plasma modes are present in the spectrum of collective charge-density (CD) excitations in a DQW. For a system of two electron layers without tunneling, one of the modes is the optical plasmon (OP) with a square-root dispersion law, which corresponds to in-phase oscillations of the charge density in the layers, and the other one is the acoustic plasmon (AP) with a linear dispersion law, which corresponds to antiphase oscillations. In addition, there exist single-particle excitations (SPEs) of the 2D electron gas.

The aim of this work was an experimental and theoretical investigation of the spectrum of collective excitations in a DQW in an external parallel magnetic field. Collective intraband CD excitations in double GaAs/AlGaAs quantum wells were studied by inelastic light scattering. The effect of the mutual orientation of the parallel magnetic field and the excitation quasi-momentum on the energy spectrum of excitations was investigated. It has been found that the energies of the excitations under study (optical and acoustic plasmons) depend on the mutual orientation of the magnetic field and the excitation quasi-momentum. The anisotropy of the spectra of excitations due to the parallel magnetic field was considered theoretically as a function of such DQW factors as the finite width of the quantum wells and tunneling between them. The theoretical and experimental results were compared with each other.

I. Two high-quality samples grown by molecular beam epitaxy (MBE) were investigated in this work. The samples were two GaAs quantum wells separated with an AlGaAs barrier symmetrically doped on both sides with a Si δ layer. Structure A was a DQW with well widths of 200 Å and a distance of 25 Å between the well boundaries (200/25/200); structure B was a 250/200/250 DQW. The mobility of 2D electrons was of the order of 10^6 cm^2 V^{-1} s^{-1}. The photoexcitation of the system was carried out by a Ti:sapphire laser tunable in the range 1.545–1.571 eV with the characteristic power density W = 1–10 W/cm^2 and also by a He–Ne laser with a photon energy of 1.958 eV (W = 0.01–0.1 W/cm^2). Inelastic light scattering spectra were detected by a CCD camera and a triple T64000 monochromator, which provided a spectral resolution of 0.02 meV. The high quality of the samples was confirmed by the small line widths obtained in the inelastic light scattering and photoluminescence spectra (of order 0.15 meV). Raman spectra were measured at a temperature of 4.2 K using a dual optical fiber system [8] in a cryostat with a horizontal orientation of the magnetic field. Part of the measurements was performed in a cryostat with the Faraday geometry. The concentration of two-dimensional electrons (n) for both samples was determined by magnetoluminescence measurements [9]. The total concentration was 7.2×10^{11} cm^{-2} for DQW A(200/25/200) and 1.65×10^{11} cm^{-2} for DQW B(250/200/250) under minor illumination by the He–Ne laser [10]. It was possible to vary the angle between the excitation quasi-momentum and the direction of the parallel magnetic field in the range from 0 to 360° by rotating the insert around the vertical axis. In this way, the anisotropy of the spectrum of excitations of a DQW can be investigated.

Figure 1 presents inelastic light scattering spectra for the two DQW samples: 250/200/250 on the left-hand side and 200/25/200 on the right-hand side. The spectra were measured in the cryostat with a parallel orientation of the magnetic field at the excitation quasi-momentum $k = 13 \times 10^4$ cm^{-1}. The spectra measured in the parallel magnetic field $B_{\parallel} = 7$ T at two different values of the angle φ between the direction of the excitation quasi-momentum and the direction of the magnetic field are shown in the left-hand and right-hand sides of Fig. 1 for (a) $\varphi = 180°$ and (b) $\varphi = 90°$. The case of a zero magnetic field corresponds to curves (c). The spectra of excitations of DQW 250/200/250 (left-hand side of Fig. 1) exhibit two modes: the low-energy line corresponds to the AP, and the high-energy line corresponds to the OP. The spectra demonstrate that the energy of both plasmons increases as the angle φ varies from 90° to 180°. The spectra of excitations of DQW 200/25/200 (right-hand side of Fig. 1) exhibit only one mode, which corresponds to the AP. It is seen in the figure that, as in the previous case, the excitation energy is higher when the quasi-momentum is parallel to the magnetic field.

As was mentioned above, it was possible to vary the angle between the quasi-momentum and the vector of the parallel magnetic field continuously by rotating the insert around the vertical axis, which allowed the anisotropy of excitations of the double quantum wells to be investigated. Black squares in Fig. 2 indicate the dependence of the AP energy on the angle between k and $B_{\parallel}$ in Cartesian coordinates for DQW 200/25/200 at equal concentrations in both wells (symmetric case, $n_1 = n_2 = 3.6 \times 10^{11}$ cm^{-2}). As is seen in the figure, the AP energy exhibit noticeable anisotropy and reaches a minimum (maximum) at the perpendicular (parallel) orientation of the excitation quasi-momentum with respect to the magnetic field. The spectra of excitations of DQW 250/200/250 exhibit two modes of plasma oscillations: the acoustic and optical plasmons. It was possible to change the concentration in the DQW by minor illumination with the He–Ne laser, which allowed an asymmetric case corresponding to unequal concentrations of electrons in the wells ($n_1 = 1.1 \times 10^{11}$ cm^{-2} and $n_2 = 5.5 \times 10^{10}$ cm^{-2}) to be investigated. Black squares in Fig. 3 indicate the result of processing the experimental data. It is seen in the figure that, as in the previous case, the dependence of the AP energy (on the left) and the OP energy (on the right) on the angle is symmetric and a minimum (maximum) is reached at the same values of the angle $\varphi = 90°$ and 270° ($\varphi = 0°$ and 180°). It should be noted that a small increase in the plasmon energy upon changing the mutual orientation of k and $B_{\parallel}$ from perpendicular to parallel in a single heterojunction was noted in [3].

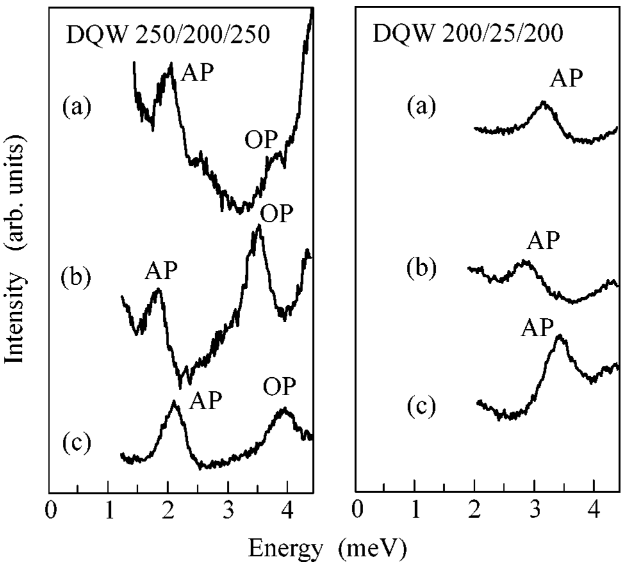

Fig. 1. Inelastic light scattering spectra in the double quantum wells 200/25/200 with concentrations $n_1 = n_2 = 3.6 \times 10^{11}$ cm^{-2} (on the right) and 250/200/250 with concentrations $n_1 = 1.1 \times 10^{11}$ cm^{-2} and $n_2 = 5.5 \times 10^{10}$ cm^{-2} (on the left) at the excitation quasi-momentum $k = 13 \times 10^4$ cm^{-1}. Curves (a) and (b) correspond to the spectra measured in the parallel magnetic field $B_{\parallel} = 7$ T at two values of the angle φ (180° and 90°, respectively); curves (c) correspond to the spectra measured in a zero magnetic field.

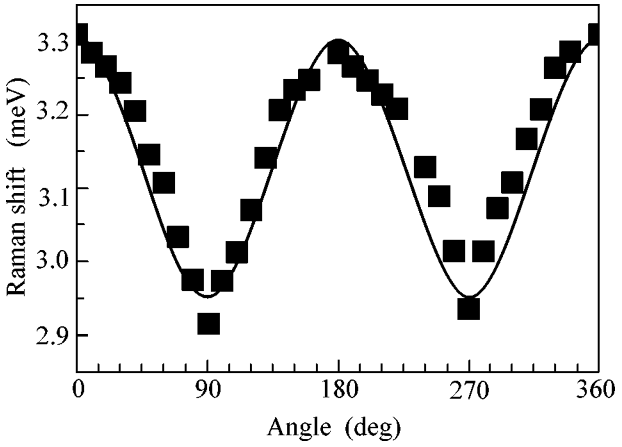

Fig. 2. Dependence of the AP energy in the double quantum well 200/25/200 on the angle between the excitation quasi-momentum in the plane $k = 13 \times 10^4$ cm^{-1} and the direction of the parallel magnetic field $B_{\parallel} = 7$ T in Cartesian coordinates at equal concentrations in both wells ($n_1 = n_2 = 3.26 \times 10^{11}$ cm^{-2}). Black squares are experimental points; the theoretical curve is shown with a solid line.

II. To determine the energy of plasmons (CD excitations) theoretically, it is sufficient to use the random phase approximation (RPA) [11, 12] without regard for the electron exchange interaction. Thus, for the case of

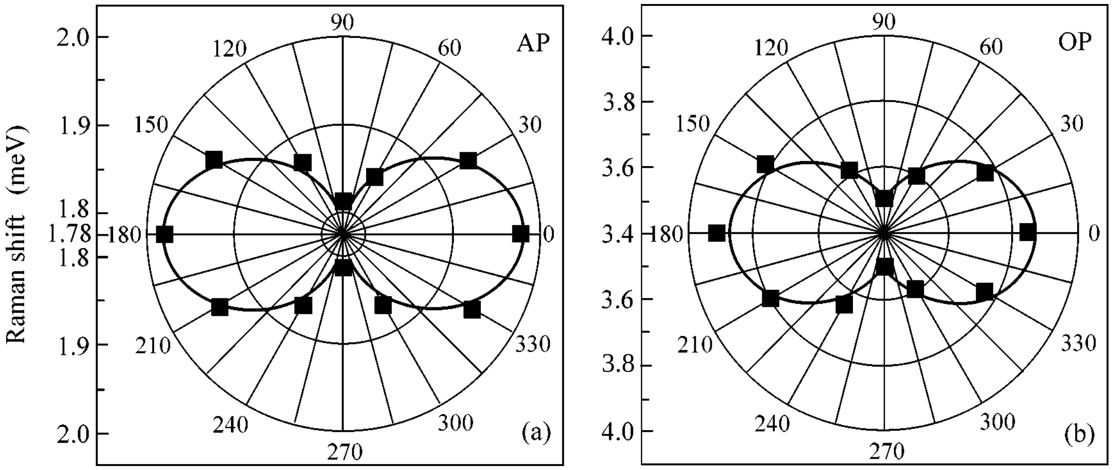

Fig. 3. Dependence of the (a) AP and (b) OP energies in the double quantum well 250/200/250 on the angle between the excitation quasi-momentum in the plane $k = 13 \times 10^4$ cm^{-1} and the direction of the parallel magnetic field $B_{\parallel} = 7$ T in polar coordinates at unequal concentrations in both wells ($n_1 = 1.1 \times 10^{11}$ cm^{-2} and $n_2 = 5.5 \times 10^{10}$ cm^{-2}). Black squares are experimental points; the theoretical curves are shown with solid lines.

infinitely thin electron layers with equal concentrations N without regard for interlayer tunneling, the energies of plasma oscillations in the absence of the parallel magnetic field equal

$$\omega_{OP} = \left(\frac{4\pi e^2 Nk}{\varepsilon m}\right)^{1/2}, \quad \omega_{AP} = k v_F \frac{1 + 2b/a_B}{(1 + 4b/a_B)^{1/2}}, \qquad (1)$$

where b is the interlayer distance, k is the excitation momentum, a_B is the electron Bohr radius, k_F is the Fermi momentum, and $v_F = \hbar k_F/m$. Taking into account the finite layer thickness leads to a change in the interaction between electrons and, hence, to the following change in the dispersion law of plasmons:

$$\omega_{OP,\,AP} \longrightarrow \omega_{OP,\,AP}(1 - \mathrm{const}\,ka), \qquad (2)$$

where a is the characteristic layer thickness; however, this change is insignificant at $ka \ll 1$.

The effect of weak tunneling ($E_0 \gg \Delta_{SAS}$, where E_0 is the energy of the lowest level and Δ_{SAS} is the splitting of the energy levels) in the region of frequencies $\omega \gg \Delta_{SAS}$ is also reduced to only small corrections [13, 14].

The spectrum of collective excitations in DQWs placed in a strong magnetic field parallel to the planes of electron motion is determined by the simultaneous action of such factors as the magnetic field, the finite width of the quantum wells, and tunneling. The effect of a parallel magnetic field for the case of infinitely thin layers but finite tunneling was considered in [15]. However, this case is not sufficiently realistic, because tunneling is always associated with the finite width of the layers. Moreover, the integral formulas and unduly small-scale plots given in this work render a comparison with experiment impossible. The results of a particular numerical calculation for a wide quantum well, which, in a strong magnetic field, bears a similarity to a DQW, are given in [16]. The necessary factors have been taken into account, but it is difficult to trace the contribution of each of them.

Therefore, in what follows, the contribution of each of the determining factors to the plasmon spectrum is considered separately and the general regularities are revealed.

In the general case, the electron wave functions are found from the Schrödinger equation for an electron in the external potential $V_{DQW}(z)$, the parallel magnetic field B, and the self-consistent Hartree potential $V_H(z)$

$$\left(\frac{\hbar^2}{2m}(k_x - eBz)^2 + \frac{\hbar^2 k_y^2}{2m} + V_{DQW}(z) + V_H(z)\right)\Psi_{lk}(z) = E_l(k)\Psi_{lk}(z). \qquad (3)$$

It is suggested that the magnetic field in this equation can be considered as a perturbation ($\hbar\omega_c \ll E_l$).

For two infinitely thin electron layers without regard for tunneling, the parallel field leads to a shift of the dispersion curves

$$\begin{aligned} E_{01} &= E_0 + \frac{\hbar^2}{2m}((k_x + k_H)^2 + k_y^2), \\ E_{02} &= E_0 + \frac{\hbar^2}{2m}((k_x - k_H)^2 + k_y^2), \end{aligned} \qquad (4)$$

where $k_H = b/2l_H^2$, l_H is the magnetic length ($z = 0$ corresponds to the middle position between the layers). In this case, the energy of plasma oscillations remains unchanged.

For two layers of finite thickness, the result in the first-order perturbation theory is analogous to the preceding one but b will be replaced by $\bar{z}_1 - \bar{z}_2$, where $\bar{z}_i = \int \Psi_i^2(z) z dz$ (i is the layer number). The second-order perturbation theory leads to anisotropy of the effective electron mass:

$$E_{01} = E_0 + \frac{\hbar^2}{2m_H}(k_x + k_H)^2 + \frac{\hbar^2}{2m}k_y^2;$$
$$E_{02} = E_0 + \frac{\hbar^2}{2m_H}(k_x - k_H)^2 + \frac{\hbar^2}{2m}k_y^2, \tag{5}$$

where

$$\frac{1}{m_H} = \frac{1}{m}(1-\gamma); \quad \gamma = \sum_l \frac{2\hbar^2|\langle z\rangle_{0l}|^2}{m l_H^4 (E_l - E_0)}. \tag{6}$$

For the case of a parabolic well (harmonic oscillator with frequency ω_0), the anisotropy of the electron mass in the parallel field can be found strictly: $\gamma = \omega_c^2/(\omega_0^2 + \omega_c^2)$ [17].

The anisotropic dispersion law for electrons leads in turn to anisotropy in the dispersion of plasmons:

$$\omega_{OP,AP} \longrightarrow \omega_{OP,AP}(1-\gamma\sin^2\varphi)^{1/2}. \tag{7}$$

For the asymmetric case (wells with different anisotropies of the electron mass γ_1 and γ_2 and different electron concentrations n_1 and n_2), the angular dependence of the OP and AP energies is also described by Eq. (7) but with the following parameters:

$$\gamma_{OP} = (\gamma_1 n_1 + \gamma_2 n_2)/(n_1 + n_2),$$
$$\gamma_{AP} = (\gamma_2 n_1 + \gamma_1 n_2)/(n_1 + n_2). \tag{8}$$

The anisotropy parameter γ can be estimated for two limiting cases: (a) a narrow rectangular well with infinite walls, $\gamma_a = 0.026(a/a_H)^4$, and (b) a triangular well (can serve as a model for a wide rectangular well with one-sided doping) $\gamma_b = 4(\langle z\rangle/a_H)^4$. For sample A, we obtain $\gamma_a = 0.4$ and $\gamma_b = 0.2$; for sample B, $\gamma_a = 0.7$ and $\gamma_b = 0.13$. The actual value of γ with regard to doping and the self-consistent potential falls within this range.

Taking into account tunneling for infinitely thin layers in a strong field ($E_F < U$, $U = \hbar^2 k_H^2/2m$) [15] also indicates that the energies of plasmons propagating along and across the field are different, but the parameter is $(\Delta_{SAS}/4U)^2$. For the samples under study ($\Delta_{SAS} <$ 1 meV), this value is approximately 10^{-2}; therefore, the effect of tunneling is insignificant.

For comparison with the experimental data, Fig. 2 presents angular dependence (7) for the AP energy at $\gamma = 0.20$ and Fig. 3 presents angular dependences (7) for the AP and OP energies at $\gamma = 0.17$ (the values of energies along the field for constructing the theoretical curves were taken from the experiment). The experimental and theoretical results are in agreement with each other.

In this work, it was found experimentally that the spectra of excitations in the system of electrons in a DQW in a strong parallel magnetic field are characterized by noticeable anisotropy. It was shown theoretically that the anisotropy of the energy of the optical and acoustic plasmons is due to the finite width of the electron layers, which manifests itself in the anisotropy of the effective mass.

The authors are grateful to I.V. Kukushkin for useful discussions and for constant attention to this work.

This work was supported by the Russian Foundation for Basic Research.

REFERENCES

1. S. V. Tovstonog, I. V. Kukushkin, L. V. Kulik, and V. E. Kirpichev, Pis'ma Zh. Éksp. Teor. Fiz. **76**, 592 (2002) [JETP Lett. **76**, 511 (2002)].
2. S. V. Tovstonog, L. V. Kulik, I. V. Kukushkin, *et al.*, Phys. Rev. B **66**, 241308 (2002).
3. V. E. Kirpichev, I. V. Kukushkin, B. N. Shepel', *et al.*, Pis'ma Zh. Éksp. Teor. Fiz. **63**, 974 (1996) [JETP Lett. **63**, 1031 (1996)].
4. L. V. Kulik, I. V. Kukushkin, V. E. Kirpichev, *et al.*, Phys. Rev. B **66**, 073306 (2002).
5. J. Dempsey and B. I. Halperin, Phys. Rev. B **45**, 3902 (1992).
6. P. I. Tambonea and S. Das Sarma, Phys. Rev. B **49**, 16593 (1994).
7. D. S. Kainth, D. Richards, A. S. Bhatti, *et al.*, Phys. Rev. B **59**, 2095 (1999).
8. E. D. Isaacs and D. Heiman, Rev. Sci. Instrum. **58**, 1672 (1987).
9. I. Kukushkin and V. B. Timofeev, Adv. Phys. **45**, 147 (1996).
10. I. Kukushkin, K. von Klitzing, K. Ploog, *et al.*, Phys. Rev. B **40**, 4179 (1989).
11. R. Z. Vitlina and A. V. Chaplik, Zh. Éksp. Teor. Fiz. **81**, 1011 (1981) [Sov. Phys. JETP **54**, 536 (1981)].
12. S. Das Sarma and A. Madhukar, Phys. Rev. B **23**, 805 (1981).
13. G. E. Santoro and G. F. Guilliani, Phys. Rev. B **37**, 937 (1988).
14. S. Das Sarma and E. H. Hwang, Phys. Rev. Lett. **81**, 4216 (1998).
15. G. R. Aizin and Godfrey Gumbs, Phys. Rev. B **54**, 2049 (1996).
16. Shuh-Jen Cheng and R. R. Gerhards, Phys. Rev. B **65**, 085307 (2002).
17. H. Tang and P. N. Butcher, J. Phys. **21**, 3313 (1988).

Translated by A. Bagatur'yants

JETP Letters, Vol. 78, No. 11, 2003, pp. 726–729. From Pis'ma v Zhurnal Éksperimental'noĭ i Teoreticheskoĭ Fiziki, Vol. 78, No. 11, 2003, pp. 1242–1246.
Original English Text Copyright © 2003 by Teitel'baum, Kataev, Vavilova, Kuhns, Reyes, Moulton.

Interplay between the Magnetic Fluctuations and Superconductivity in Lanthanum Cuprates[¶]

G. B. Teitel'baum[1], *, V. E. Kataev[1], E. L. Vavilova[1], P. L. Kuhns[2],
A. P. Reyes[2], and W. G. Moulton[2]
[1] *Zavoĭskiĭ Institute for Technical Physics, Russian Academy of Sciences, Kazan, 420029 Tatarstan, Russia*
[2] *NHMFL, Tallahassee, FL 32310, USA*
**e-mail: grteit@dionis.kfti.knc.ru*

Received October 29, 2003

We report an analysis of the magnetic fluctuations in superconducting $La_{2-x}Sr_xCuO_4$ and related lanthanum cuprates that have different symmetry of the low-temperature structure. NMR and ESR investigations revealed a dynamical coexistence of superconductivity and the antiferromagnetic correlations in most of the superconductivity region of the phase diagram. We show that, for all compounds, regardless of their low-temperature symmetry and their superconducting properties, the enhancement of the spin stiffness near 1/8 doping takes place. *© 2003 MAIK "Nauka/Interperiodica".*

PACS numbers: 74.25.Ha; 74.72.Dn; 76.30.-v; 76.60.-k

Interest in microscopic phase separation in high-T_c superconducting materials has received a strong impetus after the discovery of stripe correlations [1]. They were observed only in compounds specially doped with rare-earth ions, whose role is to induce the low-temperature tetragonal (LTT) phase favorable for the pinning of the stripe fluctuations. Recent neutron scattering experiments [2] in the low-temperature orthorhombic (LTO) phase of $La_{2-x}Sr_xCuO_4$ with $x = 0.12$ reveal the presence of modulated antiferromagnetic order very similar to that found in LTT compound $La_{1.6-x}Nd_{0.4}Sr_xCuO_4$. However, on a larger time scale, the magnetic fluctuations in $La_{2-x}Sr_xCuO_4$ are dynamical, especially for the superconducting state, and their relevance to the stripe structure is a matter of debate. In particular, the dynamical character of the microscopic phase separation hinders the investigation of its properties by means of low-frequency local methods such as conventional NMR [3, 4].

The main aim of the present work is to analyze the phase diagram and the properties of magnetic fluctuations for superconducting $La_{2-x}Sr_xCuO_4$ and related compounds with the help of experiments whose characteristic frequency is shifted to larger values in comparison with conventional NMR. We consider ESR ($\nu \sim 10$ GHz) and high field NMR ($\nu \sim 0.1$ GHz) measurements, which are focused on a comparative analysis of the magnetic fluctuations for the different metal oxides. With this purpose, we discuss the ESR data obtained for such compounds as $La_{2-x}Sr_xCuO_4$ (LSCO) [5], $La_{2-x}Ba_xCuO_4$ (LBCO) [6], and $La_{2-x-y}Eu_ySr_xCuO_4$ (LESCO) [7] together with conventional NMR data for $La_{2-x-y}Nd_ySr_xCuO_4$ (LNSCO) [8] and new high field NMR data for superconducting LSCO. All the measurements were carried out on powder samples with various hole doping. For LSCO, the doping level covers the entire superconducting region of the phase diagram; for LBCO, we studied the doping region in the vicinity of the well-known T_c dip, whereas the LESCO and LNSCO series correspond to the nonsuperconducting LTT phase. The samples that were used for the ESR measurements were doped with 1 at. % of Gd, which was used as an ESR probe [5]. Such a tiny concentration of Gd ensured only small suppression of T_c via pair breaking.

We analyzed the temperature and concentration dependence of the width of the most intense component of the multiline Gd^{3+} ESR spectrum, corresponding to the fine splitting of the spin states $S = 7/2$ in the crystalline electric field [5]. The typical temperature dependence of the linewidth δH is shown in Fig. 1.

The temperature behavior for $T > T_c$ is qualitatively very similar for all the samples under study: a linear dependence of δH on temperature, which is followed by the rapid growth of the linewidth at low T. But, after cooling below 40 K, the behavior of superconducting and nonsuperconducting samples becomes different: the linewidth of superconducting LSCO exhibits a downturn starting at a temperature T_m dependent on x, whereas, for other samples which are not bulk superconductors, the linewidth continues to grow with further decreasing temperature (see Fig. 1).

This behavior may be explained if one takes into account that, in addition to the important but temperature-independent residual inhomogeneous broadening,

---

[¶] This article was submitted by the authors in English.

the linewidth is given by different homogeneous contributions linked to the magnetic properties of CuO_2 planes:

(i) The interaction of Gd^{3+} spins with the charge carriers, i.e., the Korringa relaxation channel. The simplest Korringa term in the linewidth is $\delta H = a + bT$ with $b = 4\pi(JN_F)^2P_M$ [9], where $P_M = [S(S + 1) - M(M + 1)]$ is the squared matrix element of the Gd spin transitions between the M and $M + 1$ states, N_F is the density of states at the Fermi level, and J is the coupling constant between the Gd and charge carrier spins [5]. The factor P_M describes the Barnes–Plefka enhancement [9] of the relaxation with respect to the standard Korringa rate. Such an enhancement occurs in exchange-coupled crystal field split systems where the g-factors of localized and itinerant electrons are approximately equal but the relaxation of conduction electrons towards the “lattice” is strong enough to inhibit bottleneck effects. For the system under study, this was discussed in [5]. Note that the enhancement of the linear slope for LESCO relative to that for LSCO seen in Fig. 1 is due to the influence of the depopulation of the first excited magnetic Eu level [7].

(ii) The interaction of Gd with copper spins, giving rise to homogeneous broadening of the Gd ESR line (a close analogue of nuclear spin-lattice relaxation):

$$\delta H = \frac{1}{2}(\gamma H)^2 P_M[(\tau/3) + (2\tau/3)/(1 + (\omega\tau)^2)], \quad (1)$$

where τ is the magnetic fluctuations lifetime and H is the internal magnetic field at the Gd site. Following [8], we assume the activation law for the fluctuation lifetime temperature dependence $\tau = \tau_\infty \exp(E_a/kT)$, with τ_∞ being the lifetime at the infinite temperature and E_a, the activation energy proportional to the spin stiffness ρ_s ($E_a = 2\pi\rho_s$).

The second contribution describes the standard Bloembergen–Purcell–Pound (BPP) behavior: the broadening of the ESR line upon cooling with the downturn at certain freezing temperature T_m corresponding to $\omega\tau = 1$. Here, ω is the resonant frequency. This expression is written for the case when the fluctuating magnetic fields responsible for Gd spin relaxation are induced by local Cu moments. In the polycrystalline samples, the averaging over the random orientation of the local Cu moments with respect to the external magnetic field yields a twofold greater probability that they will have perpendicular rather than collinear orientation.

We observed that, depending on the Sr content, the linewidth behavior transforms from a BPP-like (with the maximum at T_m) to a pure Korringa (linear) temperature dependence. Based on the observation that the relative weight of the BPP-contribution, compared with the Korringa one, decreases with increasing Sr doping, we conclude that, at low x, the Gd spin probes an almost magnetically correlated state and, at the high x end, an almost nonmagnetic metal. Such a transformation may be explained in terms of the microscopic phase separation into the metallic and AF-correlated phases. It is worth to remembering that, very soon after the discovery of high-T_c superconductivity in cuprates, it was suggested [10] that microscopic phase coexistence is an inherent feature of these materials. Note that, according to the phase diagram shown in Fig. 2, the T_m values obtained are lower than the respective T_c, although for certain hole doping, they lie close to each other. The rel-

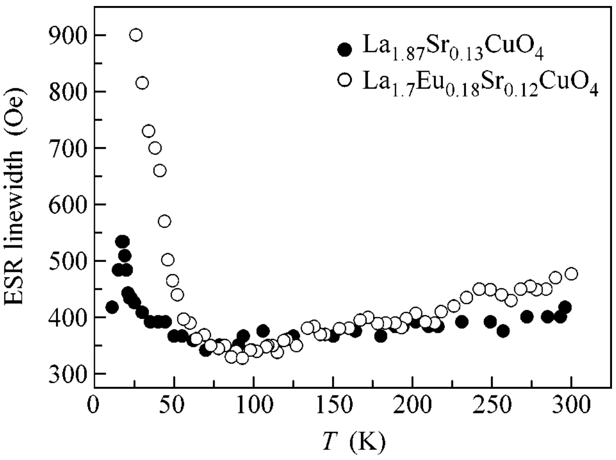

Fig. 1. Typical ESR linewidth temperature dependences for LTO, superconducting LSCO, and LTT nonsuperconducting LESCO.

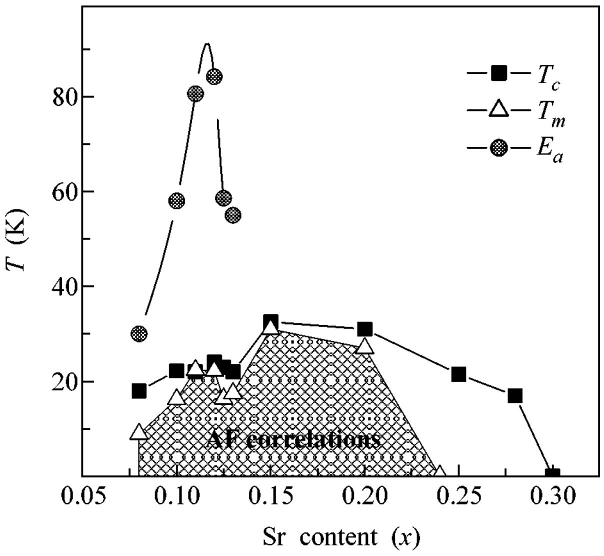

Fig. 2. Phase diagram of the magnetic fluctuations of superconducting LSCO. The triangles correspond to the magnetic transition temperature $T_m(x)$; squares, to the superconducting transition temperature $T_c(x)$; and the circles, to the magnetic fluctuations’ activation energy $E_a(x)$. The coexistence region is shown in gray.

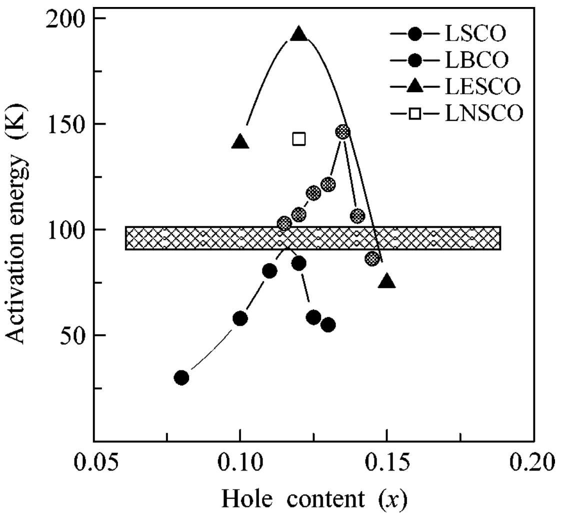

Fig. 3. Activation energies $E_a(x)$ for the magnetic fluctuations in different cuprates vs. the hole doping x. The boundary separating the $E_a(x)$ values corresponding to nonsuperconducting and bulk superconducting phases is shaded.

ative amount of the AF phase falls abruptly in the vicinity of $x = 0.20$, so that, for $x = 0.24$, any traces of it are absent. One cannot exclude that this boundary is connected with the existence of the widely discussed quantum critical point [11] at these doping values.

The different temperature dependences of the linewidths for the superconducting and nonsuperconducting compounds may be consistently explained assuming that, for the superconducting samples, the linewidth below T_c is governed by fluctuating fields which are transversal to the constant field responsible for the Zeeman splitting of the Gd spin states (the second term in Eq. (1) for δH). Since these fluctuations are induced by Cu moments lying in the CuO_2 planes, it means that Gd ions are subjected to a constant magnetic field normal to these planes. This may indicate that the magnetic flux lines penetrating the layered superconducting sample tend to orient normally to the basal planes, where the circulating superconducting currents flow (it is also possible that Gd ions pin the magnetic fluctuations connected with the normal vortex cores). An important argument in favor of the magnetic fluctuations' contribution to the Gd ESR linewidth is given by the fact that the BPP peak at $T = T_m(x = 0.10) \approx 16$ K is in a reasonable agreement with that observed near 4 K in the ^{139}La nuclear spin relaxation rate temperature dependence for LSCO with $x = 0.10$ at a frequency of 140 MHz [12].

In principle, there might also be a second possibility for different low-temperature behavior of the linewidth for superconducting samples in comparison with that for nonsuperconducting ones. The nonresonant field-dependent microwave absorption in the superconducting state may distort the shape of the ESR spectrum. But these distortions should be especially pronounced for broad lines, typically, for the samples with a small amount of holes, whereas the temperature T_m, characteristic of small x, is considerably lower than T_c. Thus, the idea that the possible distortion of the ESR line shape owing to nonresonant microwave absorption is the main reason for the apparent narrowing of the ESR line below T_c seems to be improbable.

Since the measurements were carried out in a nonzero external field, it is very important to consider the flux lattice effects. In typical ESR fields of approximately 0.3 T, oriented normally to the CuO_2 layers, the lattice period is 860 Å, whereas the vortex core sizes for LSCO are approximately 20 Å. As the upper critical field amounts to 62 T, it is clear that, in the case of ESR, the vortex cores occupy only 0.5% of the CuO_2 planes. According to [13, 14], the Cu spins in the vortex cores may be AF ordered. Therefore, the phase diagram in Fig. 2 indicates that not only the spins in the normal vortex cores are AF correlated, but the AF correlations are spread over the distances of the order of magnetic correlation length, which at low doping reaches 600–700 Å [14].

Numerical simulations of the Gd ESR linewidths for compounds with different Sr content enable us to estimate the values of the parameters in the expression for the linewidth. For example, the maximal effective internal field H in the rare-earth positions is about 200 Oe; the lifetime τ_∞, which was found to be material-dependent, for LSCO is equal to $\tau_\infty = 0.3 \times 10^{-12}$ s; and the activation energies E_a for all the investigated compounds are shown in Figs. 2 and 3. Note that, since the influence of the Nd magnetic moments for LNSCO hinders the ESR measurements, the activation energy for this compound was estimated from the measurements of the nuclear spin relaxation on Cu and La nuclei.

The enhancement of E_a (that is, of a spin stiffness ρ_s) near $x = 0.12$ shown in Fig. 3 gives evidence of developed antiferromagnetic correlations for all the investigated compounds and explains both the anomalously narrow peak in inelastic neutron scattering [15] and the elastic incommensurate peak with a narrow q-width [2] reported for superconducting $La_{2-x}Sr_xCuO_4$ for this Sr doping. This indicates the important role of commensurability and gives evidence of the plane character of the inhomogeneous spin and charge distributions. The maximal activation energies are 80 K for LSCO, 144 K for LBCO, 160 K for LESCO, and 143 K for LNSCO. Note that, for LBCO and LESCO, the signatures of the bulk superconductivity [6, 7] become visible upon the suppression (in the course of Ba or Sr doping) of the activation energy down to 80–85 K. Therefore, it is plausible to assume that these values of the activation energy are probably the critical ones for the realization of the bulk superconducting state. The corresponding boundary is shown in Fig. 3. Fluctuations with the

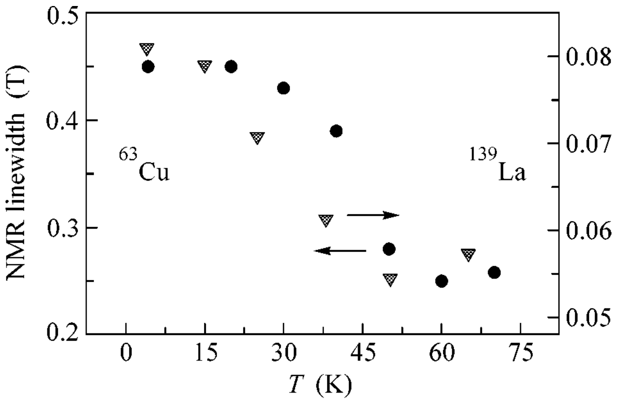

Fig. 4. Temperature dependence of the ^{63}Cu and ^{139}La NMR linewidths for superconducting LSCO with $x = 0.12$.

higher activation energies (spin stiffness) are effectively pinned and suppress the superconductivity.

To obtain information about ordered magnetic moments for compounds with enhanced spin stiffness, NMR measurements were carried out at 20–25 T in a high homogeneity resistive magnet of the NHMFL in Tallahassee (Florida). The temperature and doping dependences of ^{63,65}Cu and ^{139}La NMR field sweep spectra of the oriented powders $La_{2-x}Sr_xCuO_4$ were studied. According to the previous La NQR results [3, 12], measurements of oriented powder samples in a magnetic field perpendicular to the c axis revealed that, for Sr content near 1/8, the central lines of the observed spectra both for Cu and La exhibit broadening upon cooling below 40–50 K (Fig. 4).

Such behavior is connected with the slowing down of the magnetic fluctuations, which are gradually slowing down upon ordering. The broadening of the La NMR line allows us to estimate that the additional magnetic field at the La nucleus is 0.015 T. If we consider that, for the antiferromagnet La_2CuO_4, the copper moment of $0.64\mu_B$ induces a field of 0.1 T at the La site [16], then the effective magnetic moment in the present case is $\sim 0.09\mu_B$. Note that the manifestation of the magnetic order only in the vicinity of $x = 1/8$, when the AF structure is commensurate with the lattice, indicates that the magnetic inhomogeneities are of a plane character.

In conclusion, our investigation reveals that, for all the compounds studied irrespective of the symmetry type (LTO or LTT) in the neighborhood of 1/8 doping, enhancement of the spin stiffness takes place. Compounds with a spin stiffness larger than a certain critical value (see Fig. 3) reveal no bulk superconductivity.

According to the phase diagram, the inherent feature of the superconducting state in cuprates is the presence of frozen antiferromagnetic correlations. Such a coexistence seems to be a result of phase separation on the microscopic scale, as was discussed in the pioneering paper of Gor'kov and Sokol [10].

In the neighborhood of 1/8 doping, this coexistence may be realized in the form of dynamic stripes, since the corresponding enhancement of the spin-stiffness reveals the plane character of the spin (and charge) inhomogeneities.

One of the authors (G.B.T.) is grateful to L.P. Gor'kov for valuable discussions about the specifics of phase separation for cuprates. This work is partially supported by the Russian Foundation for Basic Research (grant no. 01-02-17533).

REFERENCES

1. J. M. Tranquada, B. J. Sternlieb, J. D. Axe, *et al.*, Nature **375**, 561 (1995).
2. T. Suzuki, T. Goto, K. Chiba, *et al.*, Phys. Rev. B **57**, R3229 (1998).
3. S. Oshugi, Y. Kitaoka, H. Yamanaka, *et al.*, J. Phys. Soc. Jpn. **63**, 2057 (1994).
4. T. Goto, K. Chiba, M. Mori, *et al.*, J. Phys. Soc. Jpn. **66**, 2870 (1997).
5. V. Kataev, Yu. Greznev, E. Kukovitskii, *et al.*, JETP Lett. **56**, 385 (1992); V. Kataev, Yu. Greznev, G. Teitel'baum, *et al.*, Phys. Rev. B **48**, 13042 (1993).
6. B. Z. Rameev, E. F. Kukovitskii, V. E. Kataev, and G. B. Teitel'baum, Physica C (Amsterdam) **246**, 309 (1995).
7. V. E. Kataev, B. Z. Rameev, B. Buechner, *et al.*, Phys. Rev. B **55**, R3394 (1997); V. E. Kataev, B. Z. Rameev, A. Validov, *et al.*, Phys. Rev. B **58**, R11876 (1998).
8. G. B. Teitel'baum, I. M. Abu-Schiekah, O. Bakharev, *et al.*, Phys. Rev. B **63**, 020507(R) (2001).
9. S. E. Barnes, Adv. Phys. **30**, 801 (1981).
10. L. P. Gor'kov and A. V. Sokol, JETP Lett. **46**, 420 (1987).
11. S. Sachdev, Rev. Mod. Phys. **75**, 913 (2003).
12. M.-H. Julien, A. Campana, A. Rigamonti, *et al.*, Phys. Rev. B **63**, 144508 (2001).
13. D. P. Arovas, A. J. Berlinsky, C. Kallin, and S. C. Zhang, Phys. Rev. Lett. **79**, 2871 (1997).
14. B. Lake, G. Aeppli, K. N. Clausen, *et al.*, Science **291**, 832 (2001).
15. K. Yamada, C. H. Lee, K. Kurahashi, *et al.*, Phys. Rev. B **57**, 6165 (1998).
16. T. Tsuda, T. Shimizu, H. Yasuoka, *et al.*, J. Phys. Soc. Jpn. **57**, 2908 (1988).

JETP Letters, Vol. 78, No. 11, 2003, pp. 730–733. From Pis’ma v Zhurnal Éksperimental’noĭ i Teoreticheskoĭ Fiziki, Vol. 78, No. 11, 2003, pp. 1247–1250.
Original English Text Copyright © 2003 by Shegeda, Lisin.

Time-Resolved Photo-Phonon Spectroscopy of Exchange Coupled Cr^{3+} Pairs in Ruby[¶]

A. M. Shegeda* and V. N. Lisin
Zavoĭskiĭ Institute for Technical Physics, Russian Academy of Sciences, Kazan, 420029 Tatarstan, Russia
**e-mail: shegeda@kfti.knc.ru*

Received October 31, 2003

A rather simple method is used to simultaneously detect both optical absorption spectra and excited-state nonradiative transitions in 0.03 and 0.16 at. % ruby at temperature 2 K. The technique utilizes a time-resolved bolometer detection of phonons generated by the excited-state nonradiative relaxation following optical excitation with a pulsed tunable dye laser. The observed excitation spectra of phonons coincide well with currently known absorption spectra of both chromium single ions and pairs of the nearest neighbors. For the first time, the fast (≤ 5 μs) resonant energy transfer from single chromium ions to the fourth nearest neighbors is observed directly. New strongly perturbed Cr-single-ion sites are observed. © *2003 MAIK “Nauka/Interperiodica”.*

PACS numbers: 78.40.Ha; 78.47.+p

The method used can be referred to as photo-phonon spectroscopy. Nonequilibrium phonons, which are created after laser pulse excitation due to radiationless relaxation, can be detected as a change in bolometer temperature in real time following laser excitation if the free length of the phonons is comparable to the distance up to the bolometer. Therefore, the bolometer signal amplitude is determined by both the absorption cross-section and the radiationless relaxation intensity, so both absorption spectra and radiationless relaxation can be studied by this method. This technique was first proposed in [1]. It is a natural development of the photoacoustic [2] method. Absorption spectra of ruby in the R_1–R_2 region were observed in [1] utilizing sinusoidally chopped light excitation. We use a pulse laser excitation and wider range of the light wavelengths than in [1]. This has allowed us to identify the lines of chromium ion pair and to calculate the fast resonant energy transfer from single ions to the fourth-nearest neighbors and new single ion sites.

The geometry of the experiment is shown in Fig. 1. The dye (oxazin 1) tunable laser is used for optical excitation of Cr^{3+} ions. It produces 8-ns light pulses with a repetition frequency of 12.5 Hz and spectral half-width of 0.1 Å at any wavelength in the range 6915–7100 Å. The ruby samples have a Cr^{3+} concentration of 0.03 and 0.16 at. % and thickness (along the C_3 axis) of 10.0 and 5.0 mm, respectively. Linearly polarized laser radiation is transmitted through a sample along the C_3 axis. The phonon pulse created upon passage of laser radiation through a sample is detected by a superconductive Sn or In bolometer. The bolometer was evaporated on one of the lateral sides of a sample. Its shape is a meander and the area is 3 mm^2. Samples are immersed in liquid helium, which is pumped down to 2 K. The working point of the bolometer is tuned to the lower part of the linear site of superconductive transition due to an external magnetic field. The bolometer signals are amplified using a wide-band preamp with a small noise signal. Data output is via stroboscopic oscilloscope. All processes of measuring (detection of a signal, its accumulation and processing, and change of the wavelength of the laser) were automated.

It is necessary to note that the laser wavelength can be changed with a step smaller than 0.005 Å; however, the reflecting monochromator used did not allow us to establish the wavelength values with such an accuracy. It was possible to establish only the relative change of the wavelength precisely enough. In addition, there is no consistency of wavelength values of the R_1 and R_2

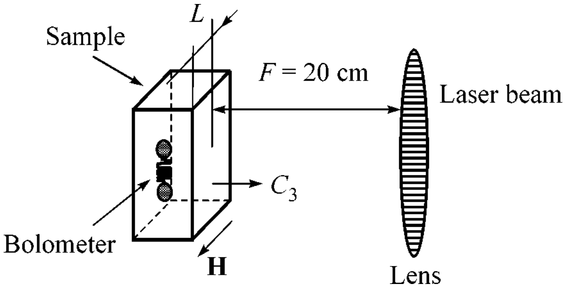

Fig. 1. Geometry of the experiment. **H** and C_3 are the directions of the exterior constant magnetic field and optical axis, L is the distance between the laser beam and the bolometer (fixed in our experiments), F is the focal distance.

[¶] This article was submitted by the authors in English.

lines of a ruby in the literature. Though some authors give it to within 0.01 Å, the wavelength value of, for example, R_1 lines at helium temperature in different works varies from 6933.6 to 6935.0 Å [3–5]. Therefore, in order to prevent confusion in the identification of lines, we further considered, as in [3] (where the complete data on absorption spectra and luminescence of the concentrated ruby are cited most), $\nu(R_1)$ = 14418.52 cm^{-1}, i.e., $\lambda(R_1)$ = 6933.6 Å.

When a sample is excited by a laser pulse, the bolometer detects a phonon pulse after some delay depending on the distance L between the impact laser point and the bolometer (L = 2.5 mm for results shown in Figs. 1–6).

Typical signals are shown in Fig. 2. The spike at the time initial moment in this figure occurs because the bolometer detects not only phonons but also the light scattered in the sample. The phonon pulses were observed throughout the investigated laser wavelength band, i.e., also at nonresonance laser excitation whose light frequency was differed from frequencies of optical transitions of both single ions as pairs of the nearest neighbors. The reason for nonresonance laser generation of these background phonons is not clear and demands separate study. During wavelength scanning, the amplitude of a bolometer signal is measured at some fixed delay after laser pulse excitation. The number of accumulations at each point is equal 50. Then, the spectrum is normalized to the background, because the dye laser pulse intensity depends on the wavelength. Below, when we speak about a phonon excitation spectrum, we mean the spectrum received.

Upon scanning the wavelength of the laser in a low concentrated ruby, we observed a change in the phonon signal only in the vicinity of the R_1 and R_2 lines (see Fig. 3).

As can be seen from this figure, a considerable decrease in the phonon signal is observed at resonant pumping of the R_1 line. This is probably caused by the decrease in background phonon generation due to absorption of a laser pulse in the volume of the sample, giving rise to a decrease in the laser pulse intensity. Growth of the phonon signal at the resonance with the R_2 line may be explained by the creation of additional 29-cm^{-1} phonons generated by the excited-state nonradiative relaxation $2\bar{A} \longrightarrow \bar{E}$ as in [6].

The most interesting results were received in the concentrated ruby sample (0.16 at. % Cr^{3+}). In our work, the transmission spectrum was measured without the use of a monochromator. The wavelength of the input laser is varied. The output laser pulse passed through a sample is detected by a photomultiplier. Rather low peak stability of dye laser pulses, plus usage of a high-speed photomultiplier, importing additional noise, as well as a smaller chromium ion concentration, resulted in that in a transmission spectrum only the R_1 and R_2 lines were well observed, as can be seen in Fig. 3. However, when we begin to detect phonon signal (and not a transmission spectrum) on a bolometer, we receive interesting and unexpected results (see Fig. 4). There is additional generation of phonons at particular excitation wavelengths.

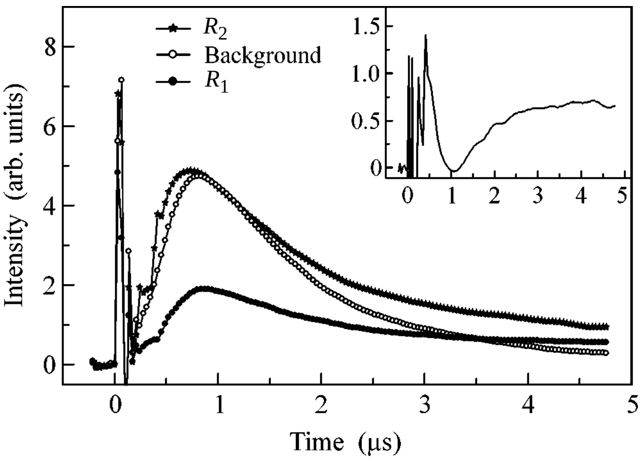

Fig. 2. Bolometer signals in the ruby (0.16 at. % Cr^{3+}) versus the time after laser pulse excitation: background—nonresonance excitation (λ = 6922 Å), R_1 and R_2—resonance excitation of the R_1 and R_2 lines. The inset shows the difference between the R_2 and background phonon signals. Time is delay time after laser pulse excitation.

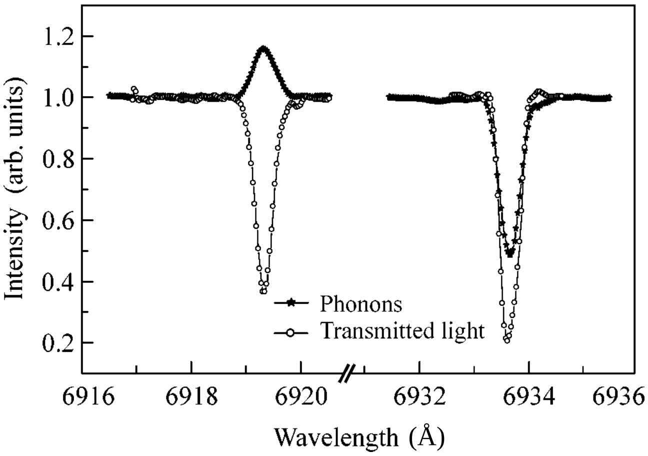

Fig. 3. Transmittivity and phonon excitation spectra near the R_1 and R_2 lines in the low concentrated ruby sample (0.03 at. % Cr^{3+}).

In Fig. 4, all known absorption lines of chromium single ions and pairs of the nearest neighbors are also shown. In view of the fact that the spectral width of the laser in our experiment was approximately 0.1 Å, the coincidence of the experimental values of wavelengths upon the excitation during which a change in the phonon signal is observed to absorption lines of the nearest neighbors is quite satisfactory. It is clear that the

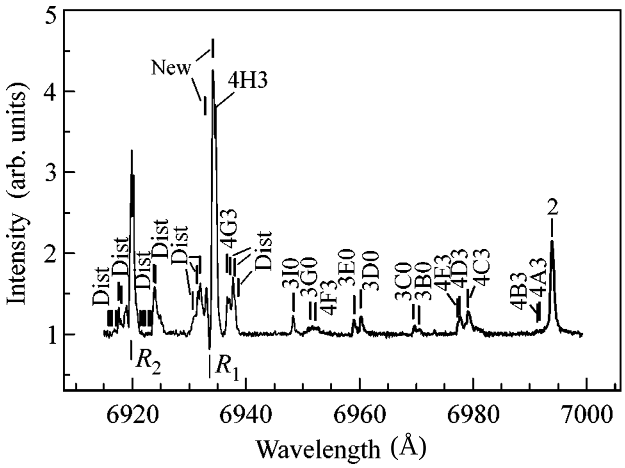

Fig. 4. Phonon excitation spectra at 3 μs delay time after the laser pulse in 0.16 at. % Cr^{3+} ruby at 2 K versus the laser wavelength. The lines show locations of all the absorption lines at 6915–7000 Å found in [3] for 4 K and polarization $\mathbf{E} \perp C_3$. Labeled as in [3]. The 4*H*3 line is not mentioned in [3], and the 4*F*3 line is mentioned in [3]; however, the transition frequency value is not given, so these values are accepted equal to the calculated values given in [3]: $\nu(4H3) = 14416.2$ cm^{-1} and $\nu(4F3) = 14379.9$ cm^{-1}. The value of frequency of transition 4*G*3 is given as in [3] for polarization $\mathbf{E} \parallel C_3$.

lines whose excitation does not accompany nonradiative transitions (4*A*3, 4*B*3) are not observed with the method used here. Therefore, it is possible to assume that the change of the phonon signal is bound to the generation of phonons due to nonradiative transitions from optical excited state on a metastable level.

Let us consider in more detail the phonon-excited spectra near the R_1 and R_2 lines. As can be seen in the inset of Fig. 2, the R_2-excited phonon signal differs in shape from a background phonon signal and has an expressed ballistic character. Indeed, at short times equal to the times of flight of ballistic longitudinal and transverse 29-cm^{-1} phonons, the bolometer signal amplitude has peaks. The excitation wavelengths of these phonons peaks are near the transmittivity dip (λ = 6919.26 Å), as can be seen in Fig. 5. As the delay time increases, these peaks decrease and two new excitation lines of phonons with λ = 6919.85 Å and λ = 6920.17 Å become visible in the phonon excitation spectra. These lines are in the long-wave area of the R_2 region.

An even more interesting situation is observed in the R_1 region, as can be seen in Fig. 6. At small delay times (~0.5 μs), there is a well pronounced line lower than the R_1 level at 1.1 Å in the phonon excitation spectrum. It is known that the line of the fourth nearest neighbors 4*H*3 should be somewhere here, which is very difficult to resolve by direct optical methods: the experimental value of the energy level is not given in [3], $\nu(4H3)$ = 14416.7 cm^{-1} [7, 8], $\nu(4H3) = \nu(R_1) - 2.0$ cm^{-1} [9]; that is, $\nu(4H3)$ = 14416.52 cm^{-1}. In approximately this place (ν = 14416.36 cm^{-1}, λ = 6934.65 Å), the peak in the phonon excitation spectra is observed at all delay times, as can be seen in Figs. 4 and 6. Presence or absence of the line located at a frequency slightly lower than R_1 line is very important [8–10] for the examination of mechanisms of migration of energy from single ions to pairs. However, intensities of phonon signals on transition 4*H*3 and 4*G*3 pairs are expected to be equal [8], but they strongly differ in our experiment. This is probably so because, at the 4*H*3-transition frequency, the single ions are excited simultaneously with pairs, which rapidly transfer energy to single ones. It is possible to say that, for the first time, the fast resonance

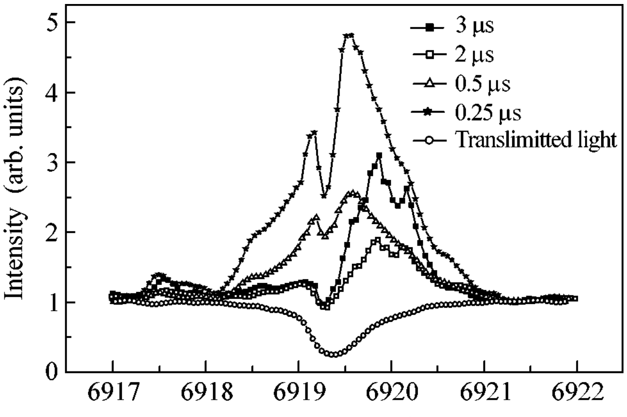

Fig. 5. R_2 region of the laser pulse transmittivity and the phonon excitation spectra of Fig. 4 at different delay times after the laser pulse input.

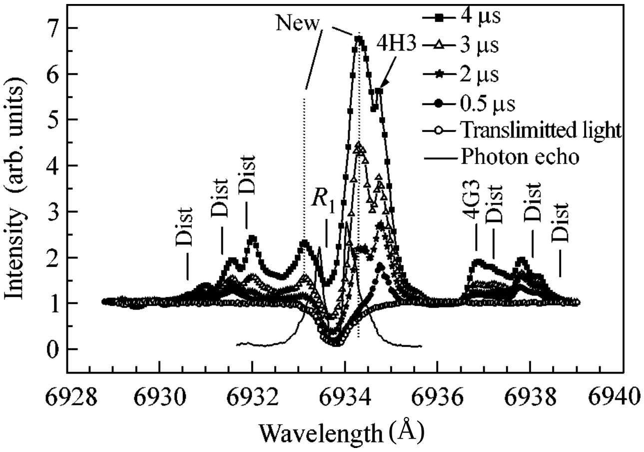

Fig. 6. R_1 region of the phonon excitation spectra of Fig. 4 at different delay times after the laser pulse input. The laser pulse transmittivity and amplitude of the backward two pulse (delay time 30.0 ns between the pulses) photon echo near the R_1 line are also shown.

transfer of energy from single ions to pairs of the fourth-nearest neighbors has been detected directly.

Finally, as is seen in Figs. 4 and 6, with increasing delay time, two new lines become visible in the phonon excitation spectra. One of them (λ = 6933.11 Å) is slightly above the R_1 line, and the other, very intensive (λ = 6934.3 Å), is slightly below this line. From various literature data, it follows that the level 4*I*3 either practically coincides with the R_1 line [3] or lies 0.5 cm^{-1} above it [7, 8]. According to us, the difference between λ = 6933.11 Å and R_1 lines is almost 1.0 cm^{-1}. In addition, unlike the 4*G*3 and 4*H*3 lines, this line is not observed at 0.5 μs delay time. Therefore, for the statement that is the line of pairs 4*I*3, there are no major bases. The least clear is the occurrence of the phonon peak with λ = 6934.3 Å. At delay times less than 1.0 μs, it is not observed at all, and then it grows very rapidly with increasing delay time; i.e., there is an effective phonon generation delayed in time at this wavelength. As the time dependence of this phonon peak sharply differs from those of 4*G*3 and 4*H*3 (and also the third and distant neighbors), we believe that this line originates from strongly perturbed Cr single ions, near to but not part of pairs. Indirect confirmation of this conclusion is that, at almost the same distance from the R_2 line, the phonon peak (see Fig. 5) is also observed. As can be seen in this figure, the dip in the backward photon echo amplitude is due to the strong resonant absorption of the second laser pulse, which is passed twice through a sample. It is visible that the 4*H*3 pairs have practically no influence on the photon echo signal. In contrast, some influence of new centers with λ = 6933.13 Å and λ = 6934.3 Å affect the photon echo signal shape of uprise and wane versus wavelength. In our opinion, this again is evidence that these two lines belong to single chromium ions. Qualitatively similar to our phonon excitation spectra, the spectra of fluorescence excitation were observed in [11] at 5.0 μs delay in 0.51 at. % ruby at 6 K in the region of the R_1 and R_2 lines. It was assumed in [11] that the new lines of fluorescence excitation in the vicinity of the *R* lines originate from *R*' ions. These ions [11] are neither truly isolated nor tightly bound into triplet, and they couple strongly to the pair but only weakly to the isolated *R* ions. In [11], lines similar to 6920.17 and 6934.13 Å were related to N_2 excitation lines, and similar to 6933.13 Å was related to the N_1 excitation line.

Thus, it is shown that the time-resolved photo-phonon spectroscopy appears to be a very sensitive method of detecting optical transitions in excited states that have the strong nonradiative relaxation. The time resolution of the method is defined by the bolometer rise time (about 30.0 ns in the case of an In bolometer and 20.0 ns in the case of a Sn bolometer) and allows one to observe spectra evolution on a nanosecond time scale. A combination of this method and detection of the time-resolved fluorescence excitation spectra gives a more complete physical pattern of such phenomena as the process of energy transfer between single ions and pairs of the nearest neighbors, which has still not been solved, with more and more new models [12] of this problem appearing.

The authors would like to thank Dr. N.K. Solovarov for helpful discussion of results. This work was supported in part by the Russian Foundation for Basic Research (project nos. 00-02-16510, 01-02-17730, and 02-02-17622) and by ISTC (project no. 2121).

REFERENCES

1. M. B. Robin and N. A. Kuebler, J. Chem. Phys. **66**, 169 (1977).
2. A. Rosencwaig, *Photoacoustics and Photoacoustic Spectroscopy* (Krieger, Malabar, Fla., 1990).
3. P. Kisliuk, N. C. Chang, P. L. Scott, and M. H. L. Pryce, Phys. Rev. **184**, 367 (1969).
4. Y. Engstrom and L. F. Mollenauer, Phys. Rev. B **7**, 1616 (1973).
5. R. C. Powell and B. DiBartolo, Phys. Status Solidi A **10**, 315 (1972).
6. P. Hu, Phys. Rev. Lett. **44**, 417 (1980).
7. L. M. Kanskaya, V. V. Druzhinin, and A. K. Przhevuskii, Sov. Phys. Solid State **11**, 2093 (1970).
8. M. Montagna, G. Nardon, O. Pilla, and G. Viliani, J. Phys. C: Solid State Phys. **20**, 1563 (1987).
9. P. M. Selzer, D. S. Hamilton, and W. M. Yen, Phys. Rev. Lett. **38**, 858 (1977).
10. X. X. Zhang, P. Xong, B. Di Bartolo, *et al.*, J. Phys.: Condens. Matter **6**, 4661 (1994).
11. P. M. Selzer, D. L. Huber, D. D. Barnett, and W. M. Yen, Phys. Rev. B **17**, 4979 (1978).
12. S. P. Jamison and G. F. Imbusch, J. Lumin. **75**, 143 (1997).

JETP Letters, Vol. 78, No. 11, 2003, pp. 734–739. Translated from Pis'ma v Zhurnal Éksperimental'noĭ i Teoreticheskoĭ Fiziki, Vol. 78, No. 11, 2003, pp. 1251–1256.
Original Russian Text Copyright © 2003 by Kagan, Maksimov.

Relaxation of Bose-Condensate Oscillations in a Mesoscopic System at $T = 0$

Yu. Kagan* and L. A. Maksimov
Russian Research Centre Kurchatov Institute, pl. Kurchatova 1, Moscow, 123182 Russia
**e-mail: kagan@kurm.polyn.kiae.su*

Received November 3, 2003

A general system of nonlinear equations describing the nondissipative evolution of an oscillating Bose condensate is presented. The relaxation of the transverse oscillations of the condensate in a trap of cylindrical symmetry is considered. The evolution is due to the parametric resonance coupling the transverse mode with the longitudinal ones. Nonlinear rescattering in the subsystem of discrete longitudinal modes leads to the suppression of back energy recovery, generating the nondissipative nonmonotonic relaxation of the transverse oscillations of the condensate. © *2003 MAIK "Nauka/Interperiodica".*

PACS numbers: 03.75.Kk; 05.30.Jp

The detection of Bose–Einstein condensation in ultracold gases has opened up a unique possibility of studying the evolution of the coherent properties of a macroscopic system isolated from the environment. One of the most interesting aspects here is associated with the elucidation and analysis of the nature of the damping of coherent oscillations of the condensate. Until recently, the theoretical and experimental study of this problem was actually associated with the consideration of damping at finite temperature T (see the detailed bibliography in [1]). In this case, the ensemble of normal excitations serves effectively as an internal thermal bath. Interaction with the thermal excitations leads to the damping of condensate oscillations with energy transfer to the subsystem of normal excitations.

The question of the internal mechanism of damping at $T = 0$ is of special interest in this problem. The authors [2] have demonstrated the existence of this mechanism by the consideration of the damping of radial coherent oscillations of a condensate of cylindrical symmetry residing in a transverse parabolic potential. It has been found that damping arises from a peculiar kind of parametric resonance, which leads to energy transfer to the subsystem of longitudinal modes. The parametric resonance itself is due to oscillations of the velocity of sound caused by transverse oscillations of the condensate. It should be emphasized that the results obtained in [2] can be used only for the description of the initial period of damping. In order to describe damping at long times in an isolated system of finite sizes with a discrete system of energy levels, it is necessary to know additionally the time evolution in the subsystem of longitudinal modes and to take into account the variation of the parametric resonance with decreasing amplitude of transverse oscillations. Therein lies the essential difference from the standard pattern of parametric resonance. The choice of the geometry of the system was predefined by the fact that, as was rigorously found in [3] (see, also, [4]), two-dimensional oscillations are not damped under arbitrary variations of the frequency of the two-dimensional parabolic potential of circular symmetry at arbitrary values of parameters.

Recently, the Parisian group [1] published the results of an experimental study of the damping of transverse oscillations of the condensate as a whole (breathing mode, BM) in an elongated trap with azimuthal symmetry at an ultralow temperature (40 nK). At a small value of the BM amplitude, the authors observed record slow damping. At a higher value of the starting BM amplitude, the pattern of damping radically changed. Now, after a drop over a bounded interval of time, back energy transfer starts with increasing BM amplitude. The normal behavior of damping was restored only after an appreciable interval of time.

A theoretical analysis with an explanation of the anomalous pattern of damping was given in [5]. It was found that taking into account the nonlinear coupling between the transverse and longitudinal modes is the crucial factor. In this case, however, the relaxation of longitudinal excitations was actually taken into account phenomenologically.

In fact, irreversible damping does not arise in the case of a discrete energy spectrum typical for a closed mesoscopic system. One can only consider unsteady energy redistribution in the system of longitudinal modes.

In this work, a complete system of nonlinear equations is obtained that describes the time evolution of an oscillating condensate in the absence of irreversible dissipation channels. The starting point is the Gross–Pitaevskii equation. A condensate of cylindrical symmetry is considered in a transverse parabolic potential with the longitudinal size $2L \gg R$, where R is the static radius of the condensate. An analysis of the solution demonstrates that the damping of radial oscillation essentially depends on the character of the evolution of longitudinal oscillations. The redistribution of the energy transferred to this subsystem leads to a chaotic unsteady pattern of the occupation of discrete levels and simultaneously to a substantial cancellation of amplitudes of active longitudinal modes directly excited as a result of parametric resonance. Effectively, this cancellation is equivalent to relaxation but proceeds in the absence of real dissipation.

The dynamics of the Bose condensate in a rarefied gas at $T = 0$ will be considered in the framework of the nonlinear Gross–Pitaevskii equation for a condensate wave function Ψ

$$i\hbar\frac{\partial\Psi(\mathbf{r},t)}{\partial t} = \left[-\frac{\hbar^2}{2m}\nabla^2 + V(\mathbf{r})\right]\Psi(\mathbf{r},t) + U_0\Psi^*(\mathbf{r},t)\Psi^2(\mathbf{r},t). \quad (1)$$

Here, $U_0 = 4\pi\hbar^2 a/m$ is a vertex of the local interaction of particles, and a is the scattering length. It is assumed that the system is closed and the number of particles N and the total energy E are conserved in the evolution process. We restrict ourselves to the case of interparticle repulsion ($a > 0$). Let us represent the wave function in the form

$$\Psi(\mathbf{r},t) = \sqrt{n(\mathbf{r},t)}e^{i\Phi(\mathbf{r},t)}.$$

The imaginary part of Eq. (1) directly gives the continuity equation for the condensate

$$\frac{\partial n_1(\mathbf{r},t)}{\partial t} + \nabla[(n_0(\mathbf{r}) + n_1(\mathbf{r},t)]\mathbf{v}(\mathbf{r},t) = 0, \qquad \mathbf{v}(\mathbf{r},t) = \frac{\hbar}{m}\nabla\Phi(\mathbf{r},t). \quad (2)$$

In Eq. (2), we introduced the explicitly time-dependent part of the density $n_1(\mathbf{r}, t)$, representing the total density in the form $n(\mathbf{r}, t) = n_0(\mathbf{r}) + n_1(\mathbf{r}, t)$.

The real part of Eq. (1) leads to the equation for the phase

$$-\hbar\frac{\partial\Phi}{\partial t} = \frac{\hbar^2}{2m}(\nabla\Phi)^2 + U_0 n + V(\mathbf{r}) - \frac{\hbar^2}{2m\sqrt{n}}\nabla^2\sqrt{n}. \quad (3)$$

Below, a gas of a sufficiently high density at which the correlation length $\xi = 1/\sqrt{mn_0U_0}$ is small in comparison with all the sizes of the system is considered throughout. Only long-wavelength condensate excitations with wavelengths large in comparison with ξ turn out to be involved in the processes under consideration. Under these conditions, which correspond to the Thomas–Fermi approximation, the last term in Eq. (3) can be neglected (see, for example, [6]). In the steady-state case, when $\mathbf{v} = 0$, the phase of the condensate wave function has the known value $\Phi_0 = -\mu_0 t/\hbar$, where μ_0 is the chemical potential. Then, from Eq. 3, it follows that

$$n_0(\mathbf{r}) = \frac{1}{U_0}(\mu_0 - V(\mathbf{r})). \quad (4)$$

Retaining the designation Φ only for the phase associated with the dynamics of the condensate, we obtain

$$-\hbar\frac{\partial\Phi}{\partial t} = \frac{\hbar^2}{2m}(\nabla\Phi)^2 + U_0 n_1. \quad (5)$$

The system of nonlinear equations (2) and (5) describes not only the excitations of the quantum liquid but also their interaction. We will take into account this interaction strictly without resorting to the perturbation theory. Note that the external potential enters into Eqs. (2) and (5) only indirectly through the static density distribution (4).

In the linear approximation, the system of equations (2) and (5) is reduced to the equation of harmonic oscillations

$$\partial^2 n_1/\partial t^2 = c_0^2\nabla(f_0\nabla n_1).$$

Here,

$$f_0(\mathbf{r}) = \frac{n_0(\mathbf{r})}{n_{00}}, \quad n_{00} = n_0(0), \quad c_0^2 = \frac{U_0 n_{00}}{m} = \frac{\mu_0}{m}. \quad (6)$$

Let us introduce a complete set of eigenfunctions of the harmonic problem $\{\chi_s(\mathbf{r})\}$, which give a solution to the equation

$$\Omega_k^2\chi_s(\mathbf{r}) + c_0^2\nabla(f_0(\mathbf{r})\nabla\chi_s(\mathbf{r})) = 0. \quad (7)$$

Let us expand the functions n_1 and Φ in the complete set of eigenfunctions $\chi_s(\mathbf{r})$

$$n_1(t,\mathbf{r}) = \sum_s c_s(t)\chi_s(\mathbf{r}), \quad \Phi = \sum_s a_s(t)\chi_s(\mathbf{r}). \quad (8)$$

Substituting these expansions into Eqs. (2) and (5), we find

$$\frac{\partial}{\partial t}c_s - \frac{\hbar\Omega_s^2}{U_0}a_s = \frac{\hbar}{m}\sum_{s_1s_2}c_{s_1}a_{s_2}\langle\chi_{s_1}(\nabla\chi_s^*)(\nabla\chi_{s_2})\rangle,$$
$$\frac{\partial}{\partial t}a_s + \frac{U_0}{\hbar}c_s = -\frac{\hbar}{2m}\sum_{s_1s_2}a_{s_1}a_{s_2}\langle\chi_s^*(\nabla\chi_{s_1})(\nabla\chi_{s_2})\rangle. \quad (9)$$

Here, $\langle\ldots\rangle = \int d^3r(\ldots)$. In the right-hand side of the first equation, we took advantage of the transformation

$$\langle\chi_s^*\nabla(\chi_{s_1}(\nabla\chi_{s_2}))\rangle = -\langle\chi_{s_1}(\nabla\chi_s^*)(\nabla\chi_{s_2})\rangle.$$

Let us introduce the new variables

$$a_s = \left(\frac{U_0}{\hbar\Omega_s}\right)^{1/2}(y_s + y_{-s}^*), \quad c_s = i\left(\frac{\hbar\Omega_s}{U_0}\right)^{1/2}(y_s - y_{-s}^*).$$

For the modes described by the real eigenfunctions χ_s, the coefficients a_s and b_s are real and $y_{-s} \equiv y_s$.

In these variables, Eqs. (9) can be represented as

$$\frac{\partial}{\partial t}y_s + i\Omega_s y_s = \sum_{s_1 s_2} M_{ss_1s_2}(y_{s_1} - y^*_{-s_1})(y_{s_2} + y^*_{-s_2})$$
$$- \frac{1}{2}\sum_{s_1 s_2} K_{ss_1s_2}(y_{s_1} + y^*_{-s_1})(y_{s_2} + y^*_{-s_2}). \tag{10}$$

Here,

$$M_{ss_1s_2} = \frac{1}{2m}\left(\frac{\hbar U_0 \Omega_{s_1}}{\Omega_s \Omega_{s_2}}\right)^{1/2} \langle (\nabla\chi^*_s)\chi_{s_1}(\nabla\chi_{s_2})\rangle,$$
$$K_{ss_1s_2} = \frac{1}{2m}\left(\frac{\hbar U_0 \Omega_s}{\Omega_{s_1}\Omega_{s_2}}\right)^{1/2} \langle \chi^*_s(\nabla\chi_{s_1})(\nabla\chi_{s_2})\rangle. \tag{11}$$

Let only the transverse oscillation of the condensate as a whole be excited at the initial instant of time with the conservation of the cylindrical symmetry (the breathing mode, designated below with the subscript ⊥). System of equations (10) can be represented in this case as

$$\frac{\partial}{\partial t}y_\perp + i\Omega_\perp y_\perp = \sum_k M_{\perp k-k}(y_k y_{-k} - y^*_k y^*_{-k})$$
$$- \frac{1}{2}\sum_k K_{\perp k-k}(y_k + y^*_{-k})(y_{-k} + y^*_k),$$
$$\frac{\partial}{\partial t}y_k + i\Omega_k y_k = -2M_{kk\perp}y^*_{-k}(y_\perp + y^*_\perp)$$
$$+ K_{\perp k-k}(y_\perp - y^*_\perp)(y_k + y^*_{-k}) + I_k. \tag{12}$$

In the second equation, we made use of the equalities $M_{k\perp k} = K_{\perp k-k}$ and $K_{kk\perp} = M_{kk\perp}$. The last term in the right-hand part determines the evolution in the longitudinal subsystem of excitations

$$I_k = \sum_{k_1k_2} M_{kk_1k_2}(y_{k_1} - y^*_{-k_1})(y_{k_2} + y^*_{-k_2})$$
$$- \frac{1}{2}\sum_{k_1k_2} K_{kk_1k_2}(y_{k_1} + y^*_{-k_1})(y_{k_2} + y^*_{-k_2}). \tag{13}$$

The eigenfunction of the breathing mode can be found as a solution to Eq. (7) with regard to the fact that, in the Thomas–Fermi approximation, $f_0 = 1 - r^2/R^2$, where $R^2 = 2c_0^2/\omega_\perp^2$ and $\omega_\perp$ is the frequency of the parabolic trap,

$$\chi_\perp = \sqrt{\frac{3}{V}}\left(1 - \frac{2r^2}{R^2}\right), \quad \Omega_\perp = 2\omega_\perp, \tag{14}$$

k determines the value of the wave vector of the longitudinal excitations, which ranges over discrete values by virtue of the finiteness of the system size in the z direction. Following [7], one can readily find the eigenfunctions and eigenvalues for the long-wavelength longitudinal modes

$$\chi_k = \sqrt{\frac{1}{V}}e^{ikz}\left[1 - \frac{(kR)^2}{16}\left(1 - \frac{2r^2}{R^2}\right)\right],$$
$$\Omega_k = \bar{c}k\left(1 - \frac{(kR)^2}{96}\right), \quad \bar{c} = \frac{c_0}{\sqrt{2}}. \tag{15}$$

Using Eqs. (14) and (15), one can directly calculate the matrix elements (11) involved in Eq. (12)

$$M_{\perp k-k} = M_{kk\perp} = -\eta\frac{\sqrt{6}}{4}\left(\frac{\Omega_k}{\omega_\perp}\right)^2,$$
$$K_{\perp k-k} = -\eta\frac{5\sqrt{6}}{24}\left(\frac{\Omega_k}{\omega_\perp}\right)^3, \quad \eta = \omega_\perp\left(\frac{\hbar\omega_\perp}{Vn_{00}\mu_0}\right)^{1/2}, \tag{16}$$

and in Eq. (13)

$$M_{kk_1k_2} = \eta\left(\frac{\Omega_k\Omega_{k_1}\Omega_{k_2}}{\omega_\perp^3}\right)^{1/2}\operatorname{sgn}(kk_2)\delta_{k,k_1+k_2},$$
$$K_{kk_1k_2} = -\eta\left(\frac{\Omega_k\Omega_{k_1}\Omega_{k_2}}{\omega_\perp^3}\right)^{1/2}\operatorname{sgn}(k_1k_2)\delta_{k,k_1+k_2}. \tag{17}$$

Equations (12) and (13) along with the matrix elements (16) and (17) completely describe the relaxation of the transverse oscillations of the condensate in a mesoscopic system in the absence of dissipative channels of evolution.

We will assume that the initial amplitude of the BM is relatively small, i.e., $|\delta R/R|_0 \ll 1$. This restricts the scale of the nonlinear interaction between modes. At the same time, the energy range in which the discrete longitudinal modes effectively coupled with the breathing mode lie turns out to be small in comparison with $\omega_\perp$. Under these conditions, we can simplify the system of equations, restricting ourselves to the quasi-resonant approximation. Within this approximation, we may retain in Eqs. (12) and (13) only the terms for which the following inequality is fulfilled:

$$\Delta\Omega = \left|\Omega_s \pm \Omega_{s_1} \pm \Omega_{s_2}\right| \ll \Omega_{s_i}. \tag{18}$$

Let us rewrite Eqs. (12) and (13) in this approximation, introducing the ratios $\bar{y}_s = y_s(t)/|y_\perp(0)|$ instead of amplitudes y_s. The initial BM amplitude $y_\perp(0)$ can be found from a comparison of the vibrational energy of the condensate at the initial instant of time $E_{vib} = \frac{4}{3}\mu_0 N|\delta R/R|_0^2$ with the energy of the transverse mode $2\hbar\Omega_\perp|y_\perp(0)|^2$. From here,

$$|y_\perp(0)| = \left(\frac{2\mu_0 N}{3\hbar\Omega_\perp}\right)^{1/2}\left|\frac{\delta R}{R}\right|_0.$$

With regard to these designations, Eqs. (12) and (13) take the form

$$\frac{\partial}{\partial t}\bar{y}_\perp + i\Omega_\perp\bar{y}_\perp = -\alpha{\sum_{k>0}}'\bar{y}_k\bar{y}_{-k};$$

$$\frac{\partial}{\partial t}\bar{y}_k + i\Omega_k\bar{y}_k = \alpha\bar{y}^*_{-k}\bar{y}_\perp$$
$$+\alpha'\sum_{k>k_1>0}\left(\frac{\Omega_k\Omega_{k_1}\Omega_{k-k_1}}{\omega_\perp^3}\right)^{1/2}\bar{y}_{k_1}\bar{y}_{k-k_1} \tag{19}$$
$$-2\alpha'\sum_{k_1>0}\left(\frac{\Omega_k\Omega_{k_1}\Omega_{k+k_1}}{\omega_\perp^3}\right)^{1/2}\bar{y}^*_{k_1}\bar{y}_{k+k_1}, \quad (k>0).$$

The prime at the sum in the first equation means that the summation is over only the "active modes" directly interacting with the BM with regard to inequality (18). For the longitudinal modes not coupled directly with the transverse mode, the first term in the right-hand side of the second equation (19) should be omitted. In these equations

$$\alpha = |(2M_{\perp k-k}-K_{\perp k-k})||y_\perp(0)| \approx 0.3\omega_\perp\left|\frac{\delta R}{R}\right|_0, \tag{20}$$
$$\alpha' \approx 2\alpha.$$

Let us assume that, at the initial instant of time for the trivially degenerate states, $\bar{y}_k(0) = \bar{y}_{-k}(0)$.

From system of equations (19), it follows that this equality is conserved during the evolution. For analysis, it is convenient to extract the fast phase from the complex variables $\bar{y}_s$ and represent them in the form

$$\bar{y}_s = b_s(t)e^{-i(\Omega_s t+\varphi_s(t))},$$

where $b_s(t)$ and $\varphi_s(t)$ are real quantities varying relatively slow with time at $\alpha/\omega_\perp \ll 1$. Let us introduce the designation

$$\gamma_{kk_1k_2} = (\Omega_k-\Omega_{k_1}-\Omega_{k_2})t+(\varphi_k-\varphi_{k_1}-\varphi_{k_2}). \tag{21}$$

Separating the real and imaginary parts in Eq. (19), we find

$$\frac{\partial}{\partial t}b_\perp = -\alpha{\sum_{k>0}}'b_k^2\cos\gamma_{\perp kk},$$
$$\frac{\partial}{\partial t}\varphi_\perp = \alpha{\sum_{k>0}}'\frac{b_k^2}{b_\perp}\sin\gamma_{\perp kk}, \tag{22}$$

$$\frac{\partial}{\partial t}b_k = \alpha b_k b_\perp\cos\gamma_{\perp kk}+I_k,$$
$$I_k = \alpha'\sum_{k>k_1>0}\left(\frac{\Omega_k\Omega_{k_1}\Omega_{k-k_1}}{\omega_\perp^3}\right)^{1/2}b_{k_1}b_{k-k_1}\cos\gamma_{kk_1k-k_1} \tag{23}$$
$$-2\alpha'\sum_{k_1>0}\left(\frac{\Omega_k\Omega_{k_1}\Omega_{k+k_1}}{\omega_\perp^3}\right)^{1/2}b_{k+k_1}b_{k_1}\cos\gamma_{k+k_1k_1k},$$

$$\frac{\partial}{\partial t}\varphi_k = \alpha b_\perp\sin\gamma_{\perp kk}+I'_k,$$
$$I'_k$$
$$= -\alpha'\sum_{k>k_1>0}\left(\frac{\Omega_k\Omega_{k_1}\Omega_{k-k_1}}{\omega_\perp^3}\right)^{1/2}\frac{b_{k_1}b_{k-k_1}}{b_k}\sin\gamma_{kk_1k-k_1} \tag{24}$$
$$-2\alpha'\sum_{k_1>0}\left(\frac{\Omega_k\Omega_{k_1}\Omega_{k+k_1}}{\omega_\perp^3}\right)^{1/2}\frac{b_{k+k_1}b_{k_1}}{b_k}\sin\gamma_{k+k_1k_1k}.$$

An analysis of the resulting equations allows us to obtain a scenario for the relaxation of the transverse oscillations of the condensate. At the initial instant of time, the longitudinal modes are not excited and obey the relationship $b_k(0) \ll 1$, whereas, by definition, $b_\perp(0) = 1$. Therefore, the right-hand sides of Eq. (22) and the I_k and I'_k terms, which are quadratic in b_k, play no part at the initial period of time, and the evolution is actually determined by the first terms in the right-hand sides of Eqs. (23) and (24) with constant $b_\perp$. The joint solution demonstrates the exponential growth of $b_k(t)$ under the condition

$$|\Delta\Omega| \equiv \left|\Omega_k-\frac{1}{2}\Omega_\perp\right| < \alpha. \tag{25}$$

In particular, at $|\Delta\Omega| = 0$, $\gamma_{\perp kk} \simeq 0$, and it follows from Eq. (23) that $b_k(t) = b_k(0)\exp(\alpha t)$. These results, including the requirement of the finiteness of the initial amplitude $b_k(0)$, are the typical manifestation of the parametric resonance (compare with [2]). All the longitudinal modes that fall within an energy interval of order α (*active modes*) exhibit exponential growth. With the cylinder length $2L$, the separation between the levels is $\delta\Omega = \pi\bar{c}/L$. If $\delta\Omega < 2\alpha$, at least one mode falls within this interval. The growth of $b_k(t)$ leads to the fact that, after a certain delay, $b_\perp(t)$ starts to drop, and energy transfer to other longitudinal modes is switched on concurrently. There are many such modes at $L \gg R$; however, the discrete character of the energy spectrum leads to the complete forbidding of irreversible transitions. However, the irregular character of the transition amplitudes of the $(\Omega_k\Omega_{k_1}\Omega_{k_2}/\omega_\perp^3)^{1/2}\cos\gamma_{kk_1k_2}$ type in Eqs. (23) and (24) in the nonlinear I_k and I'_k terms leads

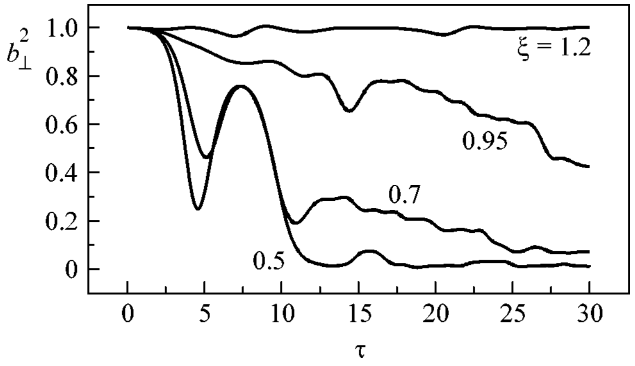

Fig. 1. Time dependence of the population of the breathing mode at the fixed value $k_0 = 10\pi/L$ for $\xi = 0.5$, 0.7, 0.95, and 1.2.

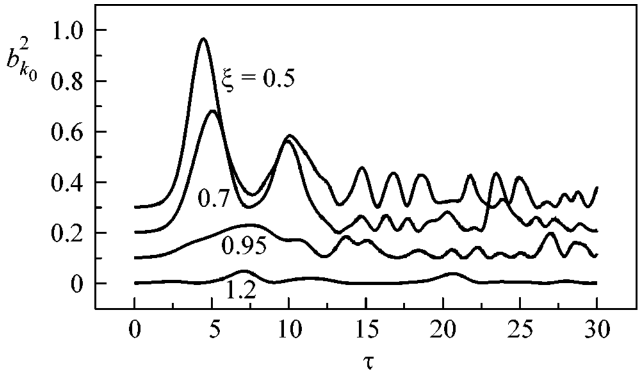

Fig. 2. Time dependence of the population of the active longitudinal mode k_0 at the same values of ξ. These four curves are vertically shifted with respect to each other by 0.1.

to chaotic evolution in the system of longitudinal modes. It should be believed that the return to the active longitudinal levels must be substantially suppressed in this case, and a notable part of the transferred energy must remain on the inactive modes.

The direct numerical solution of the system of equations (22)–(24) reveals the pattern described above. Let only one level k_0 fall within an energy interval of order α. Let us neglect the weak dispersion of the longitudinal modes (15). Then, $\Omega_k\Omega_{k_1}\Omega_{k_2}/\omega_\perp^3 \cong kk_1k_2/k_0$, and the first term in Eq. (21) for the longitudinal modes may be omitted. Let us introduce the dimensionless time $\tau = \alpha t$ and take into account that $\alpha'/\alpha = \text{const}$ (see Eq. (20)). Then, the evolution to be described depends in fact only on the ratio $\xi = \Delta\Omega/\alpha$ and, to a small extent, on k_0 at $k_0L/\pi \gg 1$. (Note that this is true not only in the quasi-resonant approximation but also for general system of equations (12).)

Figure 1 presents the dependences $b_\perp^2(\tau) \equiv (\delta R(\tau)/\delta R(0))^2$ for various values of parameter ξ at a constant value of k_0 (in π/L units). Here, we took into account not only the discrete levels lying below the active level but also the longitudinal levels above k_0, which start to be occupied at the next stage after the decay of the k_0 states. The energy conservation law, which is obeyed by system of equations (22)–(24), leads during the evolution to a weak population of the upper levels. In the calculations, we restricted ourselves to an equal number of levels above and below Ω_{k_0}. At $\xi = 1.2$, the transverse oscillations are not damped at all. This is also clearly seen in Fig. 2, where the population $b_{k_0}^2$ of the k_0 level is represented as a function of τ for the same values of parameter ξ. At the selected value of ξ, the value of $b_{k_0}^2(\tau)$ remains close to zero for all τ. Thus, the statement that the damping of oscillations at $T = 0$ must be completely absent if the conditions for the occurrence of the parametric resonance (25) are violated finds direct corroboration. On the contrary, the curves that correspond to $\xi = 0.7$ and 0.5 demonstrate the occurrence of damping that is nontrivial in its character (see Figs. 1, 2). The drop in $b_\perp^2(\tau)$ and the growth of $b_{k_0}^2(\tau)$ change to back energy transfer to the BM and a drop in the population of the active mode. Only later, when the energy redistribution over other longitudinal modes becomes appreciable, does a conventional monotonic behavior of relaxation arise. The energy, as the direct calculations show, is now spread over all the longitudinal modes, and their population exhibits chaotic evolution. At this stage, in spite of the absence of irreversible processes, the character of interference determined by the spread of the dynamic phases prevents a noticeable increase in the amplitude $b_{k_0}(\tau)$ and, thus, prevents the back energy transfer to the breathing mode. The evolution in this case looks like the relaxation of the transverse condensate oscillation with the concentration of most of the energy in the subsystem of the longitudinal modes.

The sharply nonmonotonic behavior of the damping of the transverse breathing mode similar to that shown in Fig. 1 was experimentally observed in [1]. The large value of $|\delta R/R|_0$ provided the condition $\xi < 1$. It should be noted that the theoretical results obtained are universal to a large extent. Therefore, the revealed pattern of the effective relaxation with its nonmonotonic behavior is general in its character at $T = 0$.

At the same time, a quantitative comparison with the experimental results [1] is difficult primarily by virtue of the finiteness of temperature. Though $T < \mu_0$ in the experiment, $T > \hbar\omega_\perp$, and the longitudinal levels turn out to be thermally populated at the initial instant of time. (Note that, if a random spread of the dynamic phases φ_k at the initial instant of time is introduced, the qualitative pattern of evolution is retained but the quantitative behavior changes.) The slow, close-to-monotonic damping observed in [1] at a considerably smaller value of $|\delta R/R|_0$ has an analogue at $T = 0$ in an isolated system only if ξ is close to unity (see Fig. 1, the curve at $\xi = 0.95$). However, it should not be ruled out that such damping can be associated with dissipative processes caused by external factors. At a comparatively large value of the $|\delta R/R|_0$ ratio, these processes cannot play a role at the most interesting stages of nonmonotonic relaxation.

The authors are grateful to D.L. Kovrizhin for help in computer calculations.

This work was supported by the Russian Foundation for Basic Research, INTAS, and NWO (The Netherlands).

REFERENCES

1. F. Chevy, V. Bretin, P. Rosenusch, *et al.*, Phys. Rev. Lett. **88**, 250402 (2002).
2. Yu. Kagan and L. A. Maksimov, Phys. Rev. A **64**, 053610 (2001).
3. Yu. Kagan, E. L. Surkov, and G. V. Shlyapnikov, Phys. Rev. A **54**, R1753 (1996).
4. L. P. Pitaevskii and A. Rosch, Phys. Rev. A **55**, R853 (1997).
5. Yu. Kagan and L. A. Maksimov, cond-mat/0212377v2 (2002).
6. Fr. Dalfovo, St. Giorgini, L. P. Pitaevskii, and S. Stringari, Rev. Mod. Phys. **71**, 463 (1999).
7. E. Zaremba, Phys. Rev. A **57**, 518 (1998).

Translated by A. Bagatur'yants

JETP Letters, Vol. 78, No. 11, 2003, pp. 740–744. Translated from Pis'ma v Zhurnal Éksperimental'noĭ i Teoreticheskoĭ Fiziki, Vol. 78, No. 11, 2003, pp. 1257–1262.
Original Russian Text Copyright © 2003 by Gutshabash.

Generalized Darboux Transform in the Ishimori Magnet Model on the Background of Spiral Structures

E. Sh. Gutshabash
Research Institute of Physics, St. Petersburg State University, St. Petersburg, 198504 Russia
e-mail: gutshab@EG2097.spb.edu

Received August 21, 2003; in final form, October 29, 2003

The integration procedure based on the generalized Darboux transform is suggested for the Ishimori magnet model. Exact solutions are constructed for the model on the background of spiral structures. The possibility of phase transition in the system is hypothesized. © *2003 MAIK "Nauka/Interperiodica".*

PACS numbers: 75.10.-b

It is well known that the phenomenological approach suggested by Landau and Lifshitz in the theory of ferromagnetism is based on the idea that the evolution of weakly excited states of a spin system in the long-wavelength limit can be described in terms of a constant-length magnetization vector (magnetic moment density) and is characterized by a certain effective field [1]. With allowance for the fact that the greatest contribution to the process comes from the exchange interaction between crystal atoms, this made it possible, in particular, to obtain nonlinear equation for the one-dimensional case (isotropic Heisenberg ferromagnet model), which was subsequently solved by the inverse scattering method (ISM) [2, 3]: exact solitonic solutions were obtained, the excitation spectrum was described, and an infinite set of conservation laws was found. Further progress in this direction was achieved in [4], where the Lax representation was applied to the anisotropic Landau–Lifshitz model (and, thereby, it was proved to belong to the class of completely integrable models), and in [5], where its exact solutions were found by the "dressing" method. Noteworthy is also work [6], which was devoted to the construction of the integrable deformations of Heisenberg model.

The situation is much more complicated in the two-dimensional case. The corresponding nonstationary equation for a Landau–Lifshitz ferromagnet, both isotropic and anisotropic, proves to be nonintegrable (see, e.g., [7]) and has exact solutions only for rather specific cases. At the same time, there is much evidence, both experimental [8] and obtained by numerical simulation [9], of the existence of stable localized two-dimensional excitations with a finite energy. For a two-dimensional system, the spectrum of these excitations becomes more diversified; in particular, new nontrivial topological objects appear in the spectrum.

The model suggested by Ishimori in [10] is presently the major tool for the phenomenological description of ferromagnets of dimensionality (2 + 1). This is primarily due to the key property of this model: it is completely integrable and allows the use of ISM and $\bar{\partial}$-dressing procedure to construct a rather broad class of solutions (vortices (lumps), rational exponential solutions, instantons, etc.) on the trivial background [11–14], while, by using a nonstandard Darboux transform [15], a physically interesting solution can be obtained in the form of a vortex rotating on the circumference with a constant angular velocity.

However, it is worth noting that the exact two-dimensional solutions were found at the expense of the necessity of introducing nonlocal (along with the exchange) spin interactions into the model. The physical mechanism of this interaction is still unclear. In this connection, it should be emphasized that the standard Heisenberg (exchange) interaction mechanism in the so-called Schwinger-boson mean-field theory became more understandable only a relatively short time ago (see, e.g., [8] and references cited therein). This gives grounds to hope that the nature of nonlocality that provides a broad spectrum of reasonable solutions and the corresponding observed physical objects will be clarified in the future and that the Ishimori model is quite realistic (within the framework of the adopted macroscopic approach).

In this work, a new and rather effective integration procedure is proposed for the Ishimori ferromagnet model. It opens the way for constructing exact solutions, including the ones on the nontrivial background. As to the ISM (or the $\bar{\partial}$-dressing method), this may encounter considerable technical difficulties.

The Ishimori magnet model is given by

$$\mathbf{S}_t = \mathbf{S} \wedge (\mathbf{S}_{xx} + \alpha^2 \mathbf{S}_{yy}) + u_y \mathbf{S}_x + u_x \mathbf{S}_y, \tag{1a}$$

$$u_{xx} - \alpha^2 u_{yy} = -2\alpha^2 \mathbf{S}(\mathbf{S}_x \wedge \mathbf{S}_y), \tag{1b}$$

where $\mathbf{S}(x, y, t) = (S_1, S_2, S_3)$ is the three-dimensional magnetization vector, $|\mathbf{S}| = 1$, $u = u(x, y, t)$ is the auxiliary scalar real field, and the parameter α^2 equals ±1. The case $\alpha^2 = 1$ will be called Ishimori-I magnet model (MI-I), and $\alpha^2 = -1$ will be called MI-II.

Note that, in the static limit ($\mathbf{S} = \mathbf{S}(x, y)$) and $u =$ const, the MI-I model transforms into the model of two-dimensional isotropic Heisenberg ferromagnet (elliptic version of the nonlinear $O(3)$-sigma model), which was integrated in [16, 17] by using the ISM with boundary conditions of the spiral-structure type.

A characteristic feature of model (1) is the presence of topological charge

$$Q_T = \frac{1}{4\pi}\int_{-\infty}^{\infty}\int_{-\infty}^{\infty}\mathbf{S}(\mathbf{S}_x \wedge \mathbf{S}_y)dxdy, \tag{2}$$

which is conserved in the course of system evolution (integral of motion) and represents the mapping of a unit 2-sphere onto the 2-sphere: $\tilde{S}^2 \longrightarrow \tilde{S}^2$. This mapping is known to be characterized by the homotopic group $\pi_2(\tilde{S}^2) = Z$, where Z is the integer group, signifying that Q_T must be an integer. According to Eq. (1b), the scalar function $u = u(x, t)$ is related to the topological charge production density.[1]

System of Eqs. (1) is integrated using the following associated linear system:

$$\Psi_y = \frac{1}{\alpha}S\Psi_x, \tag{3a}$$

$$\Psi_t = -2iS\Psi_{xx} + Q\Psi_x, \tag{3b}$$

where $Q = u_yI + \alpha^3u_xS + i\alpha S_yS - iS_x$, $\Psi = \Psi(x, y, t) \in \mathrm{Mat}(2, \mathbb{C})$, $S = \sum_{i=1}^{3}S_i\sigma_i$, σ_i are the standard Pauli matrices, and I is a unit 2 × 2 matrix. From its definition, the matrix S has the following properties: $S = S^*$, $S^2 = I$, $\det S = -1$, and $\mathrm{Tr}S = 0$ (the symbol * denotes Hermitian conjugation).

In what follows, we restrict ourselves to the MI-II case ($\alpha = i$); the situation with MI-I can be analyzed in a similar manner.

We will solve Eqs. (1) by the method of generalized Darboux matrix transform.[2] We also require that system (3) be covariant ($U \longrightarrow \tilde{U}$, $\Psi \longrightarrow \tilde{\Psi}$) about the transformation of the form ($U \equiv S$)[3]

$$\tilde{\Psi} = \Omega(\Psi, \Psi_1)\Psi_1^{-1}, \tag{4}$$

where $\Psi_1 = \Psi_1(x, y, t)$ is a certain nondegenerate bare solution to system of Eqs. (3), and $\Omega(\Psi, \Psi_1) \equiv \Omega(x, y, t) \in \mathrm{Mat}(2, \mathbb{C})$ is a functional defined on the pair set of matrix functions.[4] One then obtains from Eq. (3a) two dressing relations:

$$\tilde{U} = \Omega\Psi_1U\Psi_1^{-1}\Omega^{-1}, \quad \tilde{U} = i\Omega_y(\Omega_x)^{-1}. \tag{5}$$

Hence, setting $z = x + iy$, $\bar{z} = x - iy$, $\partial_z = (1/2)(\partial_x - i\partial_y)$, $\partial_{\bar{z}} = (1/2)(\partial_x + i\partial_y)$, and $W^{(0)} = \Psi_1^{-1}U\Psi_1$, we obtain the first equation for the matrix Ω ($\det(I \pm U)) = \det(I \pm W^{(0)}) = 0$):

$$(I - W^{(0)})(\Omega^{-1})_{\bar{z}} = 0. \tag{6}$$

Note that, due to the symmetry relation $\bar{U} = -\sigma_2U\sigma_2$, the following involutions are valid:

$$\Psi = \sigma_2\bar{\Psi}\sigma_2, \quad Q = \sigma_2\bar{Q}\sigma_2, \quad \Omega = \sigma_2\bar{\Omega}\sigma_2, \tag{7}$$

which means, in particular, that Eq. (6) can be rewritten in the “conjugate” form

$$(I + W^{(0)})(\Omega^{-1})_z = 0. \tag{8}$$

To obtain the second equation for the matrix Ω, one should use Eq. (3b). This equation, however, is rather cumbersome. Taking into account that Eqs. (5) and (6) can easily be expressed in terms of the function $\tilde{\Psi}$, the following consideration can best be carried out for this function.

Using the identity $Q + UQ = -2i(I + U)(uI + U)_{\bar{z}}$, one obtains from Eq. (3b)

$$(I + U)\{\Psi_t + 2i\Psi_{xx} + 2i(u_{\bar{z}}I + U_{\bar{z}})\Psi_x\} = 0. \tag{9}$$

Let us transform this equation. Making allowance for the relation $\Psi_{y\bar{z}} = -U_{\bar{z}}\Psi_x - iU\Psi_{x\bar{z}}$ that follows from Eq. (3a), one has

$$(I + U)\{\Psi_t + 2i\Psi_{xx} + 2iu_{\bar{z}}\Psi_x - 2\Psi_{y\bar{z}} - 2iU\Psi_{x\bar{z}}\} = 0. \tag{10}$$

After multiplying both sides of this equation by U on the left and adding together the resulting expression and Eq. (10), one finds

$$(I + U)\{\Psi_t + 2i\Psi_{zz} + 2i\Psi_{\bar{z}\bar{z}} + 4iu_{\bar{z}}\Psi_{\bar{z}}\} = 0. \tag{11}$$

Thus, after applying transformation (4) together with the covariance requirement, one obtains two (and two analogous conjugate) equations for the function $\tilde{\Psi}$:

$$(I - \tilde{U})\tilde{\Psi}_{\bar{z}} = 0, \tag{12}$$

$$(I + \tilde{U})\{\tilde{\Psi}_t + 2i\tilde{\Psi}_{zz} + 2i\tilde{\Psi}_{\bar{z}\bar{z}} + 4i\tilde{u}_{\bar{z}}\tilde{\Psi}_{\bar{z}}\} = 0. \tag{13}$$

---

[1] Although, strictly speaking, the function u has no direct physical meaning, the functions u_y and u_x, related to each other by Eq. (1b), can likely be interpreted as “friction coefficients” inducing forced precession of the magnetization vector **S** along the x and y axes, respectively.

[2] In [18], the approach based on the Darboux transform was applied to a system that is gauge equivalent to (3), and the dressing relations were obtained thereafter.

[3] In the literature, the scalar variant of this transformation is sometimes called Moutard transform [19].

[4] It follows from Eq. (3a) that the matrix solutions Ψ and Ψ_1 are related to each other by the nonlinear relationship $\Psi_y(\Psi_x)^{-1} = \Psi_{1y}(\Psi_{1x})^{-1}$.

Next, taking into account the identities $\mathbf{S}(\mathbf{S}_x \wedge \mathbf{S}_y) = (1/2i)\mathrm{Sp}(UU_xU_y)$ and

$$\begin{aligned}\mathrm{Tr}(\tilde{U}\tilde{U}_x\tilde{U}_y) &= \mathrm{Tr}(UU_xU_y) + 2i\Delta(\ln\det\tilde{\Psi}) \\ &+ 2i\mathrm{Tr}\{[U, U_x]\tilde{\Psi}^{-1}\tilde{\Psi}_x + [U, U_y]\tilde{\Psi}^{-1}\tilde{\Psi}_y\} \\ &+ 4\mathrm{Tr}\{U[\tilde{\Psi}^{-1}\tilde{\Psi}_y, \tilde{\Psi}^{-1}\tilde{\Psi}_x]\},\end{aligned} \qquad (14)$$

where Δ is the two-dimensional Laplace operator, and requiring that Eq. (1b) be covariant, we rewrite it as

$$\begin{aligned}\Delta(\tilde{u} - u - 2\ln\det\tilde{\Psi}) &= 2\mathrm{Tr}\{[U, U_x]\tilde{\Psi}^{-1}\tilde{\Psi}_x \\ &+ [U, U_y]\tilde{\Psi}^{-1}\tilde{\Psi}_y - 2iU[\tilde{\Psi}^{-1}\tilde{\Psi}_y, \tilde{\Psi}^{-1}\tilde{\Psi}_x]\}.\end{aligned} \qquad (15)$$

The relevant expression for the dressed topological charge has the form

$$\begin{aligned}\tilde{Q}_T &= Q_T + \frac{1}{4\pi}\int_{-\infty}^{+\infty}\int_{-\infty}^{+\infty} dxdy\Delta\ln\det\tilde{\Psi} \\ &+ \frac{1}{4\pi}\int_{-\infty}^{+\infty}\int_{-\infty}^{+\infty} dxdy\mathrm{Tr}\{[U, U_x]\tilde{\Psi}^{-1}\tilde{\Psi}_x \\ &+ [U, U_y]\tilde{\Psi}^{-1}\tilde{\Psi}_y - 2iU[\tilde{\Psi}^{-1}\tilde{\Psi}_y, \tilde{\Psi}^{-1}\tilde{\Psi}_x]\}.\end{aligned} \qquad (16)$$

Introducing the notation $\Psi[1] = \tilde{\Psi}$, …, $U[1] = \tilde{U}$, …, $u[1] = \tilde{u}$, …, $Q_T[1] = \tilde{Q}_T$,…, one can readily obtain from Eqs. (5), (15), and (16) upon N-fold dressing of the starting bare solution $U = U^{(1)} \equiv U[0]$[5]

$$U[N] = \left(\prod_{j=0}^{N-1}\Psi[N-j]\right)U\left(\prod_{j=0}^{N-1}\Psi[N-j]\right)^{-1}, \qquad (17)$$

$$\begin{aligned}u[N] &= u + 2\sum_{j=1}^{N}\ln\det\Psi[j] \\ &+ \int_{-\infty}^{+\infty}\int_{-\infty}^{+\infty} dx'dy'G(x-x', y-y')\sum_{j=1}^{N}\mathrm{Tr}A_j(x', y', t),\end{aligned} \qquad (18)$$

$$\begin{aligned}Q_T[N] &= Q_T + \frac{1}{4\pi}\int_{-\infty}^{+\infty}\int_{-\infty}^{+\infty} dxdy\sum_{j=1}^{N}\Delta\ln\det\Psi[j] \\ &+ \frac{1}{4\pi}\int_{-\infty}^{+\infty}\int_{-\infty}^{+\infty} dx'dy'\sum_{j=1}^{N}\mathrm{Tr}A_j(x', y', t),\end{aligned} \qquad (19)$$

where $A_j(x, y, t) = [U[j-1], U_x[j-1]]\tilde{\Psi}[j]^{-1}\tilde{\Psi}_x[j] + [U[j-1], U_y[j-1]]\tilde{\Psi}[j]^{-1}\tilde{\Psi}_y[j] - 2iU[j-1] \times [\tilde{\Psi}[j]^{-1}\tilde{\Psi}_y[j], \tilde{\Psi}[j]^{-1}\tilde{\Psi}_x[j]]$, $G(x, y) = (1/2\pi)\ln(x^2 + y^2)$ is the Green's function of the Laplace equation.

Turning back to the simple dressing, we note that Eqs. (12) and (13) define the whole collection of the solutions to model (1) (in the reflectionless (in ISM terms) section of the problem). According to Eqs. (12) and (13), four cases are possible: (1) $\tilde{\Psi}_{\bar{z}} = 0$ and the braced expression in Eq. (13) is also zero; (2) $\tilde{\Psi}_{\bar{z}} = 0$ and the expression in braces is nonzero; (3) the situation opposite to (2); and (4) $\tilde{\Psi}_{\bar{z}} \neq 0$ and the expression in Eq. (13) is also nonzero (i.e., the columns of this matrix belong to the kernels of the degenerate $I - \tilde{U}$ and $I + \tilde{U}$ transformations, respectively).

In this letter, we restrict ourselves only to the first case. Then,

$$\tilde{\Psi}_{\bar{z}} = 0, \quad \tilde{\Psi}_t + 2i\tilde{\Psi}_{zz} = 0. \qquad (20)$$

This system has the well-known polynomial solutions ($\tilde{\Psi} = \{\tilde{\Psi}_{ij}\}$, $i, j = 1, 2$, $\tilde{\Psi}_{22} = \overline{\tilde{\Psi}}_{11}$, $\tilde{\Psi}_{12} = -\overline{\tilde{\Psi}}_{21}$) [10, 13]:

$$\begin{aligned}\tilde{\Psi}_{11}(z, t) &= \sum_{j=0}^{N_1}\sum_{m+2n=j}\frac{a_j}{m!n!}\left(-\frac{1}{2}z\right)^m\left(-\frac{1}{2}it\right)^n, \\ \tilde{\Psi}_{21}(z, t) &= \sum_{j=0}^{M_1}\sum_{m+2n=j}\frac{b_j}{m!n!}\left(-\frac{1}{2}z\right)^m\left(-\frac{1}{2}it\right)^n,\end{aligned} \qquad (21)$$

where N_1 is the natural number and $M_1 = N_1 - 1$; a_j and b_j are the complex numbers; and the first summation is over all possible combinations of the numbers $m, n \geq 0$ such that $m + 2n = j$.

The bare solution to Eqs. (1) is taken in the form of vector function $\mathbf{S}^{(1)} = (0, \sin\Phi^{(1)}, \cos\Phi^{(1)})$, where $\Phi^{(1)} = \delta_0 t + \alpha_0 x + \beta_0 y + \gamma_0$ ($\alpha_0, \beta_0, \gamma_0, \delta_0 \in \mathbb{R}$ are parameters), i.e., in the form of a two-dimensional spiral structure with $Q_T = Q_T^{(1)} = 0$ (according to Eq. (2)). To determine the function $u(x, y, t) = u^{(1)}(x, y, t)$, one should substitute this vector into Eqs. (1a) and (1b). The requirement for the compatibility of the resulting two linear equations gives, after integration,

$$\begin{aligned}u^{(1)} &= g_0^{(1)}\left(y + \frac{\beta_0}{\alpha_0}x\right) \\ &+ \int^{s} g_1^{(1)}\left(y(s') + \frac{\beta_0}{\alpha_0}x(s'), t\right)ds',\end{aligned} \qquad (22)$$

---

[5] These formulas can also be written in terms of the matrix functionals $\Omega(\Psi_i, \Psi_j)$, where Ψ_i and Ψ_j are certain bare solutions to Eqs. (3) with $S = S^{(1)}$.

where $g_0^{(1)}$ and $g_1^{(1)}$ are arbitrary functions. The function $g_0^{(1)}$ is constant on the characteristic $y + (\beta_0/\alpha_0)x =$ const and s is its parameter. Therefore, the explicit expression for $\tilde{u}$ is determined by Eq. (18) with $N = 1$ and by Eqs. (21) and (22).

Dressing relation (17) gives ($S_+ = S_1 + iS_2$)

$$\begin{aligned} \tilde{S}_3(x, y, t) &= \frac{\cos\Phi^{(1)}(|\tilde{\Psi}_{11}|^2 - |\tilde{\Psi}_{21}|^2) - i\sin\Phi^{(1)}(\tilde{\bar{\Psi}}_{21}\tilde{\bar{\Psi}}_{11} - \tilde{\Psi}_{21}\tilde{\Psi}_{11})}{|\tilde{\Psi}_{11}|^2 + |\tilde{\Psi}_{21}|^2}, \\ \tilde{S}_+(x, y, t) &= \frac{2\cos\Phi^{(1)}\tilde{\Psi}_{21}\tilde{\bar{\Psi}}_{11} + i\sin\Phi^{(1)}(\tilde{\bar{\Psi}}_{11}^2 + \tilde{\bar{\Psi}}_{21}^2)}{|\tilde{\Psi}_{11}|^2 + |\tilde{\Psi}_{21}|^2}. \end{aligned} \qquad (23)$$

Setting $\delta_0 = 0$ and $N_1 = 1$, we obtain the simplest static (anti)vortex (one-lump) solution on the background of (also) static spiral structure:

$$\begin{aligned} \tilde{S}_3(x, y, t) &= \frac{\cos\Phi^{(1)}\left(\left[\left|a_0 - \frac{1}{2}a_1 z\right|^2 - |b_0|^2\right] + i\sin\Phi^{(1)}\left[b_0\left(a_0 - \frac{1}{2}a_1 z\right) - \bar{b}_0\left(\bar{a}_0 - \frac{1}{2}\bar{a}_1\bar{z}\right)\right]\right)}{\left|a_0 - \frac{1}{2}a_1 z\right|^2 + |b_0|^2}, \\ \tilde{S}_+(x, y, t) &= \frac{2b_0\cos\Phi^{(1)}\left(\bar{a}_0 - \frac{1}{2}\bar{a}_1\bar{z}\right) + i\sin\Phi^{(1)}\left[b_0^2 + \left(\bar{a}_0 - \frac{1}{2}\bar{a}_1\bar{z}\right)^2\right]}{\left|a_0 - \frac{1}{2}a_1 z\right|^2 + |b_0|^2}. \end{aligned} \qquad (24)$$

The calculations in Eq. (16) show that $\tilde{Q}_T \longrightarrow \infty$; the divergence arises after the integration of the first two terms in the brackets. For $\delta_0 = \alpha_0 = \beta_0 = \gamma_0 = 0$, solution (24) transforms into a static (anti)vortex (on the trivial background) with the topological charge $\tilde{Q}_T = -1$ (see also [13]).

For $\delta_0 \neq 0$ and $N_1 = 2$, i.e., for $\tilde{\Psi}_{11} = a_0 - (a_1/2)z + (a_2/2)[(1/4)z^2 - it]$ and $\tilde{\Psi}_{21} = b_0 - (1/2)b_1 z$, formulas (23) describe the dynamic (anti)two-vortex (two-lump) state on the background of (also) dynamic spiral structure with $\tilde{Q}_T \longrightarrow \infty$, and it transforms to the state with $\tilde{Q}_T = -2$ if the parameters entering $\Phi^{(1)}$ turn to zero.

Clearly, the intermediate types of solutions are also quite realistic and of interest. Among these are a static vortex on the background of the dynamic spiral structure and a dynamic vortex on the background of the static spiral structure.

On the basis of these results, the hypothesis can be put forward that the structural second-order spiral–vortex $\longrightarrow$ vortex phase transition (analogous to the Kosterlitz–Thouless transition) is possible in the system of interest. This can occur if the parameters δ_0, α_0, β_0, and γ_0 are functions of time, i.e., functionals of an external nonstationary and spatially uniform magnetic field.[6] Then, the fact that the parameter turns to zero means that there is a certain critical field ("Curie point" or, more precisely, Lifshitz point) that corresponds to the phase transition point. This hypothesis is confirmed by the experimental fact that the spiral (modulated incommensurate) structure in a magnetic field can convert into the commensurate structure corresponding to a paramagnet with magnetic moments mainly oriented along the external field[7] [20]. We also emphasize that this phase transition should be accompanied by a change in the symmetry and topological properties of the system.

Another series of solutions to model (1) can be found if the solution to system of equations (20) is sought in the form

$$\tilde{\Psi}_{11,21}(x, y, t) = \int_{-\infty}^{\infty} B_{11,21}(p)e^{-2ip^2t + pz}dp. \qquad (25)$$

Here, $B_{11,21}$ are the functional parameters. In particular, by setting $B_{11,21}(p) = c_{11,21}\delta(p - p_{11,21})$, where $\delta(\cdot)$ is the Dirac delta function and $c_{11,21} \in \mathbb{C}$ and $p_{11,21} \in \mathbb{R}$ are parameters, one obtains using Eq. (17) ($c_{11,21} \neq 0$ and the symbol c.c. stands for the complex conjugation)

---

[6] One can show that the addition of the term $\mathbf{S} \wedge \mathbf{H}(t)$ to the right-hand side of Eq. (1a), where $\mathbf{H}(t)$ is the external magnetic field, merely renormalizes the magnetization vector; i.e., this term can be eliminated by the appropriate transformation by making the bare solution dependent on magnetic field.

[7] Clearly, the theoretical justification of this hypothesis should rest on the consideration of the order parameters of the system and on the analysis of the Ginzburg–Landau functional in the vicinity of the critical point. However, although the Hamiltonian of system (1) is known (generally speaking, it is obtained in [21] for a modified MI model), the relevant calculations become overly cumbersome even for the simplest solutions and, thus, are beyond the scope of this article.

$$\tilde{S}_3(x,y,t) = \frac{\cos\Phi^{(1)}[|c_{11}|^2 e^{2|p_{11}|x} - |c_{21}|^2 e^{2|p_{21}|x}] - i\sin\Phi^{(1)}[\bar{c}_{11}\bar{c}_{21} e^{2i(p_{11}^2 + p_{21}^2)t + 2(p_{11}+p_{21})\bar{z}} - \text{c.c.}]}{|c_{11}|^2 e^{2p_{11}x} + |c_{21}|^2 e^{2p_{21}x}},$$

$$\tilde{S}_+(x,y,t) = \frac{2\bar{c}_{11}c_{21}\cos\Phi^{(1)} e^{2i(p_{11}^2 - p_{21}^2)t + p_{11}\bar{z} + p_{21}z} + i\sin\Phi^{(1)}(\bar{c}_{11}^2 e^{4ip_{11}^2 t + 2p_{11}\bar{z}} + c_{21}^2 e^{-4ip_{21}^2 t + 2p_{21}z})}{|c_{11}|^2 e^{2p_{11}x} + |c_{21}|^2 e^{2p_{21}x}}. \tag{26}$$

Therefore, a nonexponential and nonsingular solution is found on the background of spiral structure. At $\Phi^{(1)} \longrightarrow 0$, the solution is finite if p_{11}, $p_{21} > 0$; in this case, the component $\tilde{S}_3$ evolves only along the x variable.

More complicated solutions of this type can be found if the functionals $B_{11,\,21}$ are taken as linear combinations of delta functions.

Of interest is to compare the results obtained in this work with the results of [22], where the MI-II model was proved to be gauge equivalent to the known hydrodynamic Davy–Stuartson-II system (which describes the evolution of a nearly monochromatic small-amplitude wavepacket at the surface of a small-depth fluid). This means that the Lax pair can be transformed from one system to another by a certain gauge transformation, which, in turn, allows the formulas relating the solutions for these systems to be derived. It is significant that the initial boundary-value problems with specified classes should possess similar equivalence; in [22], the class of rapidly decreasing Cauchy data was assumed in both cases. Clearly, there is no gauge equivalence in the considered case of spiral (and, hence, nondecreasing) structures, while the solution constructed on their background cannot be derived from the solution to the Davy–Stuartson-II model.

Note in conclusion that the approach developed in this work can easily be extended to a series of Myrzakulov magnet models [23, 24], which are modifications of the Ishimori model; for them, the first Lax-pair equation either is close to or coincides with Eq. (3a) and the main modifications concern the functional Q in Eq. (3b).

I am grateful to A.B. Borisov for attention to the work and S.A. Zykov and A.V. Shirokov for assistance.

REFERENCES

1. L. D. Landau, *Collected Works* (Gostekhizdat, Moscow, 1969), Vol. 1, pp. 128–143.
2. L. A. Takhtajan, Phys. Lett. A **64A**, 235 (1977).
3. L. D. Faddeev and L. A. Takhtajan, *Hamiltonian Methods in the Theory of Solitons* (Nauka, Moscow, 1986; Springer, Berlin, 1987).
4. E. K. Sklyanin, Preprint No. E-3-79, LOMI (Inst. of Fine Mechanics and Optics, Leningrad, 1979).
5. A. I. Bobenko, Zap. Nauchn. Semin. LOMI, No. 123, 58 (1983).
6. A. V. Mikhailov and A. B. Shabat, Phys. Lett. A **116**, 191 (1986).
7. A. M. Kosevich, B. A. Ivanov, and A. S. Kovalev, Phys. Rep. **194**, 117 (1994).
8. Tai Kai Ng, Phys. Rev. Lett. **82**, 3504 (1999).
9. B. Piette and W. J. Zakrzewski, Physica D (Amsterdam) **119**, 314 (1998).
10. Y. Ishimori, Prog. Theor. Phys. **72**, 33 (1984).
11. V. G. Dubrovsky and B. G. Konopelchenko, Preprint No. 90-76 (Inst. of Nuclear Physics, Siberian Division, USSR Academy of Sciences, Novosibirsk, 1990).
12. V. G. Dubrovsky and B. G. Konopelchenko, Preprint No. 91-29 (Inst. of Nuclear Physics, Siberian Division, USSR Academy of Sciences, Novosibirsk, 1990).
13. B. G. Konopelchenko, *Solitons in Multidimensions* (World Sci., Singapore, 1993).
14. V. G. Mikhalev, Zap. Nauchn. Semin. LOMI, No. 189, 75 (1991).
15. K. Imai and K. Nozaki, Prog. Theor. Phys. **96**, 521 (1996).
16. E. Sh. Gutshabash and V. D. Lipovskiĭ, Teor. Mat. Fiz. **90**, 175 (1992).
17. G. G. Varzugin, E. Sh. Gutshabash, and V. D. Lipovskiĭ, Teor. Mat. Fiz. **104**, 513 (1995).
18. E. Sh. Gutshabash, Zap. Nauchn. Semin. LOMI, No. 271, 155 (2002); nlin.SI/0302002.
19. C. Athorne and J. J. Nimmo, Inverse Probl. **7**, 809 (1995).
20. Yu. A. Izyumov, *Diffraction of Neutrons on Long-Period Structures* (Énergoatomizdat, Moscow, 1987).
21. L. Martina, G. Profilo, G. Soliani, and L. Solombrino, Phys. Rev. B **49**, 12915 (1994).
22. V. D. Lipovskiĭ and A. V. Shirokov, Funkts. Anal. Pril. **23**, 65 (1989).
23. R. Myrzakulov, Preprint, KazGU (Kazakh State Univ., Alma-Ata, 1987).
24. N. K. Bliev, G. Nugmanova, R. N. Syzdukova, and R. Myrzakulov, Preprint No. 1997-05, CNLP (Alma-Ata, 1997); solv-int/990214.

Translated by V. Sakun